Dissertação

Mestrado em Engenharia Automóvel

Development of a Platform for the Control and Monitoring of Exhaust Gas Emissions from Internal Combustion Engines

João Miguel Moura Adam

Leiria, Abril 2026

Dissertação

Mestrado em Engenharia Automóvel

Development of a Platform for the Control and Monitoring of Exhaust Gas Emissions from Internal Combustion Engines

João Miguel Moura Adam

Dissertação de Mestrado realizada sob a orientação do Doutor Luis Manuel Ventura Serrano, Professor da Escola Superior de Tecnologia e Gestão do Instituto Politécnico de Leiria e coorientação do Doutor João Francisco Romeiro da Fonseca Perreira, Professor da Escola Superior de Tecnologia e Gestão do Instituto Politécnico de Leiria.

Leiria, Abril 2026

This page was intentionally left blank

Originality and Copyright

Agradecimentos

Ao meu orientador, Professor Doutor Luís Serrano, pela orientação contínua ao longo de todo o desenvolvimento deste trabalho. O seu acompanhamento próximo, espírito crítico e disponibilidade foram determinantes na definição das soluções técnicas adotadas e na qualidade final do sistema desenvolvido.

Ao meu coorientador, Professor Doutor João Fonseca Pereira pelo enquadramento académico proporcionado no âmbito deste trabalho e ao longo do percurso académico.

Ao Professor Carlos Ferreira, pelo apoio técnico prestado no desenvolvimento da PCB, nomeadamente na análise de circuitos, validação de soluções e resolução de problemas ao nível do hardware.

Ao Professor Hélder Santos, pelo apoio na componente científica do trabalho, em particular na revisão de conteúdos e enquadramento em literatura técnica.

Aos responsáveis de laboratório, Eng. Nuno Pires e Eng. Diogo Duro, pelo apoio prestado ao longo da realização dos ensaios laboratoriais, nomeadamente na preparação dos *setups* experimentais, instrumentação e aquisição de dados.

À minha família, pelo apoio constante ao longo de todo o percurso.

À minha namorada e aos meus amigos, pelo apoio constante e compreensão ao longo das diferentes fases deste trabalho, contribuindo para a sua conclusão.

Resumo

O presente trabalho teve como objetivo o desenvolvimento de um sistema portátil de medição de emissões de gases de escape, enquadrado no conceito de *Portable Emissions Measurement Systems* (PEMS), com especial enfoque na quantificação de óxidos de azoto (NOx). Este desenvolvimento surge no contexto das limitações dos métodos atualmente utilizados seja nas inspeções técnicas periódicas, seja em contexto de laboratório, que frequentemente não refletem as emissões reais em condições de operação dos veículos.

O sistema desenvolvido integra três componentes principais: um sistema de medição de caudal baseado num tubo de Venturi, utilizando sensores de pressão diferencial e temperatura; um módulo de medição de NOx com comunicação CAN; e uma unidade eletrónica dedicada responsável pela aquisição, processamento e transmissão de dados. A arquitetura foi implementada com base num microcontrolador ESP32-S3, recorrendo a uma abordagem modular e a uma organização de tarefas inspirada em sistemas de tempo real.

O dimensionamento do Venturi foi realizado de acordo com normas ISO, sendo posteriormente validado através de simulação CFD, o que permitiu caracterizar o comportamento do escoamento e os diferenciais de pressão gerados. O sistema eletrónico foi desenvolvido de raiz, incluindo o desenho de uma PCB dedicada com condicionamento de sinal e interfaces de comunicação. O firmware foi implementado em C++, assegurando aquisição e processamento de dados em tempo real.

A validação experimental demonstrou boa concordância na medição de NOx e de temperatura. O módulo de NOx apresentou desvios de 7,27%, 0,44%, 11,00%, 15,06% e 21,34% face ao analisador de referência Testo ao longo dos cinco pontos de ensaio, enquanto a concentração de O_2 diferiu apenas 2% do Testo e 0,9% do banco dinamométrico; os valores de lambda concordaram com os sensores do veículo e AEM dentro de 0,35% a 2,59%. A análise CFD previu um diferencial de pressão mensurável de cerca de 0,28 bar em caudal elevado (116 m/s à entrada), mas apenas cerca de 6 Pa (0,00006 bar) em baixo caudal (1,46 m/s), abaixo da resolução de sensores convencionais. Por esse motivo, a medição de caudal não pôde ser validada de forma conclusiva, mantendo-se o erro de pressão diferencial desprezável apenas acima de aproximadamente 160 Pa.

De forma geral, o sistema desenvolvido constitui uma solução PEMS simplificada e de baixo custo, com um custo total de componentes de aproximadamente 4296 €, face a sistemas PEMS comerciais que ultrapassam tipicamente 150 000 €. É adequado para aplicações de investigação e desenvolvimento, embora a precisão e a calibração, em particular em baixos caudais, devam ainda ser melhoradas e constituam a base do trabalho futuro.

Palavras-chave: PEMS, NOx, Emissões, Venturi, Caudal, CAN

Abstract

The present work aimed at the development of a portable exhaust gas emissions measurement system, framed within the concept of *Portable Emissions Measurement Systems* (PEMS), with a particular focus on the quantification of nitrogen oxides (NOx). This development arises in the context of the limitations of current methods used both in periodic technical inspections and laboratorial tests, which often do not reflect real emissions under actual vehicle operating conditions.

The developed system integrates three main components: a flow measurement system based on a Venturi tube, using differential pressure and temperature sensors; a NOx measurement module with CAN communication; and a dedicated electronic unit responsible for data acquisition, processing, and transmission. The architecture was implemented based on an ESP32-S3 microcontroller, using a modular approach and a task organization inspired by real-time systems.

The Venturi was designed according to ISO standards and subsequently validated through CFD simulation, allowing the characterization of flow behaviour and the generated pressure differentials. The electronic system was developed from scratch, including the design of a dedicated PCB with signal conditioning and communication interfaces. The firmware was implemented in C++, ensuring real-time data acquisition and processing.

Experimental validation showed good agreement for NOx and temperature measurements. The NOx module differed from the reference Testo analyser by 7.27%, 0.44%, 11.00%, 15.06% and 21.34% across the five tested operating points, while the measured O_2 concentration differed by only 2% from the Testo analyser and 0.9% from the dynamometer test bench. The lambda values agreed with the vehicle and AEM sensors within 0.35% to 2.59%. The CFD analysis predicted a measurable pressure differential of about 0.28 bar at high flow (116 m/s inlet velocity), but only about 6 Pa (0.00006 bar) at low flow (1.46 m/s), which is below the resolution of conventional sensors. Consequently, the flow rate could not be conclusively validated, with the differential-pressure error remaining negligible only above approximately 160 Pa.

Overall, the developed system constitutes a simplified, low-cost PEMS solution, with a total component cost of approximately €4296, compared with commercial PEMS that typically exceed €150,000. It is suitable for research and development applications, although

its accuracy and calibration, particularly for low flow rates, still require improvement and should constitute the basis for future developments of this work.

Keywords: PEMS, NOx, Emissions, Venturi, Flow rate, CAN

List of figures

This page was intentionally left blank

Table List

This page was intentionally left blank

List of acronyms

AFR - Air-Fuel Ratio

AI – Artificial Intelligent

CAN - Controller Area Network

C_2O - ketenylidene radical

CFD - Computational Fluid Dynamics

CO - Carbon Monoxide

CO_2 - Carbon Dioxide

DOC - Diesel Oxidation Catalyst

DPF - Diesel Particulate Filter

ECU - Engine Control Unit

ECM - Engine Control Module

EGR - Exhaust Gas Recirculation

EU - European Union

GPF - Gasoline Particulate Filter

H_2 - Hydrogen

H_2O - Water

HC - Hydrocarbons

HNCO - Isocyanic Acid

ISO - International Organization for Standardization

LNT - Lean NOx Trap

NDUV - Non-Dispersive Ultraviolet

NH_3 - Ammonia

NH_4NO_3 - Ammonium Nitrate

NID - Node ID

NO_2 - Nitrogen Dioxide

NOx - Nitrogen Oxides

NSC - NOx Storage Catalyst

O_2 - Oxygen

OBD - On-Board Diagnostics

OBM - On-Board Measurement

PCB - Printed Circuit Board

PEMS - Portable Emissions Measurement System

PETG - Polyethylene terephthalate glycol

PM - Particulate Matter

PTI – Periodical Technical Inspections

RTOS - Real-Time Operating System

SCR - Selective Catalytic Reduction

SEMS - Smart Emissions Measurement System

SPI - Serial Peripheral Interface

SPN – Solid Particle Number

TWC - Three-Way Catalyst

VAT - Value Added Tax

This page was intentionally left blank

Índice

1 Introduction

The monitoring and control of pollutant emissions from internal combustion engines have become a critical aspect in the context of increasingly stringent environmental regulations and growing public health concerns. Accurate measurement of exhaust gas emissions is essential to ensure compliance with these regulations and to properly assess the environmental impact of vehicles.

Despite this, current measurement methods used in Periodic Technical Inspections (PTI) present significant limitations, particularly in their ability to detect malfunctioning or tampered emission control systems [1] As a result, vehicles equipped with degraded or intentionally modified aftertreatment systems may still comply with inspection requirements, leading to an underestimation of their real emissions under actual operating conditions.

In addition, existing measurement solutions are often limited to controlled laboratory environments, lacking the flexibility required to capture emissions under transient engine operation and real driving scenarios. This creates a gap between measured and real-world emissions, highlighting the need for portable and cost-effective measurement systems.

In this context, the present work focuses on the development of a portable exhaust gas measurement system, designed to monitor emissions from internal combustion engines, with particular emphasis on nitrogen oxides (NOx). The system is intended to operate under transient engine conditions, allowing data acquisition both in laboratory environments and during real driving scenarios.

The developed system integrates three main components: a Venturi tube for exhaust gas flow rate determination, based on differential pressure and temperature measurements; a set of sensors for emissions measurement, with particular emphasis on nitrogen oxides (NOx); and a dedicated electronic unit responsible for data acquisition, processing, and management. This unit also ensures system portability, enabling operation under different testing conditions.

The main objective of this work is to develop a low-cost and portable system capable of measuring key exhaust gas parameters, with a particular focus on NOx emissions. More specifically, the work aims to:

1 Evaluate and select suitable sensors for exhaust gas measurement;
2 Develop a method for exhaust gas flow rate estimation based on differential pressure and temperature measurements;
3 Design and implement a dedicated data acquisition and processing system;
4 Validate the performance of the developed system under representative operating conditions.

To achieve these objectives, a combination of analytical modelling, computational simulation, and experimental validation was employed. The exhaust gas flow rate was determined using a Venturi-based approach, designed according to International Organization for Standardization (ISO) standards and analysed through Computational Fluid Dynamics (CFD) simulations. The system hardware was developed to integrate sensors, signal conditioning, and communication interfaces, while embedded software was implemented to manage data acquisition and processing.

The document is structured as follows. Chapter 1 presents the introduction and outlines the objectives and methodology of the work. Chapter 2 provides a literature review on exhaust gas formation, aftertreatment systems, and inspection methodologies in the European Union. Chapter 3 describes the measurement systems and the development of the proposed solution, including hardware, software, and mechanical design. Chapter 4 presents the experimental validation and performance evaluation of the system. Finally, Chapter 5 summarises the main conclusions and proposes directions for future work.

2 Literature Review

The literature review is structured into three main sections. The first section focuses on the formation of exhaust gases and their impact on human health, addressing both pollutants directly generated during the combustion process and secondary compounds resulting from emission control systems.

The second section presents a review of exhaust gas aftertreatment methods in gasoline and diesel engines, including a structured overview of the systems used in vehicles, organized according to Euro emission standards.

Finally, the third section addresses the framework of technical inspections within the European Union (EU).

2.1 The Formation of Exhaust Gases and Their Impact on Health and the Environment

Exhaust gas emissions from internal combustion engines result from incomplete combustion processes and secondary reactions occurring under real operating conditions. Ideally, combustion would produce only carbon dioxide (CO_2) and water (H_2O); however, in practice, several pollutants are formed, including carbon monoxide (CO), hydrocarbons (HC), particulate matter (PM), and NOx. The formation of these species is strongly influenced by parameters such as the air–fuel ratio, combustion temperature, mixture homogeneity, and engine operating conditions.

2.1.1 Carbon Monoxide Emissions

CO is formed as a result of incomplete combustion, in processes that would ideally lead to the formation of CO_2. This occurs mainly due to insufficient oxygen (O_2) availability or limited reaction time to complete oxidation. Under fuel-rich conditions, the lack of O_2 prevents the full oxidation of carbon atoms, promoting the formation of CO instead of CO_2 [2]. Additionally, CO formation may increase at high engine speeds, although the most influential parameter remains the air–fuel ratio [3]

Although CO formation is more significant in spark-ignition engines due to their operation under richer mixtures, it may also occur in compression-ignition engines. Despite operating with overall lean mixtures, local rich zones and diffusion combustion phenomena can lead to incomplete oxidation, particularly at low loads. Furthermore, CO_2 dissociation and slow combustion processes may contribute to CO formation even in the presence of excess O_2 [4].

CO is a colorless gas with a density similar to air and poses severe risks to human health. When inhaled, it interferes with O_2 transport in the bloodstream, leading to symptoms such as headaches, fatigue, and dizziness, and in extreme cases, loss of consciousness and death by asphyxiation[5].

2.1.2 Hydrocarbons Emissions

HC) are primarily associated with incomplete combustion, resulting from unburned or partially burned fuel. Similar to CO, their formation is linked to inadequate oxidation conditions. Additionally, HC emissions may originate from lubricating oil entering the combustion chamber through piston ring clearances [2]. In diesel engines, HC emissions are typically more pronounced under low-load conditions, where lower temperatures and poor fuel-air mixing reduce combustion efficiency.

Partial oxidation of HCs contributes to environmental degradation, including the formation of greenhouse gases and photochemical smog. Furthermore, certain aromatic HCs are known to have adverse health effects, including respiratory irritation and potential carcinogenic properties [6]

2.1.3 Particulate Emissions

PM emissions, commonly referred to as soot, are mainly the result of incomplete combustion, particularly in fuel-rich regions. These particles may also originate from the combustion of lubricants [3]. They are typically very small, with sizes ranging from 0.02 to 0.12 μm[2] , and consist of complex structures where HCs and other compounds may be adsorbed.

Particle formation is strongly associated with diffusion combustion, which explains their predominance in compression-ignition engines. These particles form in regions characterized by high temperature and low O_2 availability [4].

PM is generally composed of three main components [5]:

- Solid carbon structures (soot);
- Soluble Organic Fraction (SOF), consisting of heavy HCs;
- Sulfate fraction (SO_4), typically in the form of hydrated sulfuric acid.

Due to their small size, these particles can penetrate deep into the respiratory system, being associated with increased risks of cardiovascular and pulmonary diseases, as well as cancer [7]

2.1.4 Nitrogen Oxide Emissions

NOx are formed through reactions between nitrogen and O_2 at high temperatures during combustion. Their formation is primarily driven by three mechanisms: thermal NOx, prompt NOx, and the N_2O-intermediate mechanism, with the thermal mechanism being the dominant contributor [3]

Thermal NOx formation is strongly dependent on combustion temperatures above approximately 1800 K, as well as O_2 concentration and residence time at these conditions. The prompt mechanism involves reactions between molecular nitrogen and HC radicals, while the N_2O-intermediate mechanism involves intermediate reactions leading to NOx formation.

NOx emissions have significant environmental and health impacts. Their high solubility in H_20 leads to the formation of nitric acid, contributing to acid rain. Additionally, NOx plays a role in ozone formation and acts as a greenhouse gas. From a health perspective, nitrogen dioxide (NO_2), a component of NOx, is highly toxic and can cause respiratory irritation, exacerbate asthma symptoms, and increase the risk of premature death [8]

2.1.5 Secondary emissions

In addition to primary pollutants formed during combustion, secondary emissions may arise from chemical transformations occurring either in the exhaust system or in the atmosphere. These emissions are particularly relevant due to their impact on air quality and their interaction with aftertreatment systems.

2.1.5.1 Ammonia (NH_3).

NH_3 plays a dual role in automotive applications. It is intentionally used as a reducing agent in Selective Catalytic Reduction (SCR) systems for NOx reduction in lean-burn engines, particularly in diesel applications. However, it may also appear as an undesired secondary emission when it is not fully consumed during the aftertreatment process or when formed in gasoline engines equipped with Three-Way Catalysts (TWC) under rich conditions [9] [10].

In urea-SCR systems, NH_3 is generated from the thermal decomposition of an aqueous urea solution (AdBlue). This process occurs in two main steps: thermolysis of urea, producing NH_3 and isocyanic acid (HNCO), followed by hydrolysis of HNCO, yielding additional NH_3 and CO_2 [11]

NH_3 slip may occur when there is excessive dosing, insufficient mixing, or inadequate temperature conditions for complete reaction. This phenomenon is more likely under transient operation or low-temperature conditions and may be aggravated by incomplete urea decomposition or the formation of deposits such as ammonium nitrate (NH_4NO_3) [12]

From an environmental and health perspective, NH_3 is a corrosive and irritating gas that affects the respiratory system. Additionally, it contributes to the formation of secondary PM, particularly ammonium-based aerosols, playing a significant role in urban air pollution[10].

2.1.5.2 ketenylidene radical (C_2O)

C_2O (often referred to as CCO or associated with the ketenylidene radical) is not a classical species in regulated automotive emissions, unlike CO, CO_2, NOx, or NH_3. In the technical-scientific literature, it mainly appears as a reactive intermediate in combustion kinetics mechanisms, particularly in HC oxidation and high-temperature nitrogen chemistry [13]. For this reason, it is not considered a relevant indicator of exhaust emissions nor a target of WLTP/RDE campaigns or PEMS measurements [14]

Its relevance in the automotive context lies primarily in the role it may play as an intermediate in NO formation through prompt-NO pathways. Under rich and high-temperature conditions, typical of the flame front or locally rich zones, species from the "C_2 pool" and associated radicals can participate in N_2 fixation, and the reaction $C_2O + N_2 \rightarrow NCN + CO$ has been proposed as a pathway to improve the modelling of NO formation [15]

Thus, its importance is indirect, influencing the engine-out NOx, which in turn affects the performance of the TWC and SCR systems.

Thus, its importance is indirect, influencing engine-out NOx, which in turn affects the performance of TWC and SCR systems.

Due to its high reactivity and extremely short lifetimes, C_2O tends to be rapidly converted into more stable species such as CO and CO_2 before reaching the exhaust sampling point. Consequently, the automotive aftertreatment literature does not identify it as an outlet product in DOC, TWC, DPF, or SCR, and it is treated only as an intermediate in gas-phase mechanisms [9]. In practical terms, mitigation relies on combustion and calibration strategies that reduce locally rich zones and the formation of the C_2 pool, indirectly contributing to NOx control and overall emissions system optimisation.

2.2 Vehicle Exhaust gas after treatment systems

Modern internal combustion engines require complex aftertreatment systems to comply with increasingly stringent emission regulations. These systems are designed to reduce the concentration of pollutants such as CO, HCs, PM, and NOx, through a combination of catalytic and filtration processes.

The configuration of aftertreatment systems depends on the engine type and operating conditions. In gasoline engines operating under stoichiometric conditions, emission control is typically achieved using a TWC. In contrast, diesel engines operate under lean conditions, requiring a combination of devices such as Diesel Oxidation Catalysts (DOC), Diesel Particulate Filters (DPF), SCR systems, and Exhaust Gas Recirculation (EGR).

These components are typically arranged in series along the exhaust line, where each element performs a specific function. The interaction between these systems is critical, as the performance of downstream components is often influenced by upstream reactions, particularly in terms of temperature and chemical composition of the exhaust gases.

2.2.1 Exhaust Emissions Treatment in Gasoline Engines

In spark-ignition engines operating under stoichiometric conditions, the TWC is the primary aftertreatment device used to simultaneously reduce CO, HC, and NOx emissions.

The system relies on precise air–fuel ratio control, typically maintained at λ = 1 through feedback from an O_2 sensor and closed-loop control by the ECU.

The efficiency of the TWC depends on maintaining a balance between oxidizing and reducing conditions. Under rich conditions (λ < 1), CO and HC emissions increase due to insufficient O_2, while NOx formation is reduced. Conversely, under lean conditions (λ > 1), NOx formation increases due to higher combustion temperatures, while CO and HC emissions decrease [3].

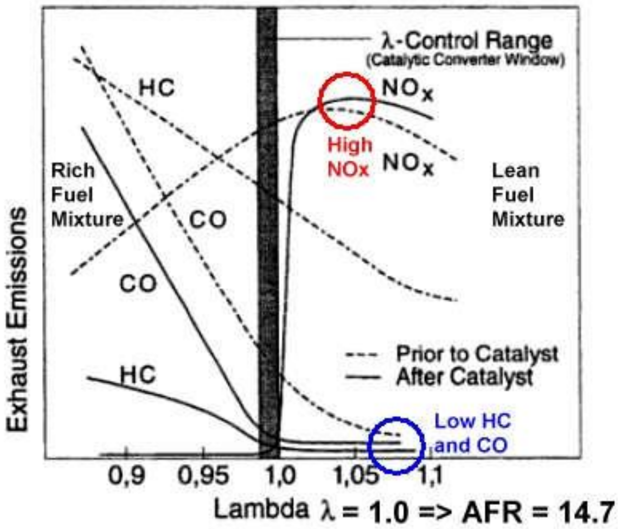

Figure 1 - Variation of CO, HC, and NOx emissions as a function of the air–fuel equivalence ratio (λ) [3]

The TWC consists of a substrate coated with noble metals such as platinum (Pt), palladium (Pd), and rhodium (Rh), which promote oxidation and reduction reactions. These include the oxidation of CO and HC into CO_2 and H_2O, and the reduction of NOx into nitrogen (N_2). As shown in Figure 2.

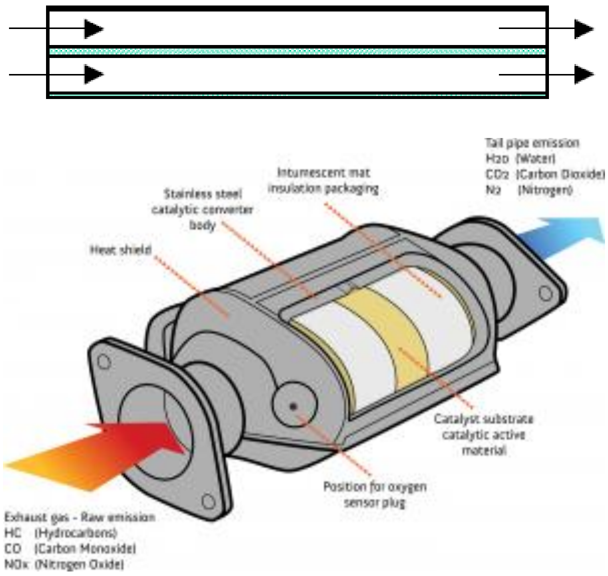

Figure 2 - Three way catalyst [16]

The Lean NOx Trap (LNT) and NOx Storage Catalyst (NSC) refer to the same technology. With the evolution of engines, operation with lean mixtures ($\lambda > 1$), meaning an excess of O_2, became more common. As illustrated in Figure 1, this led to an increase in NOx emissions. To address this issue, the LNT or NSC was introduced, aiming to reduce NOx emissions. This system operates in two main stages.

In the first stage, which occurs during normal engine operation ($\lambda > 1$), NOx is absorbed by the catalyst and stored within its structure. During this phase, nitric oxide (NO) is converted into NO_2, which is then stored in the form of nitrates. In the second stage, the system enters regeneration mode. To achieve this, the air-fuel mixture is enriched ($\lambda < 1$), meaning less O_2 and more fuel. At this stage, the stored nitrates are released and reduced to harmless nitrogen (N_2), as well as CO_2 and H_2O [3]. As shown in Figure 3.

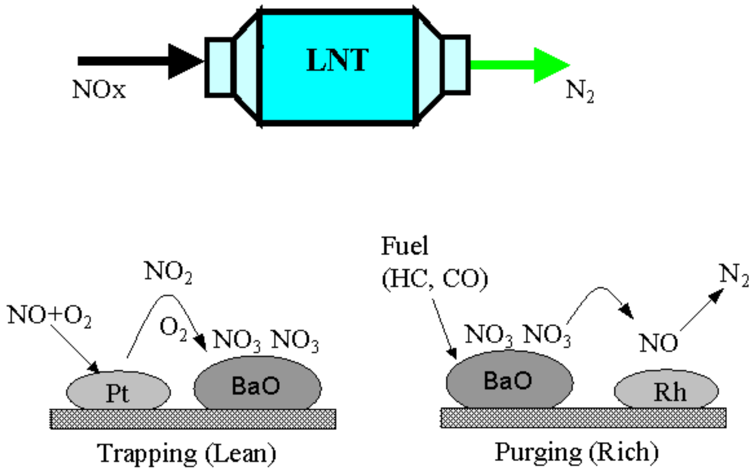

Figure 3 - Schematic representation of a LNT illustrating NOx storage as nitrates under lean conditions (λ > 1) and their reduction to N_2 during rich regeneration (λ < 1) [17]

Additionally, the introduction of Gasoline Particulate Filters (GPF) has become necessary in modern engines with direct injection, due to increased particulate emissions, particularly during transient operation. These filters operate similarly to DPF systems but typically rely on passive regeneration due to higher exhaust gas temperatures. As shown in Figure 4.

Figure 4 - GPF [18]

All systems considered within the scope of each standard are presented in Table 1

Table 1 - Progression of European emission standards (Euro 1 to Euro 7) for gasoline vehicles, showing tightening limits for CO, HC, NOx, and PM, along with associated aftertreatment systems and sensor technologies

Gasoline European Standards	*Year (New Cars)*	*CO (g/km)*	*HC (g/km)*	*NOx (g/km)*	*PM (g/km)*	*Technology (1)*	*Sensors*
EURO 1	1992	2,72	0,97	n/d	n/a	TWC	Lambda
EURO 2	1997	2,2	0,5	n/d	n/a	TWC	Lambda
EURO 3	2001	2,3	0,2	0,15	n/a	TWC	Lambda
EURO 4	2006	1	0,1	0,08	n/a	TWC	Lambda
EURO 5a	2011	1	0,1	0,06	0,005	TWC + GPF (2)	Lambda + PM (4)
EURO 5b	2013	1	0,1	0,06	0,005	TWC + GPF	Lambda + PM
EURO 6a	set/15	1	0,1	0,06	0,005	TWC + GPF	Lambda + PM
EURO 6b	set/15	1	0,1	0,06	0,005	TWC + GPF	Lambda + PM
EURO 6c	set/18	1	0,1	0,06	0,005	TWC + GPF	Lambda + PM
EURO 6d temp	set/19	1	0,1	0,06	0,005	TWC + GPF	Lambda + PM
EURO 6d	jan/21	1	0,1	0,06	0,005	TWC + GPF	Lambda + PM
EURO 7	2025+	1	0,1	0,06	0,003	TWC + GPF + Advanced Sensors	Lambda + PM + NOx + NH3

2.2.2 Exhaust Emissions Treatment in Diesel Engines

In compression ignition engines, emission control is achieved through a combination of aftertreatment devices, typically arranged sequentially along the exhaust system. A common configuration includes a DOC, followed by a DPF, and a SCR system.

The DOC is responsible for oxidizing CO and HCs, as well as promoting the conversion of nitric oxide (NO) into NO_2. This reaction is particularly important, as NO_2 enhances the passive regeneration of the downstream DPF [3], [19] As shown in Figure 5.

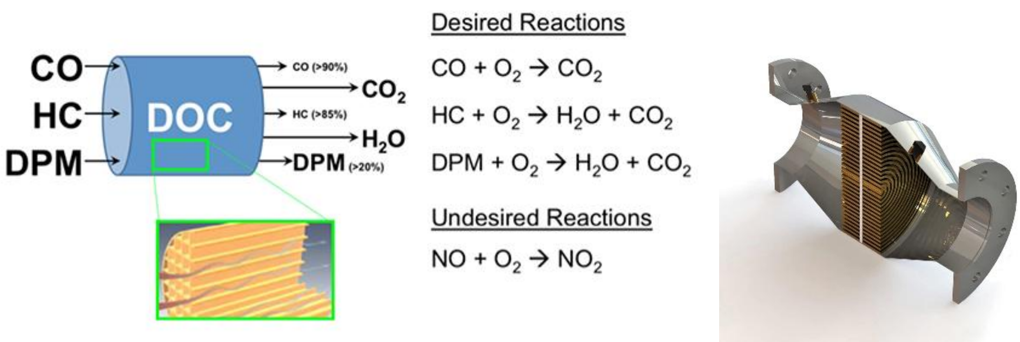

Figure 5 - DOC [20], [21]

The Diesel Particulate Filter (DPF) is designed to capture and store PM present in the exhaust gases. When the accumulated soot reaches a critical level, regeneration is required, during which the stored particles are oxidized into CO_2. This process may occur passively, facilitated by NO_2 produced in the DOC, or actively, through controlled increases in exhaust gas temperature. As shown in Figure 6.

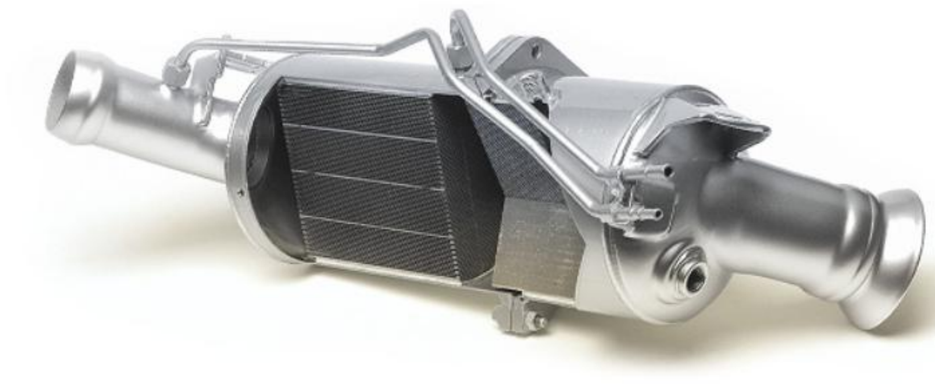

Figure 6 - DPF [22]

The SCR system is used to reduce NOx emissions. It operates by injecting a urea-based solution into the exhaust stream, which decomposes into NH_3. The NH_3 then reacts with NOx over the catalyst, converting it into nitrogen (N_2) and H_2O. The efficiency of this process depends on temperature, mixing, and accurate dosing control [3], [23]. As shown in Figure 7.

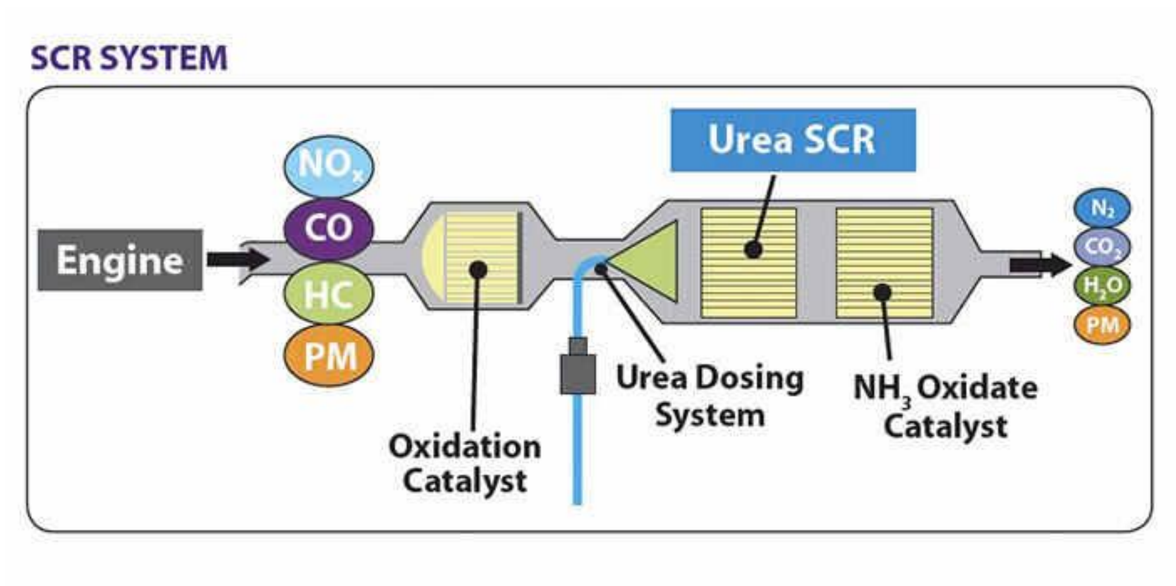

Figure 7 - SCR [24]

In addition to these systems, EGR is commonly used as an in-cylinder emission reduction strategy. By recirculating a portion of the exhaust gases back into the intake, EGR reduces combustion temperature and O_2 concentration, thereby limiting NOx formation at the source. [3], [19]. As shown in Figure 8.

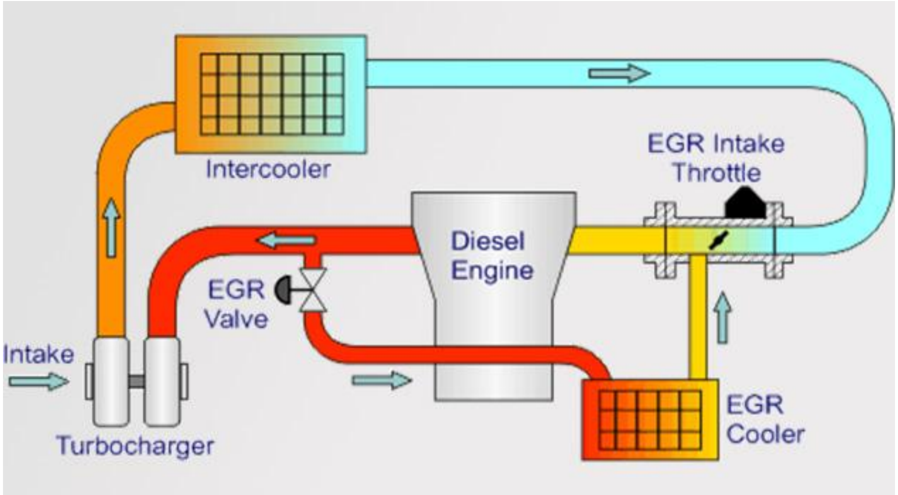

Figure 8 - EGR source [25]

The interaction between these systems is fundamental. For example, the performance of the DPF depends on the NO_2 produced in the DOC, while the efficiency of the SCR system depends on the temperature and composition of the exhaust gases downstream of the DPF.

All systems considered within the scope of each standard are presented in Table 2.

Table 2 - Progression of European emission standards (Euro 1 to Euro 7) for diesel vehicles, showing tightening limits for CO, HC, NOx, and PM, along with associated aftertreatment systems and sensor technologies

Diesel European Standards	***Year New Cars***	***CO (g/km)***	***HC + NOx (g/km)***	***NOx (g/km)***	***PM (g/km)***	***Technology (1)***	***Sensors***
EURO 1	1992	2,72	0,97	n/d	0,14	DOC	n/a
EURO 2 IDI	1997	1	0,7	n/d	0,08	DOC	n/a
EURO 2 DI	1997	1	0,9	n/d	0,1	DOC	n/a
EURO 3	2001	0,66	0,56	0,5	0,05	DOC	n/a
EURO 4	2006	0,5	0,3	0,25	0,025	DOC + DPF	Delt-p
EURO 5a	2011	0,5	0,23	0,18	0,005	DOC + DPF + SCR	Delta-p + EGT + NOx
EURO 5b	2013	0,5	0,23	0,18	0,005	DOC + DPF	Delta-p
EURO 6a	set/15	0,5	0,17	0,08	0,005	DOC + DPF + SCR	Delta-p + EGT + NOx
EURO 6b	set/15	0,5	0,17	0,08	0,005	DOC + LNT + DPF	Delta-p + EGT + NOx + Lambda
EURO 6c	set/18	0,5	0,17	0,08	0,005	DOC + SCR + LNT + DPF	Delta-p + EGT + NOx + Lambda
EURO 6d temp	set/19	0,5	0,17	0,08	0,005	DOC + SCR + DPF	PM
EURO 6d	jan/21	0,5	0,17	0,08	0,005	DOC + SCR + DPF	Delta-p + EGT + NOx + Lambda + NH3
EURO 7	2025+	0,5	0,17	0,08	0,003	DOC + SCR + LNT + DPF + Advanced Sensors	Delta-p + EGT + NOx + Lambda + NH3 + PM

2.3 Periodical Technical Inspections in European Union

2.3.1 Introduction to Periodical Technical Inspections in the European Union

PTIs are an essential regulatory mechanism in the EU designed to ensure vehicle roadworthiness, safety, and compliance with environmental standards. PTIs serve as a preventive measure against excessive emissions, identifying vehicles with malfunctioning or removed emission control devices such as DPFs. Given the significant role of diesel vehicles in European transport, the effectiveness of PTIs in controlling emissions is critical for air quality and public health.

2.3.2 Regulatory Framework for Periodical Technical Inspections in the European Union

The regulatory basis for PTIs in the EU is defined by Directive 2014/45/EU [26], which requires Member States to implement regular technical inspections for vehicles in circulation. This directive establishes the general objectives of PTIs, including the improvement of road safety, the reduction of environmental impact, and the verification of the continued effectiveness of vehicle systems over time.

Although the directive provides the overall framework, each Member State retains some flexibility in the implementation of testing procedures and pass/fail criteria. As a result, differences exist in inspection practices across the EU, particularly regarding emissions testing methodologies. This lack of full harmonisation has contributed to variations in inspection effectiveness, especially in the detection of high-emitting vehicles and tampered aftertreatment systems [1], [27].

2.3.3 Current Periodical Technical Inspections Methods in the European Union

Current PTI procedures for emissions assessment vary according to engine type and pollutant of interest. In diesel engines, the most widely used method has traditionally been smoke opacity measurement. This method is based on the attenuation of a light beam passing through the exhaust plume during a free-acceleration test, typically performed from idle to maximum engine speed with no load applied. In this framework, opacity limits are generally defined according to vehicle category or Euro standard [28], [29].

Despite its widespread use, opacity testing presents important limitations. Although it may provide an indirect indication of soot emissions, several studies have shown that it is not sufficiently sensitive to detect failures or removal of particulate filters, particularly in modern diesel vehicles equipped with DPFs [28], [29]. Consequently, a vehicle with a damaged or removed DPF may still pass a conventional opacity-based PTI.

For gasoline engines, the emissions assessment approach is different and typically focuses on gaseous pollutants such as CO and, in some cases, HCs, depending on the inspection procedure applied at national level. However, as aftertreatment systems have become more complex and emission limits more stringent, the adequacy of conventional PTI methods has increasingly been questioned.

2.3.4 National Variations in Periodical Technical Inspections Regulations

Although PTIs are regulated under a common European directive, their implementation differs across Member States. These differences involve testing procedures, measurement duration, operating conditions, and limit values. Some countries have already introduced more advanced methods for particulate emissions assessment, particularly through Solid Particle Number (SPN) measurements.

For example, the Netherlands and Belgium apply a single 15-second SPN measurement, with a limit of 1×10^6 p/cm^3 for Euro 5 and Euro 6 vehicles. Germany adopts a more stringent procedure, requiring three 30-second measurements with a hot engine and a limit of 2.5×10^5 p/cm^3 for Euro 6 vehicles. Switzerland uses a three-measurement approach at idle and elevated idle, with different thresholds depending on operating condition [30], [31]

These variations demonstrate that, despite the common legislative framework, there is still no fully standardised PTI methodology across the EU, particularly for advanced emissions measurements.

2.3.5 Challenges in Implementing Effective Periodical Technical Inspections

One of the main challenges in PTI implementation lies in the limited effectiveness of currently available methods for detecting modern emissions-related failures. On-Board Diagnostics (OBD), although potentially useful, do not always identify malfunctioning or tampered aftertreatment systems. Several studies have shown that vehicles with high emissions may not trigger any diagnostic trouble codes, thereby reducing the reliability of OBD-based inspections as a standalone method [32], [33], [34].

Another important challenge concerns the introduction of more accurate methods, such as SPN measurement. Although these methods provide significantly better detection capability, they also introduce higher equipment costs, stricter calibration requirements, and greater dependence on operator training. These factors create practical barriers to large-scale implementation, particularly in inspection systems designed for fast and low-cost operation [35].

2.3.6 Future of Periodical Technical Inspections in the EU

The future development of PTIs in the EU is expected to involve the gradual incorporation of more advanced and representative emissions measurement techniques. In particular, the ongoing revision of the European roadworthiness framework is considering the inclusion of NOx measurements, reflecting the growing importance of these pollutants in urban air quality and public health [32].

At the same time, new approaches such as On-Board Monitoring (OBM) and remote sensing are being explored as potential tools for complementing conventional inspections. These methods may allow broader emissions surveillance, improved detection of malfunctioning vehicles, and more effective control of in-service emissions over time [36].

2.3.7 Particulate Matter Emissions in Periodical Technical Inspections

PM emissions from diesel vehicles remain one of the main concerns in PTI development, particularly due to the limitations of traditional opacity-based methods. DPFs have significantly reduced particulate emissions in modern vehicles, but their malfunction or removal continues to be a relevant issue in real-world operation.

Historically, PTIs have relied on opacity meters to assess diesel particulate emissions. These instruments estimate the amount of soot in the exhaust by measuring light attenuation. Although this method is simple and low-cost, it is not sufficiently sensitive to identify many DPF failures, especially in vehicles equipped with more advanced aftertreatment systems [1], [26];

Solid Particle Number Measurement in Periodical Technical Inspections

To overcome these limitations, several countries have begun to adopt SPN measurement. Unlike opacity testing, SPN directly quantifies the number of solid particles above a given size threshold, providing a much more representative evaluation of particulate emissions and filter efficiency [18], [19]. This method is particularly effective in identifying vehicles with damaged, tampered, or removed DPFs.

SPN measurement may be implemented using technologies such as diffusion chargers, condensation particle counters, and systems incorporating evaporation tubes or catalytic strippers to remove volatile components from the sample. These approaches improve measurement specificity and align PTI procedures more closely with regulatory emissions assessment principle [27], [28].

However, several challenges remain regarding the widespread implementation of SPN in PTIs. These include the lack of harmonised procedures across Member States, differences in test duration and operating conditions, equipment cost, calibration requirements, and variability in instrument performance [29]. Some studies have also shown that detection limits and response times differ significantly between available instruments, affecting repeatability and reliability of the measurements.

- Future developments in particulate assessment during PTIs are expected to involve better integration between inspection equipment and vehicle systems, improvements in low-cost particle measurement technologies, and possible use of complementary approaches such as PEMS or remote sensing for large-scale emissions screening [32], [37]

2.3.8 Nitrogen Oxides Emissions in Periodical Technical Inspections

NOx are among the main pollutants from road transport in the EU. NOx significantly contributes to air pollution and has direct impacts on public health, especially in urban areas. According to the European Environment Agency, road transport accounted for 37% of NOx emissions in the EU-27 in 2020 [38].

Although Euro standards have progressively reduced NOx limits and promoted the adoption of systems such as SCR, ensuring the continued performance of these systems throughout vehicle life remains a challenge [39]. For this reason, the inclusion of NOx measurements in PTIs has become an increasingly relevant topic.

At present, Directive 2014/45/EU does not mandate NOx measurement during PTIs [17]. However, proposals under discussion in the context of the roadworthiness package revision aim to introduce practical methodologies capable of evaluating the proper operation of SCR and other NOx control systems [40].

Different approaches have been proposed for NOx assessment during PTIs. These include laboratory-grade chemiluminescence detectors, portable systems based on non-dispersive ultraviolet spectroscopy (NDUV), direct readings from automotive NOx sensors, indirect estimation methods based on the CO_2/NOx ratio, and hot-idle testing strategies [41],[42][43],[44] Studies have shown that hot-idle NOx measurements can effectively distinguish between vehicles with properly functioning SCR systems and those with defective aftertreatment performance [45].

2.3.8.1 Challenges in NOx Measurement for PTIs.

Despite this potential, several technical difficulties remain. These include differences between aftertreatment technologies, sensor degradation over time, the need to ensure adequate SCR operating temperature, implementation cost, and the possibility of tampering with emissions control systems [41]

Therefore, although NOx measurement in PTIs is technically feasible, its effective large-scale implementation still requires further methodological harmonisation and validation [26], [46], [47];

2.3.9 Chapter review

The literature review conducted throughout this chapter highlighted the complexity associated with the formation of emissions in internal combustion engines, as well as the evolution of aftertreatment systems developed to mitigate their environmental impact.

It was observed that the formation of pollutants such as CO, HC, PM, and NOx is strongly dependent on combustion conditions, namely the air–fuel ratio, temperature, and mixture homogeneity. These factors directly influence the effectiveness of emission control systems, making their management a multidimensional problem involving both chemical and thermal phenomena.

The analysis of aftertreatment systems showed that currently implemented solutions, such as TWC, DPF, and SCR, achieve high efficiency when operating under ideal conditions. However, their performance is highly dependent on variables such as temperature, operating regime, and component degradation, which may lead to significant deviations between expected behaviour and real-world performance.

Within the context of periodic technical inspections in the European Union, relevant limitations were identified in the methods currently employed. In particular, conventional approaches show reduced capability to detect failures in modern emission control systems, as well as to accurately represent real vehicle operating conditions. Additionally, the lack of harmonisation among Member States contributes to variations in the effectiveness of inspection procedures.

On the other hand, more advanced measurement solutions, although technically more robust, present limitations related to cost, complexity, and large-scale applicability. This reality highlights the existence of a trade-off between measurement accuracy and implementation feasibility, which constrains the development of new approaches in emissions monitoring.

In summary, the analysed literature demonstrates that, despite significant technological and regulatory advancements, important gaps remain in the assessment of emissions under real operating conditions. These limitations justify the need for the development of alternative solutions capable of improving measurement representativeness and reliability, while maintaining acceptable levels of complexity and cost.

3 Measurement Systems

This chapter presents the development of the exhaust gas measurement system proposed in this work, addressing in an integrated manner the design, component selection, implementation, and system architecture aspects. Following the critical analysis of existing methods presented in the previous chapter, the need for a solution that combines portability, low cost, and the ability to operate under real-world conditions becomes evident.

In this context, the main objective of this chapter is to justify the technical choices made and to describe the development process of a system capable of measuring key exhaust gas parameters, namely mass flow rate, temperature, and NOx concentration. The adopted approach is based on the integration of different subsystems, including sensors, data acquisition electronics, communication interfaces, and embedded processing.

Initially, an analysis of existing measurement systems, such as PEMS and SEMS, is presented, highlighting their advantages and limitations, and establishing the framework for the proposed solution. This is followed by a description of the overall system architecture, including its main modules and the interactions between them.

The chapter then proceeds with a detailed description of the different system components, namely the NOx measurement module, the microcontroller, the Venturi-based flow measurement system, the selected sensors, CAN communication, and the PCB development. Mechanical and manufacturing aspects are also addressed, along with the implementation of the firmware responsible for data acquisition, processing, and transmission.

Finally, the structure of the embedded software is presented, including task organization and the functional flow of the system, enabling a clear understanding of how data are acquired, processed, and made available for analysis.

This chapter therefore constitutes the technical core of the developed work, establishing the link between the theoretical foundations presented previously and the experimental validation discussed in the following chapter.

3.1 Exhaust Gas Measurement Devices

3.1.1 Portable Emissions Measurement Systems (PEMS)

PEMS are widely used for the measurement of gaseous emissions under real driving conditions. These systems enable the direct quantification of pollutants such as NOx, total HCs and CO, providing results that are representative of real vehicle operation outside laboratory environments.

PEMS are typically based on high-precision measurement techniques, such as chemiluminescence detection for NOx, ensuring high accuracy and reliability. These systems are used in regulatory contexts, including in-service conformity testing of vehicles, particularly under Euro VI requirements.

Despite their accuracy, PEMS present several limitations. Their operation is generally restricted to predefined test routes and relatively short durations, typically covering only a few hours of vehicle operation. As a result, they may not fully capture the variability of real-world driving conditions over extended periods.

Furthermore, PEMS systems are typically complex and expensive, limiting their applicability in widespread or low-cost monitoring scenarios. These limitations motivate the development of alternative solutions capable of providing continuous or more flexible emissions monitoring [3], [48]

3.1.2 Smart Emissions Measurement System (SEMS)

SEMS are sensor-based systems designed for long-term monitoring of vehicle emissions under real-world operating conditions. Unlike PEMS, SEMS are intended to operate continuously over extended periods, enabling the collection of large datasets representative of typical vehicle usage.

These systems rely on integrated sensors installed in the exhaust system, including NOx sensors, NH_3 sensors, and temperature sensors. Additional components, such as Global Positioning System (GPS) modules and data acquisition units, allow for the correlation of emissions data with vehicle operation parameters. Data acquisition is typically performed at low sampling frequencies, such as 1 Hz, and transmitted periodically for post-processing and analysis.

Although SEMS provide valuable insight into long-term emissions behaviour, they rely on automotive-grade sensors, which generally offer lower accuracy compared to laboratory-grade instrumentation. Additionally, the integration of sensors directly into the exhaust system may require modifications to the vehicle, limiting the flexibility of the system when applied across different platforms [48]

3.1.3 Flow Measure

The measurement of exhaust gas mass flow rate is a fundamental aspect in the characterization of emissions from internal combustion engines, since the determination of pollutant mass emissions requires the simultaneous knowledge of both gas concentration and volumetric or mass flow rate. Under real operating conditions, particularly in transient regimes, both the composition and the flow rate of exhaust gases vary continuously with engine load and speed, making their measurement a significant technical challenge [49].

Direct measurement of exhaust gas flow presents considerable difficulties due to the specific characteristics of this type of flow, namely the presence of condensable water vapor, particulate matter, rapid variations in temperature and chemical composition, as well as the pulsating nature of the flow, including possible flow reversal at low engine speeds. These conditions limit the applicability of several conventional flow measurement techniques[49].

One of the most commonly used approaches in PEMS is based on Pitot tubes. These devices estimate flow velocity from differential pressure measurements using Bernoulli's equation. However, their application to exhaust gases presents important limitations. On one hand, the nonlinear relationship between differential pressure and flow rate (square root dependency) introduces significant errors under pulsating flow conditions, making the determination of the average flow more complex. On the other hand, measurement accuracy is highly dependent on calibration, sensor positioning, and the quality of the differential pressure measurement, being particularly sensitive to offset errors and noise [49].

Another possible approach would be the use of air mass flow sensors, such as hot-wire or hot-film sensors. However, these are not suitable for exhaust line applications due to the high temperatures and the presence of particulate matter, which lead to sensor fouling and progressive degradation of performance. Additionally, these sensors are typically designed for clean air intake conditions and not for harsh exhaust environments.

Given these limitations, differential pressure-based flow meters, such as orifice plates, nozzles, and Venturi tubes, emerge as robust and suitable solutions for this type of application. These devices operate by introducing a restriction in the flow, generating a pressure difference between two sections of the duct, which is directly related to the fluid velocity through Bernoulli's principle.

Among these solutions, the Venturi tube stands out due to its lower permanent pressure losses and improved flow stability when compared to more abrupt restrictions such as orifice plates. Its converging-diverging geometry allows for a controlled acceleration of the fluid up to the throat section, where maximum velocity and minimum pressure occur, enabling accurate flow estimation based on the measured pressure differential.

Furthermore, the Venturi offers several advantages for exhaust gas applications, including:

- reduced susceptibility to particle deposition due to the absence of sharp edges;
- high robustness under elevated temperature conditions;
- lower sensitivity to flow disturbances when properly designed;
- straightforward integration with differential pressure sensors.

Therefore, the use of a Venturi tube represents a technically sound solution for exhaust gas flow measurement, providing a reliable estimation of the flow rate with a suitable balance between accuracy, robustness, and cost. This justifies its implementation in the developed system, particularly considering the requirements of portability and operation under real driving conditions.

3.1.4 Exhaust Gas Measurement Devices Analysis

Both PEMS and SEMS present distinct advantages and limitations. PEMS systems provide high measurement accuracy and are suitable for regulatory and validation purposes, but are limited in duration, flexibility, and cost. In contrast, SEMS systems enable long-term monitoring and continuous data acquisition but typically suffer from lower accuracy and require permanent or semi-permanent installation.

Within the scope of this work, the objective is to develop a portable, flexible, and cost-effective measurement system capable of operating across different vehicles without requiring permanent modifications. In this context, the PEMS concept provides a more suitable reference framework, particularly due to its portability and ability to perform measurements without interfering with the original vehicle architecture.

However, unlike conventional PEMS systems, the proposed solution aims to achieve a balance between accuracy, cost, and flexibility by integrating low-cost sensors with a dedicated data acquisition system. This approach enables the development of a simplified PEMS-like system, capable of providing relevant emissions data while maintaining portability and adaptability across different test scenarios.

3.2 System Design and Architecture

The system developed in this work was designed to measure exhaust gas flow rate, temperature, and NOx emissions, enabling its operation both in laboratory environments and under real driving conditions. The main objective was to create a portable, flexible, and cost-effective solution capable of acquiring and transmitting relevant emissions data.

The system architecture is based on a modular approach, integrating sensing elements, signal conditioning, data acquisition, and communication interfaces. The key components of the system include exhaust gas sensors, a Venturi-based flow measurement device, a dedicated Printed Circuit Board (PCB), a microcontroller for data processing, and communication modules based on the CAN protocol.

The flow rate is determined using a Venturi element, allowing indirect measurement based on the pressure differential and exhaust gas temperature. This approach enables a compact and low-cost solution compared to conventional flow measurement systems.

The acquired signals are conditioned and processed by the electronic hardware, and subsequently handled by the microcontroller, which is responsible for data acquisition, processing, and transmission. Communication with external systems, such as dataloggers or laboratory test benches, is performed through CAN interfaces, ensuring compatibility with automotive communication standards.

The system is powered by a 12 V supply, allowing operation either through the vehicle battery or an external power source. Additionally, a dedicated mechanical enclosure was developed to integrate all components, ensuring protection, portability, and ease of installation across different test scenarios.

It should be noted that particulate matter (PM) measurement was not included in the current system configuration. This decision was primarily driven by the high cost associated with particle measurement sensors, which represent one of the most expensive components in emissions measurement systems. Therefore, a phased development approach was adopted, prioritising the validation of the overall system architecture and core measurement functionalities before integrating additional sensors. As shown in Figure 9.

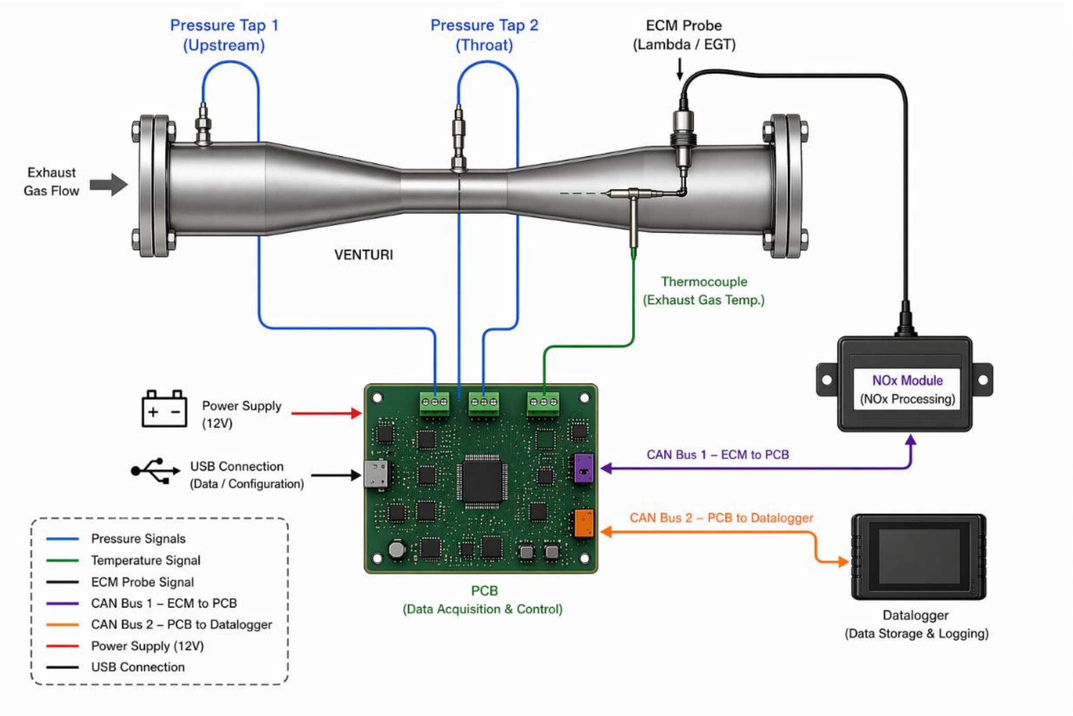

Figure 9 - System Design and Architecture (Image generated using artificial intelligence (AI))

3.2.1 NOx Modules

For the implementation of a PEMS, A market analysis was conducted and, considering the price–performance ratio and compliance with the project requirements, the ECM NOxCAN, Type T (NOxCANt) sensor was selected. At the moment, only the NOx measurement module is available; however, the modular architecture allows for system expansion with other compatible modules, which communicate in parallel over the same Controller Area Network (CAN) communication bus.

The module currently in use is the ECM NOxCAN, Type T (NOxCANt) a versatile and highly integrable device designed for the accurate measurement of NOx, lambda ratio, and O_2 in engine development and emissions aftertreatment applications. This module uses a Type T ceramic NOx sensor, which is installed directly in the engine exhaust system. The measured data including NOx concentrations, lambda values, O_2 levels, and additional sensor parameters are transmitted via the CAN interface.

The NOxCANt is compatible with all types of engines and combustion systems. A relevant point is the Type T sensor's cross-sensitivity to NH_3, with a 1:1 ratio, meaning 1 ppm of NH_3 is interpreted as 1 ppm of NOx by the sensor. Despite this characteristic, the Type T sensor is recommended for general applications.

The ECM NOxCANt module offers high-performance specifications suitable for demanding testing environments. It features a response time of less than 1 second for NOx measurements and under 150 ms for lambda (λ), air-fuel ratio (AFR), equivalence ratio (φ), and O_2 readings. The system supports various fuel types through programmable H:C, O:C, and N:C ratios, as well as compatibility with hydrogen (H_2). Power requirements range from 11 to 28 VDC, with a steady-state current draw of 1.2 A at 12V and a start-up peak of 4 A for 30 s. The sensor mounts using an 18 mm x 1.5 mm thread for NOx and a 1/4" NPT/ISO fitting for pressure. The module dimensions are 145 mm x 120 mm x 40 mm, with a sensor cable length of 0.6 m (sensor side), plus a standard 2 m extension (3 m optional). The electronics are rated for operating temperatures from -55°C to +125°C and meet IP67 standards, while the sensor itself can withstand continuous operation at temperatures up to 850°C.

It is possible to integrate additional modules in parallel with the ECM, enabling the analysis of other compounds in the exhaust gases, should there be a future need to expand the set of monitored variables beyond NOx.

According to the datasheet, the NOx sensor requires a stabilization period of approximately 30 minutes before the start of each test, in order to ensure that it reaches and maintains its nominal operating temperature. This condition is critical, since the measurement principle, typically based on an electrochemical cell, is highly temperature-dependent, directly influencing sensitivity, response time, and the accuracy of NOx readings.

3.2.2 Microcontroller

The central processing unit of the developed system is based on the ESP32-S3-WROOM-1 microcontroller. This device was selected due to its high processing capability, integrated communication interfaces, and suitability for embedded applications requiring real-time data acquisition and processing.

The ESP32 architecture provides sufficient computational resources to handle multiple simultaneous tasks, including sensor data acquisition, signal processing, and communication with external systems. Its support for C++ programming enables the implementation of structured and modular firmware, facilitating system scalability and maintainability.

One of the key factors in the selection of this microcontroller was the availability of multiple communication interfaces. In this system, two independent CAN channels are required: one dedicated to communication with the ECM measurement modules and another for communication with external systems, such as a datalogger or laboratory test bench. This separation ensures reliable data exchange and avoids communication conflicts between subsystems.

Communication with the CAN controllers is performed via the Serial Peripheral Interface (SPI), allowing high-speed and efficient data transfer between the microcontroller and the MCP2515 CAN modules. This configuration provides flexibility in system design while maintaining compatibility with automotive communication standards.

In addition to communication tasks, the microcontroller is responsible for acquiring analog and digital signals from the sensors, performing data processing, and formatting the data for transmission. The system operates under conditions that require consistent timing and reliable data handling, particularly during transient engine operation.

Although a full real-time operating system (RTOS) is not explicitly required, the system is designed following structured task separation principles, ensuring that critical operations such as data acquisition, communication, and processing are executed without interference. This approach enables deterministic behaviour and supports future implementation of real-time scheduling if required.

Overall, the ESP32-S3 provides a balanced solution in terms of performance, flexibility, and integration capability, making it suitable for the development of a PEMS.

3.2.3 Venturi-Based Flow Measurement

To determine the exhaust gas mass flow rate, a Venturi-based measurement approach was adopted. This method was selected due to its robustness, simplicity, and suitability for high-temperature and particle-laden flows, such as those found in engine exhaust systems. Compared to alternative flow measurement techniques, such as orifice plates or hot-wire sensors, the Venturi offers lower permanent pressure losses and improved reliability under harsh operating conditions.

The design and dimensioning of the Venturi were carried out in accordance with ISO 5167-1:2022 and ISO 5167-4:2022 standards, which define the geometric requirements and calculation methodology for differential pressure flow measurement devices. These standards ensure that the flow rate can be determined with acceptable accuracy based on the measured pressure differential [50], [51].

The mass flow rate is calculated using the following expression:

$$q_m = \frac{C}{\sqrt{1-\beta^4}} \times A_t \times \varepsilon \times \sqrt{2\Delta p \rho} \tag{1}$$

where:

q_m = Mass flow rate (kg/s)

C = Discharge coefficient (dimensionless, typically 0.995 for machined Venturis)

At = Throat section area (m²)

ε = Expansibility factor

ρ = Fluid density (kg/m³) before the Venturi

Δp = Differential pressure (P1−P2), measured between the sensors before and inside the throat (Pa)

β = Ratio between the throat diameter and the inlet diameter

The expansibility factor ε is determined by the following equation:

$$\varepsilon = 1 - \left(0.351 + 0.256\beta^{4} + 0.93\beta^{8}\right) \times \frac{\Delta p}{P_1 \gamma} \tag{2}$$

where:

γ = Adiabatic coefficient of the fluid

Since the fluid density varies with temperature, it can be calculated as:

$$\rho = \frac{P_1}{RT_1} \tag{3}$$

where:

P_1 = Pressure at the Venturi inlet (Pa)

T_1 = Temperature at the Venturi inlet (K)

R = Specific gas constant (J/kg·K)

This formulation allows the estimation of mass flow rate based on pressure and temperature measurements, making it suitable for integration with the selected sensors.

3.2.3.1 computer aided design (CAD) model

A three-dimensional model of the Venturi was developed for both design and simulation purposes. The geometry was defined according to ISO recommendations, with a converging section angle of 21° and a diverging section angle of 11°, ensuring stable flow acceleration and pressure recovery.

The inlet diameter was set to 60 mm, while the throat diameter was defined as 28 mm, resulting in a diameter ratio (β) suitable for the expected operating conditions. The model was created using SolidWorks, and the detailed technical drawing is provided in attachment A. As shown in Figure 10.

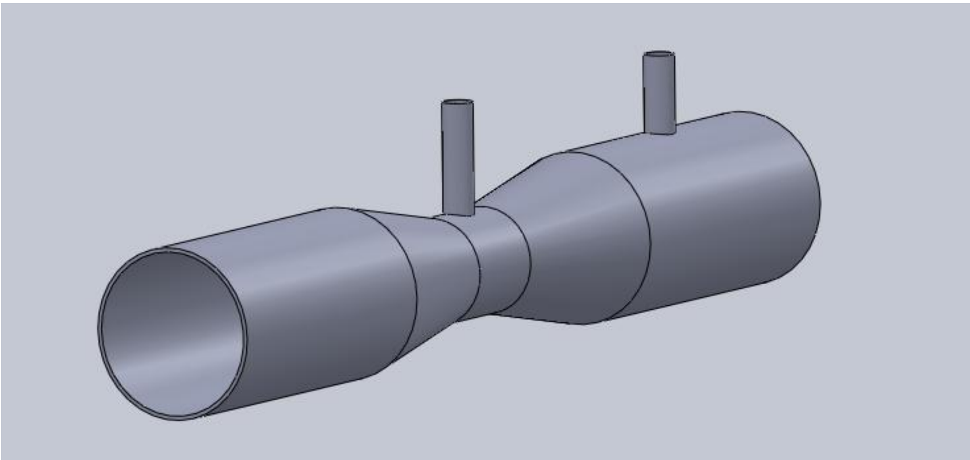

Figure 10 - Venturi cad model

The model was then imported into SpaceClaim, where names and properties were assigned to the faces of each object and volume. This step was essential for organizing the geometric model and preparing the different domains for the subsequent stages of mesh generation and boundary condition definition in the CFD simulator (Figure 11).

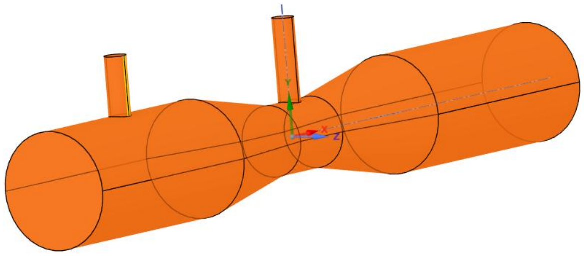

Figure 11 - Venturi in SpaceClaim

3.2.3.2 CFD Analysis and Design Validation.

To validate the Venturi design and assess its performance under different operating conditions, a CFD study was conducted. The objective was to evaluate the pressure differential range, flow behaviour, and thermal conditions within the device, ensuring compatibility with the selected sensors.

The simulation model was prepared by defining the fluid domain, boundary conditions, and mesh characteristics. Special attention was given to mesh refinement in critical regions, such as the throat section, to ensure accurate capture of velocity and pressure gradients.

The CFD analysis allowed the estimation of the expected pressure differential across a range of flow conditions, providing essential input for sensor selection. Additionally, the temperature distribution was analysed to verify that the operating conditions would not exceed the limits of the measurement components.

Local Sizing Setup

A local mesh refinement was applied in the regions of greatest interest, such as the area adjacent to the Venturi. This refinement was essential to improve accuracy in capturing critical fluid phenomena (Figure 12).

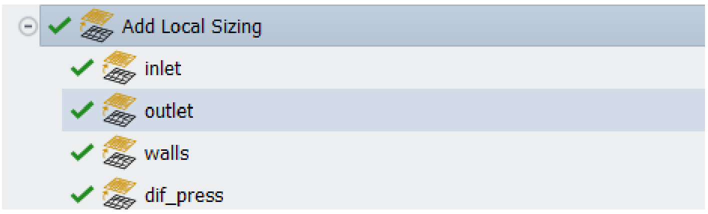

Figure 12 - Local Sizing setup

The parameters of the initial mesh before refinement were:

As a result, a total of 882664 elements was obtained.

Geometry Type Setup

A physical description of the problem was carried out. Since, in this case, there was only a fluid mesh volume and no solid region, the option "geometry consists of a single fluid region" was selected (Figure 13).

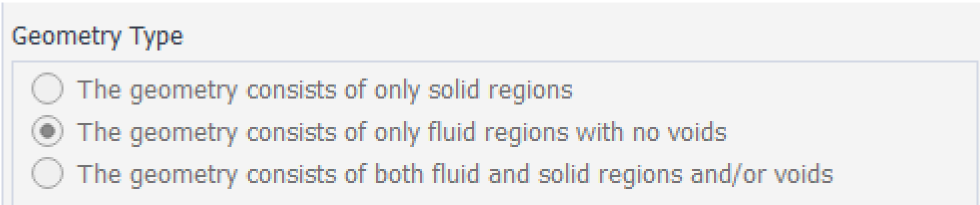

Figure 13 - Geometry type setup

Boundary Layer Setup

To properly capture the gradients near solid surfaces, such as the walls of the venturi, a boundary layer was added. This layer enabled adequate resolution of the boundary layer, ensuring greater reliability in the analysis of the flow near the surfaces (Figure 14).

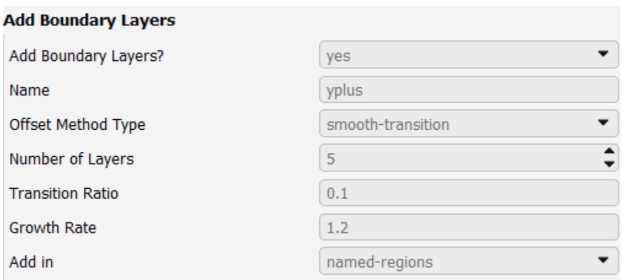

Figure 14 - Boundary layer setup

Volume Mesh Definition

After applying the necessary refinements and configurations, the volume mesh was generated, ensuring continuity and quality of the discretization throughout the computational domain. The resulting mesh was evaluated for quality, ensuring that parameters such as orthogonality and skewness remained within acceptable limits (Figure 15).

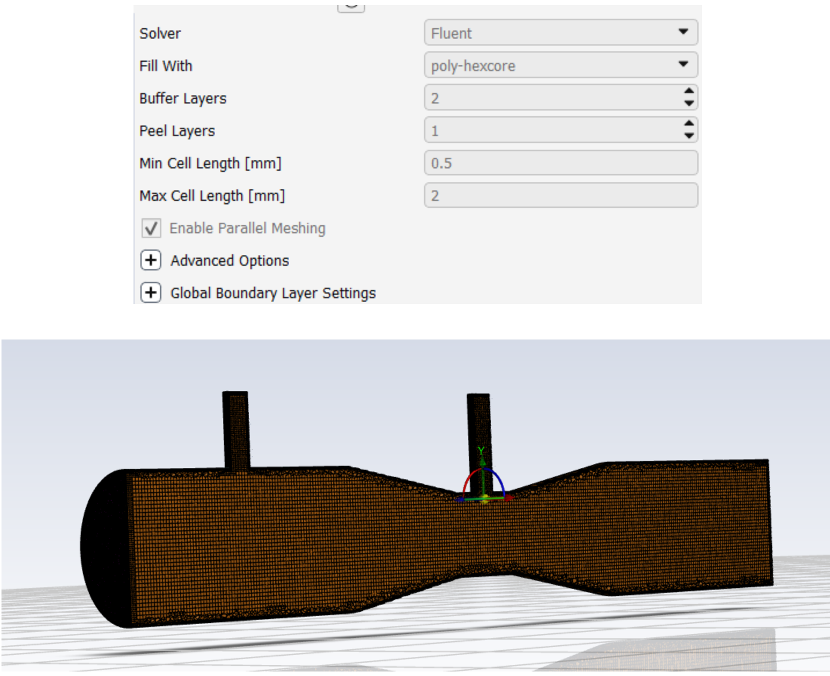

Figure 15 - Volume mesh definition

Simulation Characterization

The simulation setup is a crucial step in defining the computational scenario and the conditions governing the flow and thermal phenomena within the study domain. In this work, the essential parameters were configured in the Fluent software to ensure the accuracy and relevance of the results obtained.

Initially, the type of flow regime to be analyzed was defined, adjusting the simulation conditions to the expected behavior of the fluid. The energy mode was activated to enable the thermal equations, allowing for a detailed analysis of heat transfer.

Next, the boundary conditions were established, including:

• The thickness of the aluminum walls;

• The exterior temperature on the inlet and outlet walls;

• The fluid inlet velocity and outlet pressure.

To ensure an accurate numerical solution, the convergence criteria for residuals were adjusted. After configuring all the parameters and conditions, the calculation was started, allowing for the analysis of fluid behavior and heat transfer within the system.

Boundary Conditions

The following boundary conditions were defined:

To calculate the flow rate, it is necessary to determine the differential pressure in the venturi. For this, the theoretical maximum pressure difference was calculated for an extreme case, considering a 3500 cc engine, 4 strokes, at 10000 RPM with an extra bar of pressure.

In this equation, the boost (turbo) pressure enters as a constant, derived from the dimensionless pressure coefficient.

The maximum flow rate is determined using the following equation:

$$\dot{Q} = CC\ [m^3] \times nº\ of\ Cycles\ per\ min \times\ P_{turbo}$$

For a 4 stroke engine

$$\dot{Q} = \frac{CC\ [m^3] \times RPM \times P_{turbo}}{60 \times 2} \tag{4}$$

$$\dot{Q} = \frac{0.003500 \times 10000 \times\ 2}{120}$$

$$\dot{Q} = 0.583\ [\frac{m^3}{s}]$$

With the flow rate known, it was possible to calculate the intake velocity by dividing it by the cross-sectional intake area.

$$A_{inlet} =\ \pi \times\ r^2 = 0.005\ m^2 \tag{5}$$

$$V_{inlet} = \frac{0.583}{0.005} = 116.6\ \frac{m}{s} \tag{6}$$

To verify whether the system is functional for smaller engines and at lower engine speed, the same methodology was used to calculate the flow rate and intake velocity for a naturally aspirated 1000 cc engine running at 1000 RPM.

This resulted in a flow rate of 0.0073 m^3/s and an intake velocity of 1.46 m/s.

An exhaust gas temperature of 300 °C was defined, as according to reference [52] the average temperature during the regeneration process of a particulate filter is approximately at this level.

Y plus

To properly study the boundary layer around the Venturi, boundary layers were added around it. An expansion factor of 1.2 was used, with the first layer positioned at 0.1 mm from the surface of the venturi. This refinement consisted of 5 layers, as shown in Figure 16.

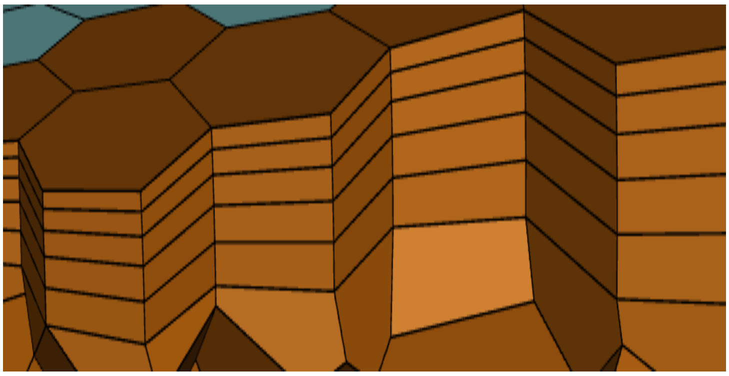

Figure 16 - Yplus setup

After the simulation, a y+ value of approximately 1.9 was obtained, indicating that the boundary layer resolution was adequate to capture the flow phenomena near the surface of the venturi (Figure 17)

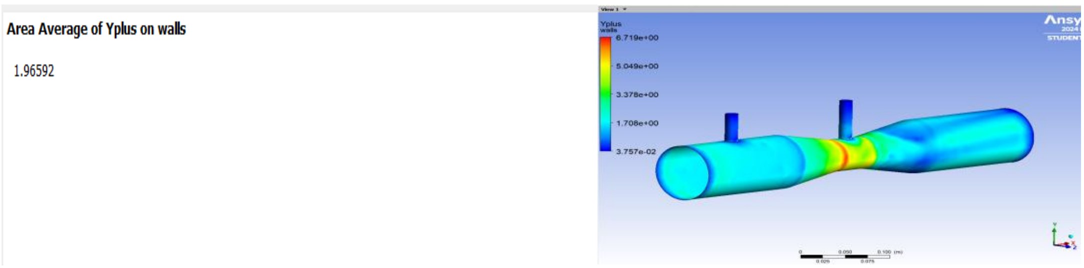

Figure 17 - Yplus result

Mesh Sensitivity Analysis

To carry out the mesh dependency study, the pressure differential was used as the reference variable, as it can be analytically estimated using the Bernoulli equation, allowing comparison between simulated values and those obtained as the number of elements was increased.

To establish a theoretical reference value for the pressure differential, the incompressible Bernoulli equation, presented in Equation (7), was employed. This equation is not intended to accurately model the real compressible flow inside the venturi, where the local Mach number approaches unity at the throat, but rather to provide a conservative upper bound serving as a comparison criterion in the mesh independence study.

Bernoulli equation

$$\Delta p = \frac{1}{2}\rho\left({V_2}^2 - {V_1}^2\right) \tag{7}$$

- $\Delta p -$ Pressure Differential
- $\rho -$ Air Density
- $V_2 - Throat\ Velocity$
- $V_1 - Inlet\ Velocity$

By the continuity equation.

$$V_2 = V_1\left(\frac{D_1}{D_2}\right)^2 \tag{8}$$

- $D_1 - Inlet\ Diameter$
- $D_2 - Throat\ Diameter$

A velocity at the throat section of $V_2 = 322.22$ m/s was considered. This value represents an extreme condition, close to the speed of sound, and is therefore unrealistic in practical terms, corresponding instead to a theoretical worst-case scenario used for conservative analysis.

Assuming a fluid density of $\rho = 0.6159$ kg/m^3, a reference pressure differential of approximately $\Delta p \approx 27.8$ kPa was obtained.

Thus, a reference value for the pressure differential was established and used as a comparison criterion in the mesh independence study. This parameter made it possible to assess whether the mesh refinement was sufficient to accurately reproduce the pressure gradient in the flow through the Venturi.

Additionally, the relative error between the reference value and the numerically obtained values was calculated, as presented in Table 3 and Figure 18.

Table 3 - Results of Mesh sensitivity analysis

Element numbers	***Differential pressure [kPa]***	***Error %***
41267	20	42.3
55341	19.6	42.0
70480	30.86	-9.9
89286	31.25	-11.1
116055	21.04	32.2
146734	30.86	-9.9
191118	43.40	-35.9
242740	38.62	-28.0
314384	25.64	8.4
407935	32.48	-14.4
562628	26.47	5.0
882264	27.96	-0.6

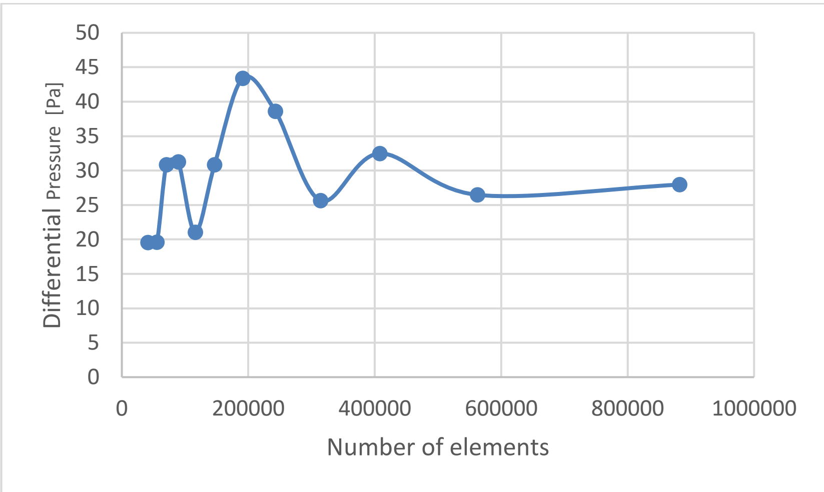

Figure 18 - Mesh sensitivity results

The expected behaviour for this type of analysis was observed: as the number of mesh elements increased, the pressure differential values showed a tendency to stabilise, indicating a trend towards mesh independence and increasing confidence in the obtained results.

However, the limitation on the number of elements imposed by the student license represented a relevant constraint, as it prevented further mesh refinement to confirm numerical convergence. Therefore, it is not possible to unequivocally guarantee that the observed stabilisation corresponds to true mesh independence, and it may instead represent an apparent stabilisation.

Despite this limitation, the obtained pressure differential value showed good agreement with the theoretical value, reinforcing the consistency of the results. As shown in Figure 19.

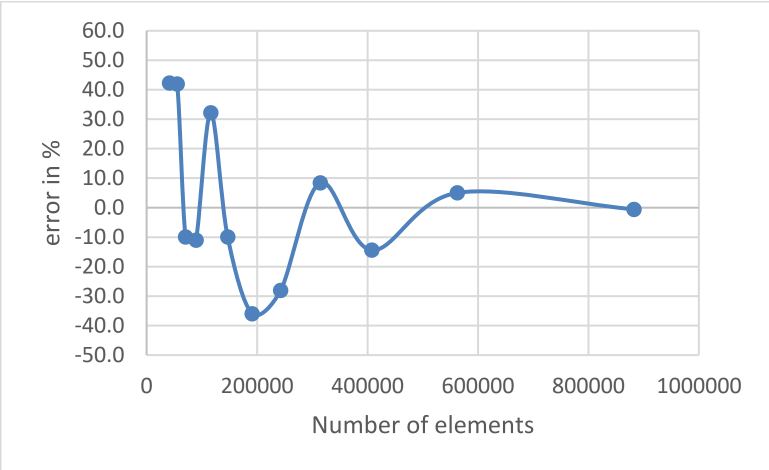

Figure 19 - Mesh sensitivity error

Venturi-Based Flow Measurement Results

In this subsection, the results obtained from the CFD simulations will be presented and discussed. The analysis will focus on the temperature, pressure, and velocity fields in order to determine the most suitable strategy to adopt. The boundary conditions used were an inlet temperature of 300 °C for both simulations, and inlet velocities of 116 m/s and 1.46 m/s, as described in section Boundary Conditions.

as it suggests that no additional cooling systems are required before the gases reach the sensors.

For the condition of 116 m/s, starting with the analysis of the temperature field, it is observed that the venturi effectively dissipates heat, preventing any significant temperature rise in the outlet region where the pressure sensor is located. This is a positive outcome. As shown in Figure 20.

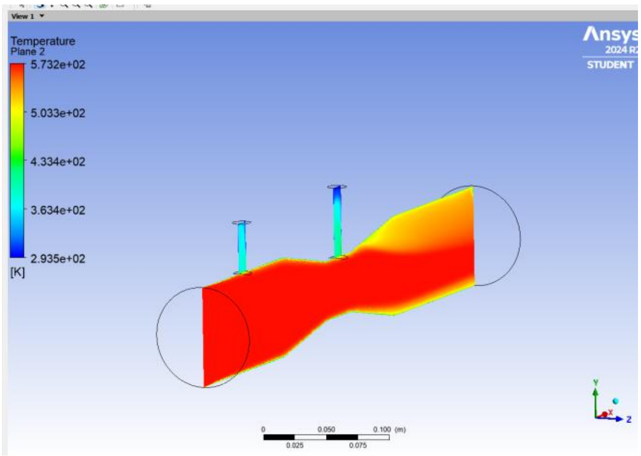

Figure 20 - Temperature field with 116 m/s inlet velocity

Regarding the pressure field, it is observed that the pressure at the sensor outlet remains nearly static, which is ideal for the proper operation of the system. A pressure differential of approximately 0.28 bar was recorded. As shown in Figure 21.

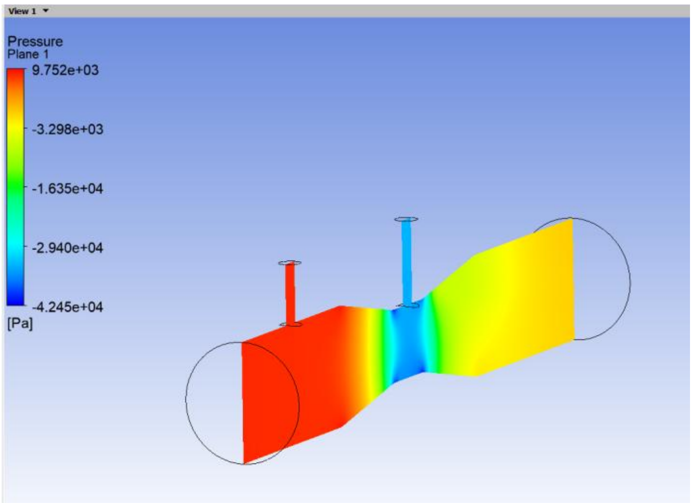

Figure 21 - pressure field with 116 m/s inlet velocity

The analysis of the velocity field further reinforces confidence in the results, as the streamlines behave as expected, showing an increase in velocity at the venturi throat. As shown in Figure 22.

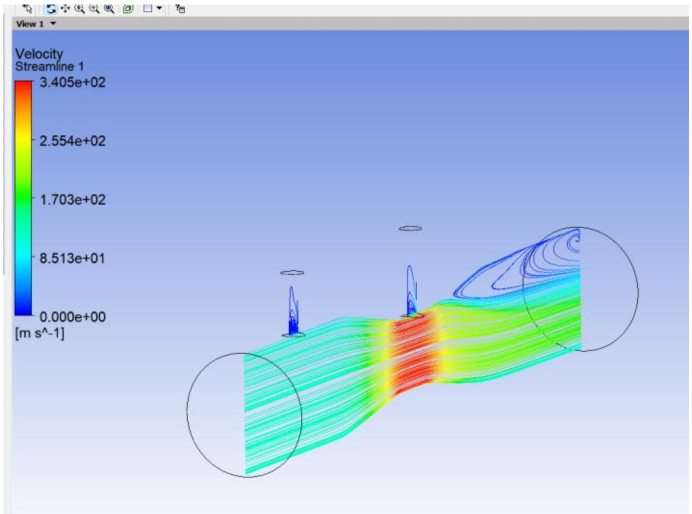

Figure 22 - velocity field with 116 m/s inlet velocity

For the condition of 1.46 m/s, it is observed that the system, as in the case of 116 m/s, is able to effectively dissipate the heat, as demonstrated in Figure 23.

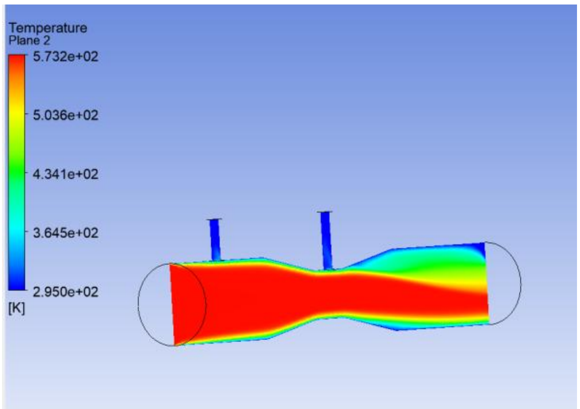

Figure 23 - Temperature field with 1.46 m/s inlet velocity

The pressure field results indicate that the system will not be able to operate effectively with such low inlet flow rates. Based on the design and characterization of the venturi, the pressure differential obtained was approximately 6 Pa (0.00006 bar), an extremely low value that is virtually undetectable by standard pressure sensors due to their limited accuracy. As shown in Figure 24.

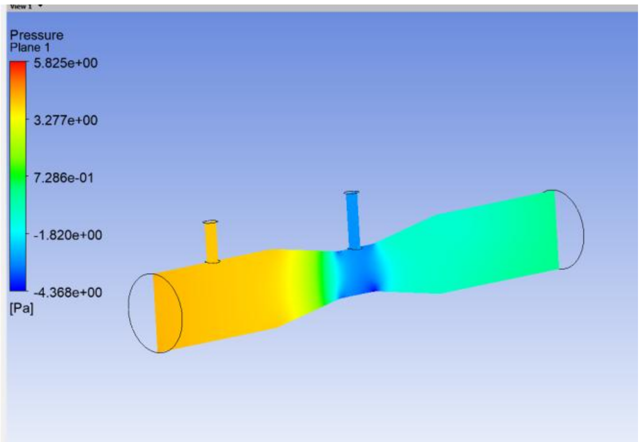

Figure 24 - pressure field with 1.46 m/s inlet velocity

The velocity field results once again reinforce confidence in the accuracy of the obtained data As shown in Figure 25.

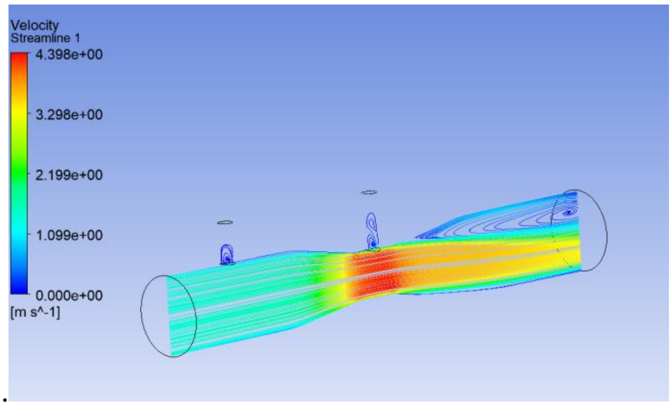

.

Figure 25 - velocity field with 1.46 m/s inlet velocity

As evidenced by the results, this solution is not suitable for implementation, as it proves to be inefficient for lower engine displacements and operating speeds. To address this issue, the most appropriate approach was to characterize multiple venturis, tailored to different engine displacement ranges and to whether the engine is turbocharged or naturally aspirated.

Venturi Subchapter Conclusion

Based on the results obtained, it can be concluded that the designed Venturi exhibits appropriate performance under high flow conditions, ensuring a measurable pressure differential consistent with theoretical predictions, as well as a stable and predictable flow behaviour. The CFD analysis further demonstrated that the system does not present significant thermal limitations for the selected instrumentation, indicating that the exhaust gas temperature does not compromise sensor operation.

Additionally, the study made it possible to characterise the range of pressure differentials across different operating conditions, enabling the appropriate selection of differential pressure sensors.

However, under low flow regimes, the generated pressure differential is insufficient to ensure reliable measurement using conventional sensors, thus limiting the applicability of the system in such conditions.

Therefore, it is concluded that the adopted solution requires the use of multiple Venturi geometries, tailored to the engine operating range (displacement and speed), in order to ensure accuracy and robustness in flow measurement across the full operating spectrum.

3.2.4 Sensors

The selection of sensors is a critical aspect of the developed system, as it directly affects measurement accuracy, reliability, and overall system performance. In this work, sensors were selected based on their compatibility with the expected operating conditions, particularly in terms of pressure range, temperature limits, and response time.

The selection process was supported by the CFD analysis described in Section 3.2.3.2, which allowed the estimation of the expected pressure differential and temperature ranges within the Venturi. These results were used to ensure that the selected sensors operate within their specified measurement ranges, avoiding saturation or insufficient resolution.

Differential Pressure Sensor

Based on the CFD results, the expected pressure differential varies significantly depending on engine operating conditions...

The differential pressure sensor is used to measure the pressure drop across the Venturi, which is required for the calculation of the exhaust gas mass flow rate. In this work, a sensor with a measurement range compatible with the expected pressure differentials was selected the MPX5004DP which have a range of 0 to 3.92 kPa.

Based on the CFD results, the expected pressure differential varies significantly depending on engine operating conditions... Based on the CFD results, the expected pressure differential varies significantly depending on engine operating conditions. For high flow rates, pressure differences in the order of several kilopascals were observed, while for low flow conditions, the pressure differential decreases to values close to the resolution limit of standard sensors.

This wide operating range represents a key challenge in sensor selection. A compromise must be made between sensitivity at low pressures and the ability to measure higher pressure differentials without saturation.

For this reason, the selected sensor must provide:

- sufficient resolution to detect low pressure differences;
- an adequate measurement range to cover high flow conditions;
- fast response time to capture transient behaviour.

Despite these considerations, the results obtained from the CFD analysis indicate that the selected Venturi geometry does not generate sufficient pressure differential at very low flow rates, which limits the effectiveness of the measurement system under these conditions. This limitation is inherent to the chosen measurement principle rather than the sensor itself.

Temperature Sensor

The temperature sensor is used to determine the exhaust gas temperature upstream of the Venturi, which is required for the calculation of fluid density.

The CFD analysis showed that the temperature distribution within the Venturi does not exceed critical limits for sensor operation, confirming that the selected sensor can operate safely under the expected conditions.

A Type K thermocouple was used due to its robustness, fast response time, and ability to withstand high temperatures typical of exhaust gases. The selected sensor operates within a temperature range of approximately -200 °C to 800 °C, ensuring compatibility with the expected operating conditions.

NOx Sensor

The NOx sensor is used to measure nitrogen oxides concentration in the exhaust gases, providing key information for emissions analysis.

As described in Section 3.2.1, the selected module is capable of measuring NOx concentration, O_2 levels, and lambda, enabling a more comprehensive analysis of combustion and aftertreatment performance.

However, it is important to consider that the sensor presents cross-sensitivity to NH_3, which may affect measurement accuracy in systems equipped with SCR. This limitation must be considered during data interpretation, particularly under conditions where NH_3 slip may occur.

Sensor Integration Considerations

The integration of the selected sensors within the system requires careful consideration of mechanical, thermal, and electrical aspects. Sensors must be positioned to ensure representative measurements while avoiding excessive exposure to temperature gradients, vibration, and flow disturbances.

Additionally, signal conditioning and proper calibration are essential to ensure measurement accuracy. The combination of differential pressure, temperature, and NOx measurements allows a comprehensive characterisation of the exhaust gas flow and composition, supporting the objectives of the developed system.

3.2.5 Controller Area Network

The CAN protocol was adopted as the main communication interface within the developed system. This choice was motivated by its robustness, reliability, and widespread use in automotive applications, making it particularly suitable for operation in electrically noisy environments such as vehicle exhaust systems.

CAN communication enables efficient and deterministic data exchange between distributed electronic modules without requiring a central master device. Its built-in error detection mechanisms, message prioritisation, and fault tolerance ensure reliable operation even under adverse conditions.

In the proposed system, two independent CAN networks were implemented. The first network is dedicated to communication with the ECM measurement modules, allowing the acquisition of NOx, O_2, and lambda data. The second network is used for communication with external devices, such as dataloggers or laboratory test benches. This separation improves system reliability and prevents interference between internal data acquisition and external communication.

The CAN controllers are interfaced with the microcontroller via the SPI, using dedicated transceiver modules. This configuration provides flexibility in system integration while maintaining compatibility with standard automotive communication protocols.

The use of CAN also facilitates system scalability, allowing additional modules or sensors to be integrated without significant modifications to the existing architecture. Furthermore, it enables synchronised data acquisition across different subsystems, which is particularly important when analysing transient engine behaviour.

Communication with the modules

The communication between the measurement modules and the data acquisition system is performed using the CAN protocol, operating at a bitrate of 500 kbps. This communication speed provides a suitable balance between data throughput and reliability, ensuring stable operation under automotive conditions.

Standard CAN frames (11-bit identifiers) are used for data transmission. Each module transmits multiple messages identified by base IDs (e.g., 0x180, 0x280, 0x380, 0x480) combined with a node identifier (NID), allowing multiple modules to coexist on the same network without address conflicts.

Each CAN frame contains up to 8 bytes of data, structured according to the parameters provided by the module. For example, the frame with ID 0x180 + NID includes Nox concentration and O_2 percentage, while additional frames provide diagnostic and electrical parameters such as current, voltage, and internal sensor signals Table 4.

Data acquisition is performed at a frequency of 10 Hz, which is sufficient to capture transient variations in exhaust gas composition while maintaining low network load. This sampling rate ensures that relevant emission dynamics are captured without introducing unnecessary communication overhead.

The selected communication configuration ensures low latency and reliable data transmission, allowing synchronised acquisition of multiple parameters. This is particularly important for correlating emissions data with engine operating conditions, especially under transient regimes.

Table 4 - Mapping of CAN Frames and Data Bytes for NOx Sensor Communication

TPD01 CAN id	Byte 0	Byte 1	Byte 2	Byte 3	Byte 4	Byte 5	Byte 6	Byte 7
0x180 + NID	NOx(ppm)				O2 (%)			
TPD01 CAN id	Byte 0	Byte 1	Byte 2	Byte 3	Byte 4	Byte 5	Byte 6	Byte 7
0x280 + NID	IP2 (A) disabled				IP1 (A) disabled			
TPD01 CAN id	Byte 0	Byte 1	Byte 2	Byte 3	Byte 4	Byte 5	Byte 6	Byte 7
0x380 + NID	RPVS (Ohms) disable				VHCM(V) disable			
TPD01 CAN id	Byte 0	Byte 1	Byte 2	Byte 3	Byte 4	Byte 5	Byte 6	Byte 7
0x480 + NID	VS (V) disable				VP2 (V) disable			

Communication with the datalogger

The functionality for data transmission to an external datalogger was implemented and validated at the communication system level. Although direct testing with the final datalogger was not performed, the integrity and reliability of the transmission were verified through communication with a secondary microcontroller.

In this context, CAN messages containing the variables processed by the system were transmitted, and the receiving microcontroller successfully validated the message structure, identifiers, and data content. This procedure confirmed the correct operation of the communication chain, including message formatting, signal encoding, and transmission over the CAN bus.

Therefore, the data writing functionality to the datalogger can be considered functionally validated, and its correct operation is expected when integrated with the final system, provided that the same communication conditions are maintained.

3.2.6 Printed Circuit Board

A dedicated PCB was developed to integrate the different components of the measurement system, including sensor interfaces, communication modules, and power management circuitry. The PCB serves as the central hardware platform, ensuring reliable electrical connections and compact system integration.

The design was developed using KiCad, allowing the implementation of a custom layout tailored to the specific requirements of the system. The PCB includes interfaces for the microcontroller, CAN communication modules, sensor inputs, and power supply connections.

Particular attention was given to power distribution and signal integrity. The system operates from a 12 V supply, requiring appropriate voltage regulation to provide stable operating conditions for the microcontroller and peripheral devices. Decoupling capacitors were placed close to critical components to minimise voltage fluctuations and electrical noise.

Given the presence of communication signals and low-level sensor measurements, the PCB layout was designed to reduce electromagnetic interference (EMI). Signal routing was carefully organised to avoid coupling between power and communication lines, and ground planes were implemented to improve noise immunity and overall system stability.

The CAN communication lines were routed following differential signal design principles, ensuring proper impedance and reducing susceptibility to external noise. This is particularly important in automotive environments, where electrical disturbances are common.

All components were assembled manually after fabrication, allowing flexibility during prototyping and testing phases. The PCB was manufactured by JLCPCB, providing a cost-effective solution with adequate quality for the intended application. As shown in Figure 26.

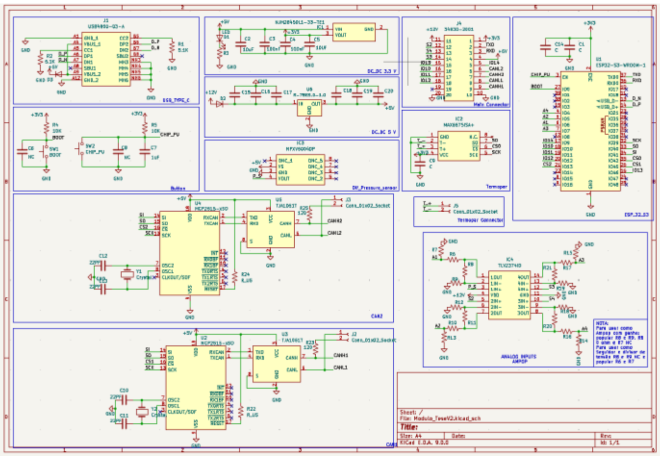

Figure 26 - PCB main Schematic

Since the system is powered by a 12 V DC supply, either from the vehicle battery or an external source, it is necessary to regulate this voltage down to 5 V, as some components operate at this level.

For this purpose, the R-78E5.0-1.0 regulator was used, capable of supplying up to 1 A. To protect the circuit, a diode was added at the input, and to filter and stabilise both the input and output voltages, six capacitors were used, three on each side. As shown in Figure 27.

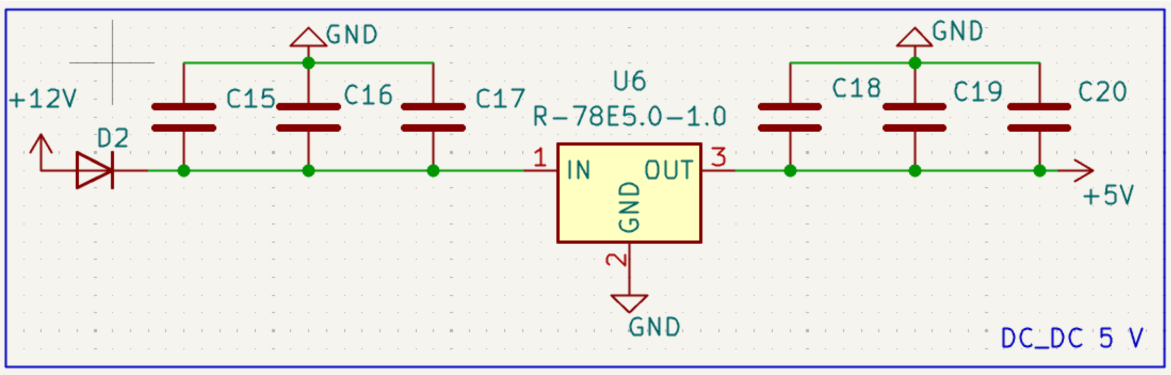

Figure 27 - 5V DCDC schematic converter

Since the ESP32 requires a 3.3 V supply, as well as the Boot and Reset buttons, an additional voltage regulator was required to step down the voltage from 5 V to 3.3 V. The principle is similar to the previous stage, using four capacitors, two at the input and two at the output—as well as an LED for debugging purposes to indicate when the circuit is powered at 5 V.

The voltage regulator used was the NJM2845DL1-33-TE1. As shown in Figure 28.

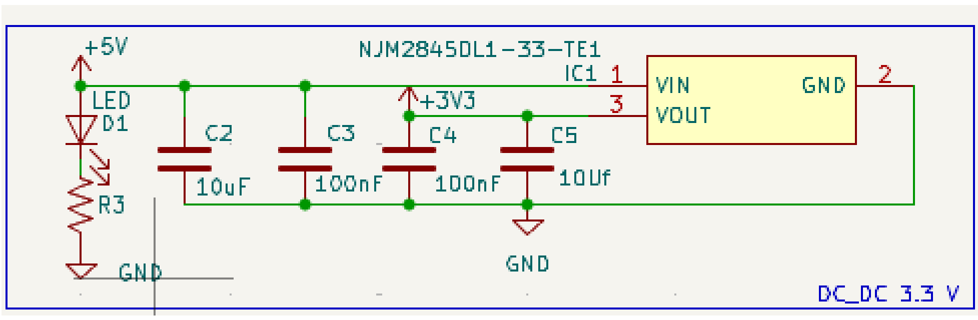

Figure 28 - 3v3 DCDC schematic converter

For the two CAN lines, the MCP2515 module was used, which together with a CAN transceiver, the TJA1051T, and a 16 MHz crystal, is responsible for acquiring CAN messages and transmitting them to the ESP32 via SPI. The circuit also includes a jumper with a 120-ohm resistor across the terminals, allowing the use of CAN termination resistance when required.

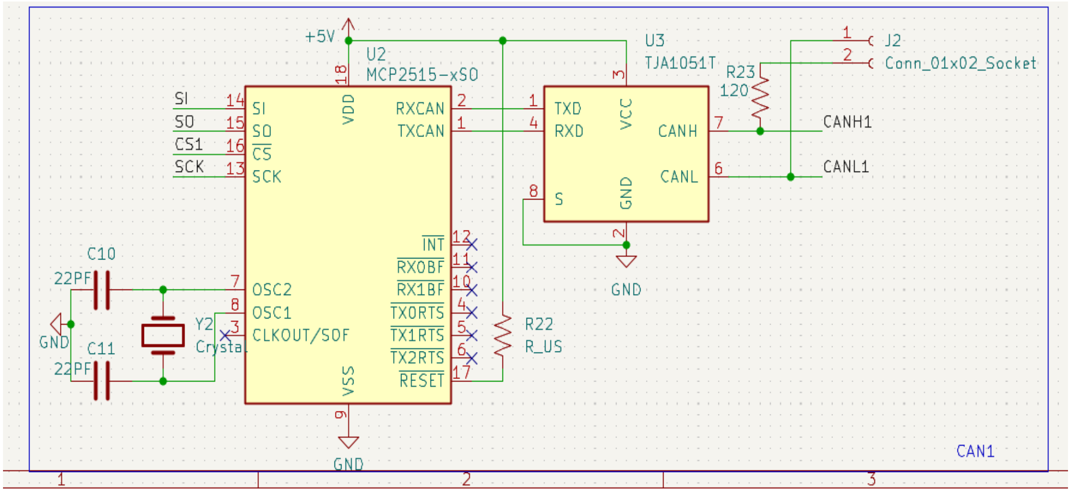

figure 29 - MCP2515 schematic

In order to enable code upload, debugging, and variable storage, a USB Type-C port was used. It includes two communication lines directly connected to the ESP32 (Data+ and Data−), as well as power lines. To protect the computer, a diode was added to prevent reverse voltage. The component reference is USB4800-03-A. As shown in Figure 30.

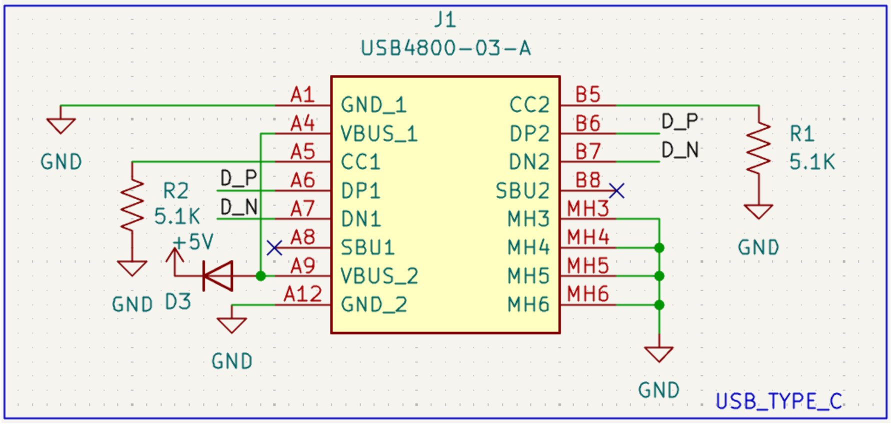

Figure 30 - USB-C schematic

To enable the measurement of the high temperatures of the exhaust gases, a Type K thermocouple was used. For temperature conversion, the MAX6675ISA+ module was employed, along with a connector to interface with the sensor. As shown in Figure 31.

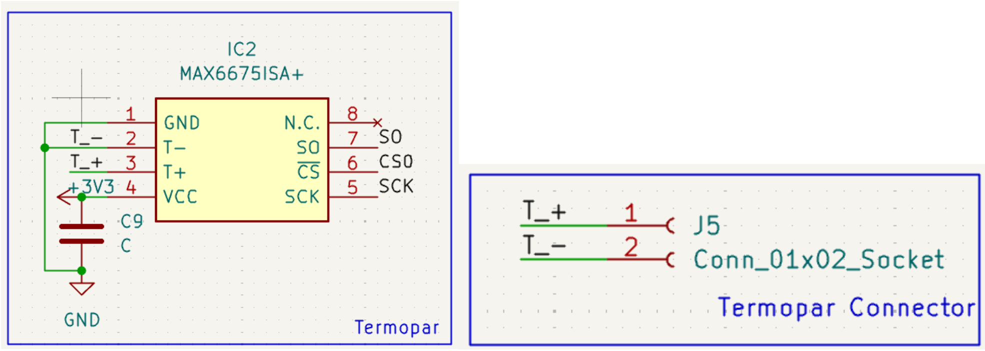

Figure 31 - Thermocouple schematic

The differential pressure sensor used was the MPXV5004DP. It is powered at 5 V and provides an analog output ranging from 1 to 5 V, with an original linear transfer function of 1 V per kPa. As shown in Figure 32.

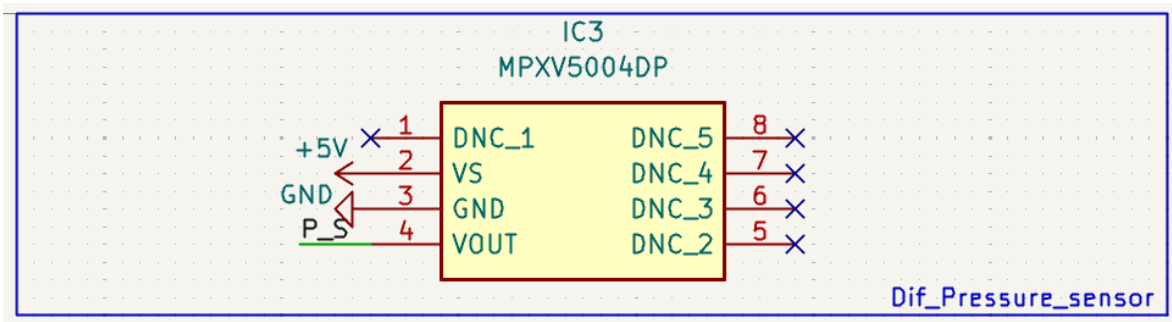

Figure 32 - Differential pressure sensor schematic

To condition the analog signals to a 0 to 3.3 V range, four operational amplifiers were used, designed both to attenuate and to amplify signals.

To use the op-amp with gain, for example, R8 and R9 are populated, R6 is a 0-ohm resistor, and R7 is not populated.

To use it as a voltage follower or voltage divider, R8 and R9 are not populated (NC), while R6 and R7 are populated. As shown in Figure 33.

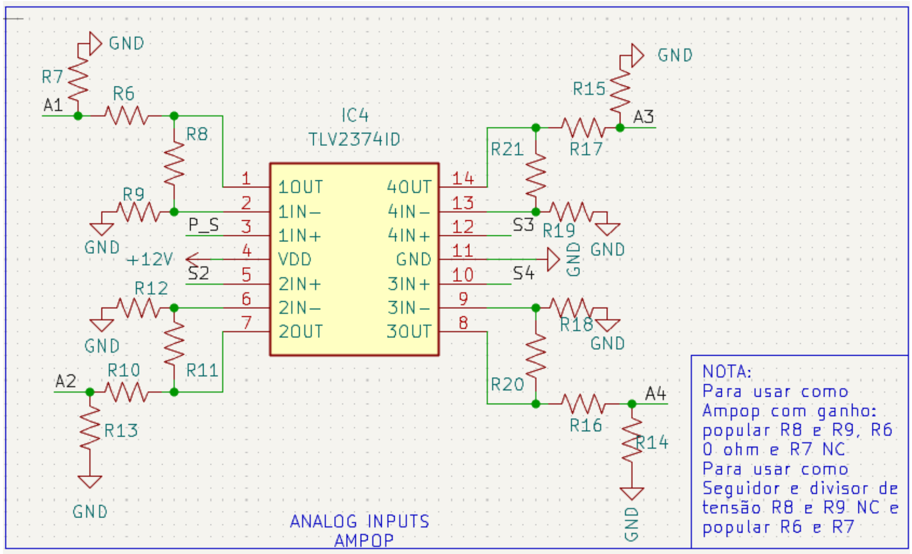

Figure 33 - Op-amp schematic

In the case of the pressure sensor, the signal ranges from 0 to 5 V, so it must be conditioned to 0 to 3 V. For this purpose, R8 and R9 are left open (not populated). To calculate the values of resistors R7 and R6, the following equation is used.

$$R7 = A1 \times \frac{R6}{5 - A1} \tag{9}$$

$$R7 = 3 \times \frac{1000}{5 - 3}$$

$$R7 = 1500\ \Omega$$

In this way, the linear function is transformed from 0–5 V to 0–3 V, as shown in Figure 34.

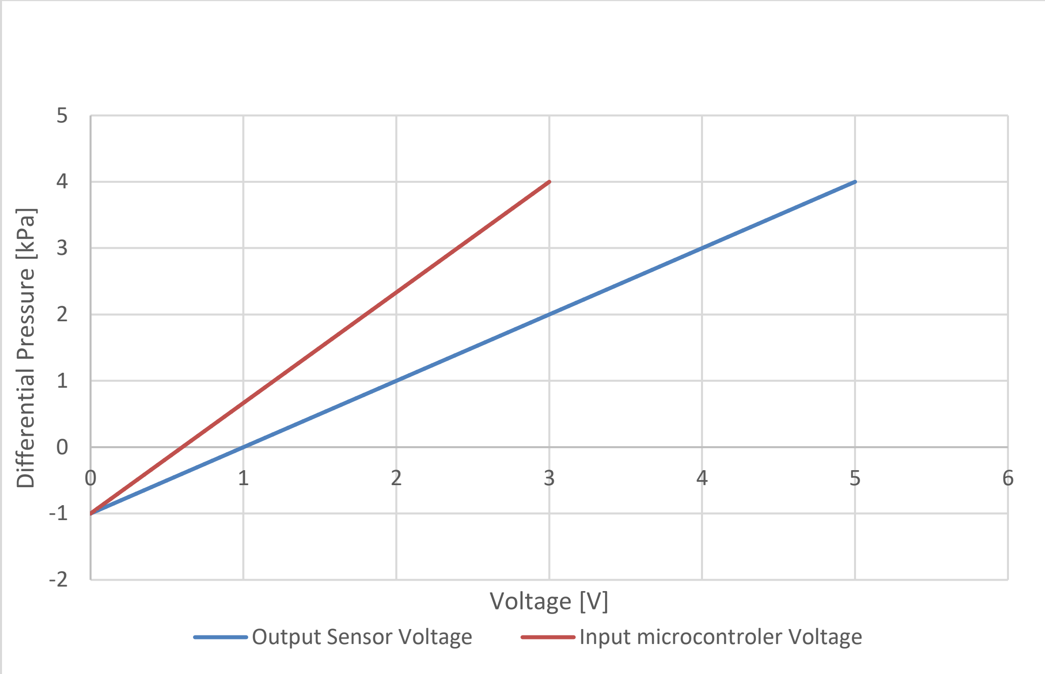

Figure 34 - Difference between DP sensor output tension and microcontroller acquisition tension

For the electrical interface of the board, a 20-pin connector was used to meet all the system's power and signal requirements.

Pin 1 corresponded to a 3.3 V line, intended exclusively to supply the microcontroller section. However, when the system was powered with a higher voltage, this pin operated as a 3 V output.

Pin 4 had a similar function to pin 1. When the board was powered at 12 V, this pin operated as a 5 V output, and could also be used as an input to supply sections of the circuit operating at 5 V and 3.3 V.

Regarding the main power supply, pin 11 was used as the 12 V input, responsible for powering the entire board. This pin functioned exclusively as a power input.

Pins 10 and 20 were used as ground pins. One corresponded to the ground from the power supply, while the other was assigned as an auxiliary ground, allowing it to be used as a common reference for external sensors or for connecting other boards requiring a shared ground.

Pins 12, 13, and 14 were used for digital or analog signals, being directly connected to the section of the schematic corresponding to the operational amplifier. These pins were intended for signals requiring amplification, with gains greater than, less than, or equal to 1, allowing adjustment of the signal amplitude from values close to 0 V up to the operational amplifier supply voltage.

Pins 5, 15, 16, 17, and 18 were directly connected to the microcontroller, allowing their use for different functions, provided that the applied voltage did not exceed 3.3 V.

Finally, pins 5, 6, 7, and 8 were assigned to the CAN lines. One CAN bus was used for communication with the modules, while the other was used for communication with the test bench and the datalogger.

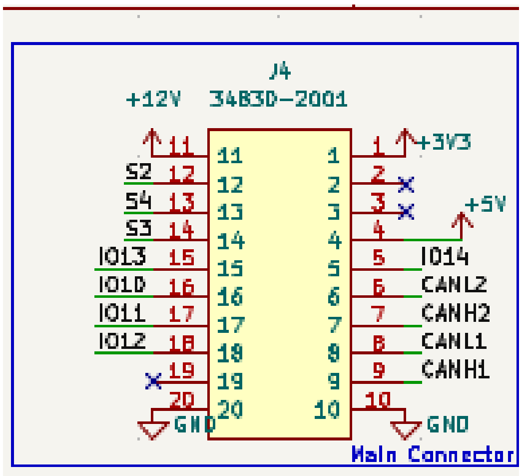

Figure - 35 Main connector schematic

Through datasheet analysis, it was determined that the maximum current supplied by the 3.3 V regulator was 0.5 A, while the maximum current effectively calculated for this supply was 0.2 A. For the 5 V supply, the regulator could deliver up to 1 A, with the maximum current calculated for the circuit being 0.5 A.

For the PCB trace and via sizing, the maximum current values allowed by the regulators were considered in order to ensure an adequate safety margin, minimise trace heating, and guarantee the electrical integrity of the board under more demanding operating conditions.

To calculate the trace widths, the PCB design software itself was used. For this purpose, it was also necessary to define the maximum allowable temperature rise due to the Joule effect. This parameter was adjusted throughout the board development; however, for the initial sizing, a value of 10 °C was considered.

Based on this criterion, 0.4 mm wide traces were used for the 3.3 V supply lines, while traces intended for microcontroller signals had a width of 0.2 mm. For the 5 V and 12 V lines, traces with a width of 0.6 mm were used, ensuring an adequate safety margin for both current handling and thermal performance. As shown in Figure 36.

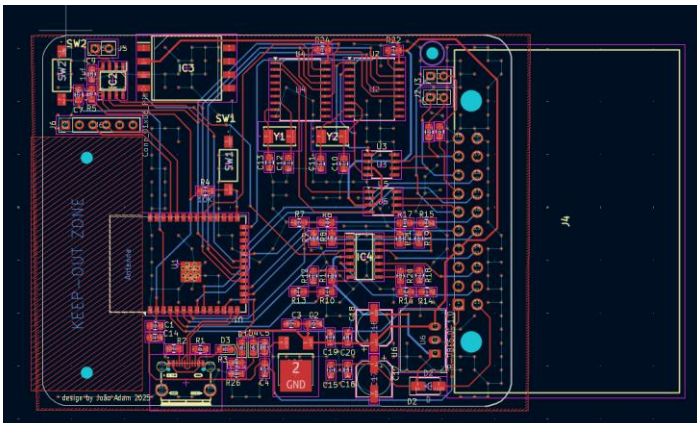

Figure 36 - main PCB

With all parameters properly configured, the components were positioned to optimise space and routing, with the sensors placed along one edge of the board, as shown in Figure 37.

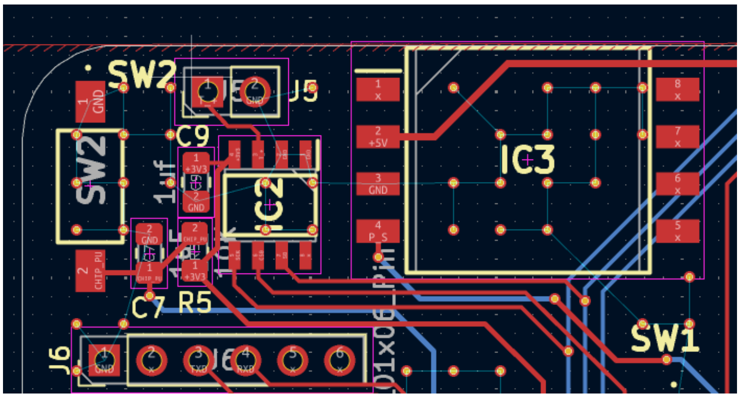

Figure 37 - Sensor PCB layout

In the central area of the board, the operational amplifier was positioned between the microcontroller and the connector, enabling a direct, low-impedance connection to the analog signals. As shown in Figure 38.

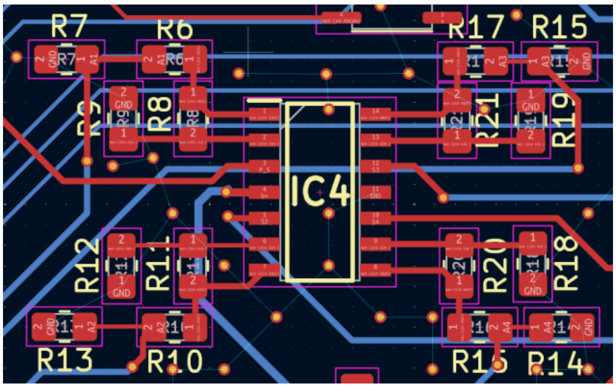

Figure 38 - Op-amp PCB layout

The CAN section was positioned as close as possible to the connector in order to reduce trace length and minimise electromagnetic interference and signal losses. As shown in Figure 39.

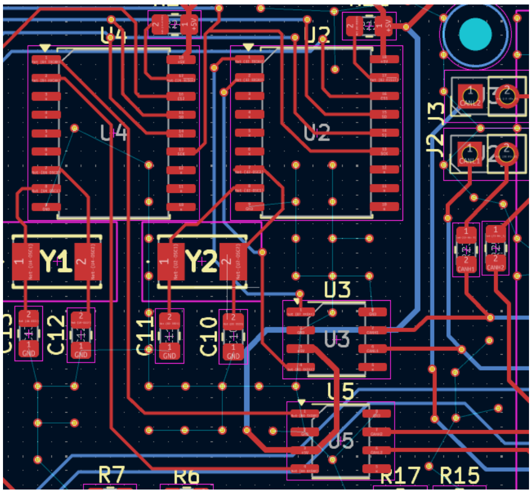

Figure 39 - Can moudles PCB layout

The microcontroller was placed in a position that facilitated its connection to all subsystems, simplifying the trace routing process. As shown in Figure 40.

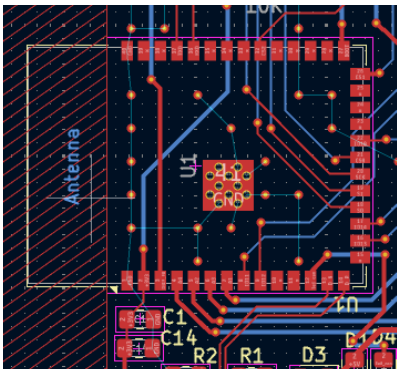

Figure 40 - Esp32 s3 PCB layout

The USB-C port was positioned at one corner of the board to avoid obstructions and allow easy cable connection. As shown in Figure 41.

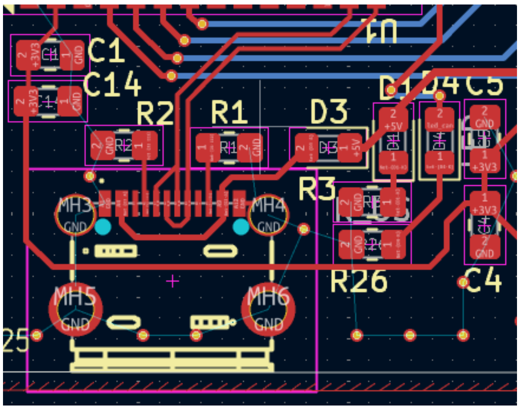

Figure 41 - USB-C PCB layout

The power supply section was placed near the connector, ensuring that the 12 V trace was as short as possible, thereby reducing voltage drops and thermal losses. As shown in Figure 42.

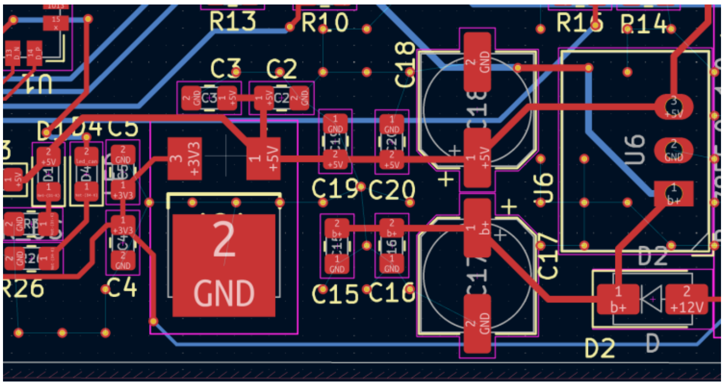

Figure 42 - Power Supply PCB layout

To ensure a solid ground reference, ground planes and via stitching techniques were used to reduce plane impedance, improve current return paths, and minimise electromagnetic interference on the board. As shown in Figure 43.

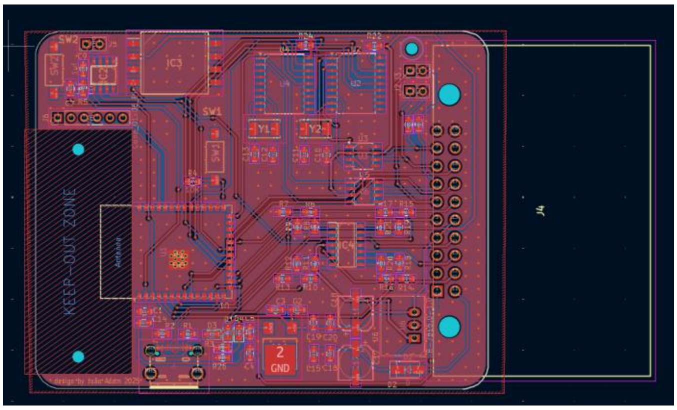

Figure 43 - Ground plane PCB layout

Thus, the final board layout was obtained. As shown in Figure 44.

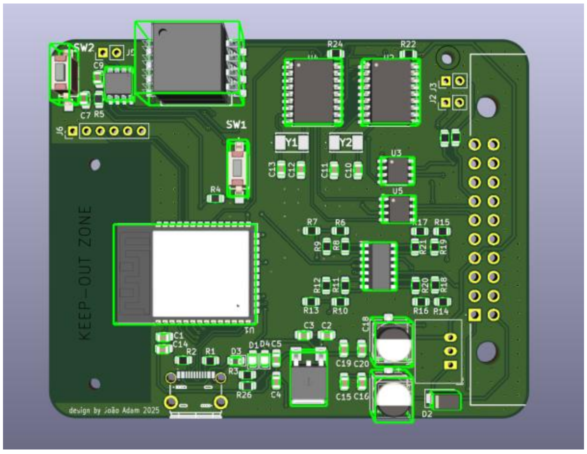

Figure 44 - Final PCB

3.2.7 Power Supply

The power supply was responsible for providing energy to all electronic components of the PEMS. The parameter used for selecting the power adapter was the AC/DC converter power. To calculate the required power supply, the following expression was used:

$$Power = Voltage\,[V] \times Total\ Current\,[A] \tag{10}$$

Since the modules and the PCB had to be powered at 12 V, it was necessary to determine the total current consumption in order to define a suitable power supply that would ensure proper operation of the entire system.

For this purpose, it was necessary to know the current consumption of all electronic equipment in the module. The PCB current consumption was measured experimentally in chapter 4.2 , resulting in a value of 0.044 A.

Regarding the modules, two current regimes were considered: peak current, which occurs at module start-up, and operating current. According to the manufacturer, the peak current could reach up to 5 A, corresponding to the sensor warm-up phase, while the operating current, required only to maintain the operating temperature, was specified as 1 A.

Since the system had to operate under all possible conditions, the worst-case consumption scenario was considered. Thus, it was assumed that all ECM modules simultaneously consumed the peak current of 5 A. Under these conditions, the total current was determined using the following expression:

Total Current = PCB Current + Number of Modules × 5 A

Considering the use of a single module, a total current of 5,044 A was obtained.

By substituting this value into the power equation, it was concluded that the power adapter, for system operation with a single module, had to supply at least 60 W.

3.3 Fabrication Process

The mechanical design of the system was developed to ensure structural integrity, protection of electronic components, and ease of installation and transport. The system was conceived as a portable unit, requiring a robust and compact structure capable of supporting both laboratory and field testing conditions.

A support frame was constructed using welded L-shaped brackets, providing a rigid structure to integrate all system components. This approach ensures mechanical stability and resistance to vibrations, which are particularly relevant in automotive environments.

To protect the system, a bent aluminium sheet was used to form an external enclosure. Aluminium was selected due to its favourable properties, including low weight, corrosion resistance, and adequate thermal behaviour. This enclosure provides mechanical protection while allowing heat dissipation from internal components.

A handle was integrated into the structure to facilitate transport, and support feet were added to ensure stability when the system is placed on the ground. These elements improve usability and enable safe operation in different testing environments. As shown in Figure 45.

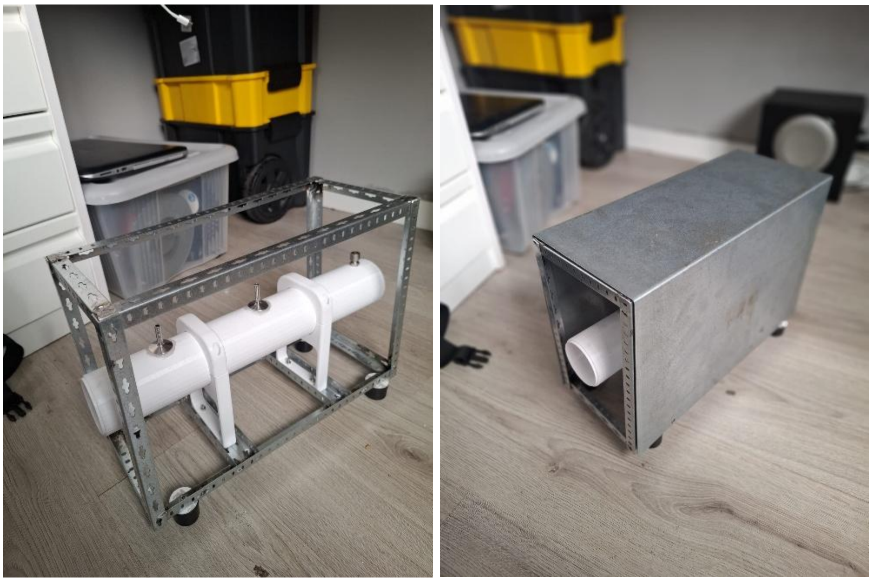

Figure 45 - Venturi main cover

Additionally, a dedicated enclosure for the electronic components was designed using CAD and manufactured using Polyethylene terephthalate glycol (PETG) material. This enclosure ensures protection against environmental factors such as dust and moisture, while benefiting from the higher deformation temperature of PETG compared to other common 3D printing materials. As shown in Figure 46.

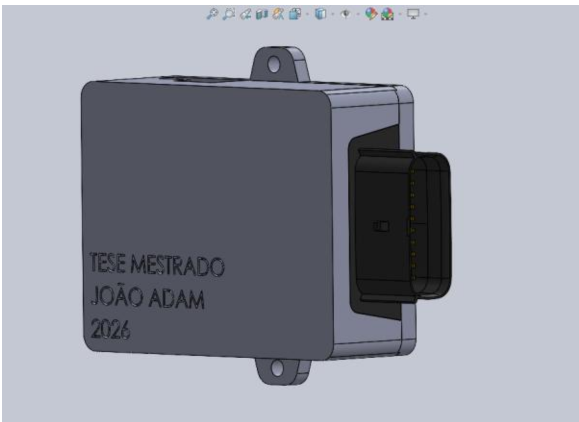

Figure 46 - PCB enclosure

The Venturi component was also manufactured as part of the mechanical system, using stainless steel (SUS304) to withstand high temperatures and corrosive exhaust gases. Due to manufacturing size limitations, the Venturi was divided into multiple sections and subsequently assembled by welding, including the integration of pressure tapping points and V-band connections for installation in the exhaust line. As shown in Figure 47.

Figure 47 - Venturi Tube in Inox

3.4 Firmware development

communication management, and data transmission. Since the system integrates multiple subsystems operating with different update requirements, the firmware was developed using a task-based architecture supported by FreeRTOS.

This approach allows the separation of the main system functions into independent tasks, improving code organisation, maintainability, and timing control. In addition, it enables different execution rates to be assigned according to the dynamic behaviour of each variable and the communication requirements of the system.

The embedded software was implemented in C++ using the Arduino framework for the ESP32-S3 platform. Communication with the CAN controllers and the thermocouple interface is performed through SPI, while sensor data are acquired, processed, and made available for both debugging and external transmission.

3.4.1 Software architecture of the embedded system

The software architecture was organised into independent functional tasks, each responsible for a specific subsystem of the measurement unit. This modular structure allows the separation of acquisition, processing, communication, and diagnostic functions, simplifying debugging and improving system scalability.

The implemented tasks include:

- acquisition of the exhaust gas temperature through the MAX6675 interface;
- acquisition of the differential pressure sensor through the ADC;
- flow rate calculation based on Venturi equations;
- reception of NOx and O_2 data from the ECM module through CAN;
- transmission of processed variables to an external CAN network;
- serial output for system monitoring and debugging.

To ensure safe access to shared resources, FreeRTOS mutexes were used. In particular, a dedicated mutex was implemented for the SPI bus, since both CAN controllers and the thermocouple interface share the same communication bus. A second mutex was used to protect the shared system status structure, preventing concurrent access conflicts between tasks.

The software was also distributed across the two processing cores of the ESP32-S3. Tasks associated with acquisition, processing, and debugging were allocated to one core, while CAN reception and transmission tasks were allocated to the other core. This distribution reduces interference between time-critical communication functions and lower-priority monitoring routines. As shown in Figure 48.

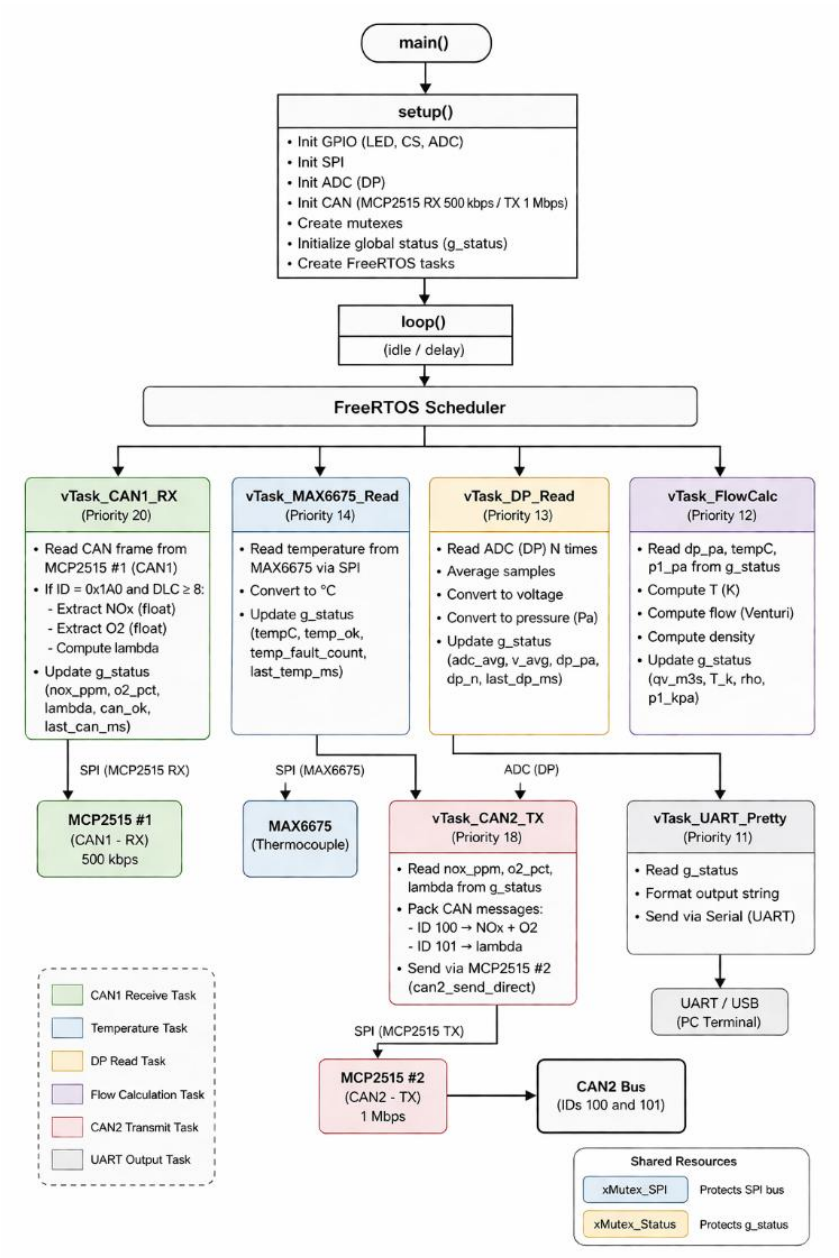

Figure 48 - System functional flow diagram (generated by AI)

3.4.2 Functional flow of the system

At startup, the microcontroller initializes the serial interface, configures the digital and analog pins, starts the SPI bus, configures the CAN controllers, and creates the synchronization objects required by FreeRTOS. After the initialization stage, the system creates the different software tasks responsible for acquisition, processing, communication, and monitoring.

During operation, the temperature task periodically reads the thermocouple signal through the MAX6675 interface and updates the shared system status structure. In parallel, the differential pressure task acquires the analog sensor signal, performs averaging over a configurable number of samples, applies the voltage calibration, and converts the measured value into pressure differential.

The flow calculation task uses the latest available pressure and temperature data to estimate the volumetric flow rate through the Venturi. This calculation includes the use of the gas properties and the Venturi geometric parameters defined in the firmware.

At the same time, a dedicated CAN reception task continuously monitors the measurement module network and decodes the NOx and O_2 values received from the ECM module. Based on the O_2 value, the lambda parameter is also calculated.

Finally, a transmission task periodically sends the processed variables to a second CAN network for communication with external devices. In parallel, a serial output task formats and prints the main variables for debugging and monitoring purposes.

3.4.3 Task execution periodicity

The temporal organisation of the firmware is given by the following table:

Different execution periods were assigned to the software tasks according to the required temporal resolution of each subsystem. This approach allows the system to maintain adequate responsiveness for transient measurements while avoiding unnecessary processor load.

The CAN reception task was configured with the highest update rate, executing every 100 ms, in order to minimise latency in the acquisition of data from the ECM module. Since communication with the measurement module is essential for NOx monitoring, this task was assigned a higher priority than the remaining functions.

The temperature acquisition task was configured with a period of 250 ms. This value was considered adequate because exhaust gas temperature does not vary as rapidly as communication signals and because the MAX6675 itself does not require very high read frequency.

The differential pressure acquisition and flow calculation tasks were both configured to operate at 10 Hz. This update rate was selected as a compromise between temporal resolution and processing cost, while remaining sufficient for the intended flow estimation under transient operating conditions.

The CAN transmission task was configured at 5 Hz, which is adequate for communicating processed variables to external systems without overloading the transmission network. Finally, the UART monitoring task was configured with a period of 100 ms, providing sufficiently frequent updates for debugging without introducing excessive serial communication overhead.

This organisation ensures that faster-varying variables, such as communication data, are handled with higher temporal resolution, while slower variables and diagnostic outputs are processed at lower rates. As presented in Table 5.

Table 5 - Task Periodicity

TASK	FUNCTION	PERIODICITY
VTASK_CAN1_RX	Receive messages CAN1	100 ms
VTASK_DP_READ	Differential Pressure Acquisition	100 ms
VTASK_FLOWCALC	Flow Calc	100 ms
VTASK_UART_PRETTY	Show data in Serial Port	100 ms
VTASK_MAX6675_READ	Temperature Reading	250 ms
VTASK_CAN2_TX	CAN 2 Periodical transmission	200 ms

3.4.4 Main functional blocks description with code excerpts

3.4.4.1 System global state structure

The status_t structure consolidates the main system variables into a single memory block shared between tasks. It stores:

- the latest sensor readings;
- calculated values;
- data received via CAN;
- validity indicators;
- update timestamps.

This approach enables a clear separation between data acquisition and processing from data presentation or retransmission. Instead of each task maintaining its own set of independent variables, the system operates on a consolidated global state, simplifying both the architecture and its functional description. As shown in Figure 49.

```
typedef struct {
  // timestamps
  uint32_t now_ms;
  uint32_t last_dp_ms;
  uint32_t last_temp_ms;
  uint32_t last_can_ms;

  // DP
  uint32_t adc_avg;
  float    v_avg;
  int32_t  dp_pa;
  uint16_t dp_n;

  // Temperatura
  float    tempC;
  bool     temp_ok;
  uint32_t temp_fault_count;

  // Caudal
  float    qv_m3s;
  float    rho;
  float    T_k;
  float    p1_kpa;

  // CAN (últimos valores)
  float    nox_ppm;
  float    o2_pct;
  float    lambda;
  bool     can_ok;
} status_t;

static status_t g_status{};
```

Figure 49 – Struct code

3.4.4.2 Direct CAN transmission function.

The function can2_send_direct() directly prepares a can_frame structure, copies the data to be transmitted, sets the CAN identifier, and performs the transmission through the MCP2515 associated with the second CAN network.

Access to the SPI bus remains protected by xMutex_SPI, as the same bus is shared by the CAN transmitter, the CAN receiver, and the MAX6675.

This block represents the layer closest to the physical transmission on CAN2. Its function is purely operational: to take the bytes to be sent and place them onto the bus. As shown in Figure 50.

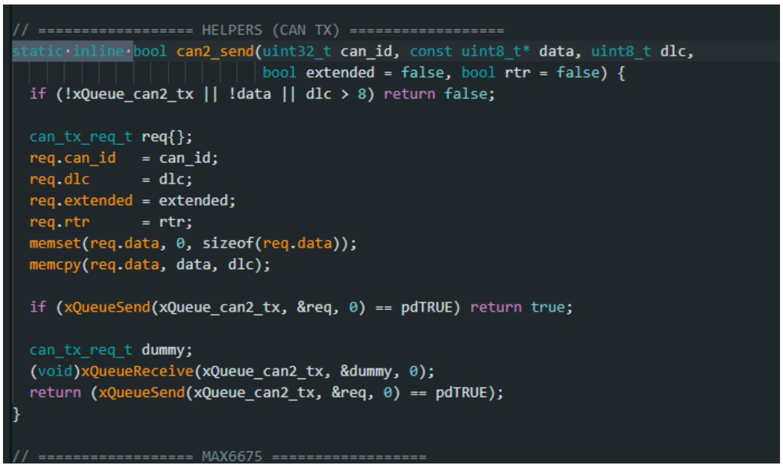

```
// ================= HELPERS (CAN TX) =================
static inline bool can2_send(uint32_t can_id, const uint8_t* data, uint8_t dlc,
                             bool extended = false, bool rtr = false) {
  if (!xQueue_can2_tx || !data || dlc > 8) return false;

  can_tx_req_t req{};
  req.can_id   = can_id;
  req.dlc      = dlc;
  req.extended = extended;
  req.rtr      = rtr;
  memset(req.data, 0, sizeof(req.data));
  memcpy(req.data, data, dlc);

  if (xQueueSend(xQueue_can2_tx, &req, 0) == pdTRUE) return true;

  can_tx_req_t dummy;
  (void)xQueueReceive(xQueue_can2_tx, &dummy, 0);
  return (xQueueSend(xQueue_can2_tx, &req, 0) == pdTRUE);
}

// ================= MAX6675 =================
```

Figure 50 - Can2 Send code

3.4.4.3 Temperature data acquisition.

This function implements temperature acquisition using the MAX6675 converter. The device is accessed via SPI, so the transaction is executed within a section protected by the bus mutex.

- After reading the 16 bits from the output register:
- the device fault bit is checked;
- if the reading is valid, the useful value is extracted;
- the value is converted to degrees Celsius according to the sensor resolution.

The function returns a logical success or failure status, allowing the calling task to register the validity of the measurement. As shown in Figure 51.

```
// ================== MAX6675 ===================
static bool max6675_read_celsius(float &tempC) {
  uint16_t raw = 0;

  xSemaphoreTake(xMutex_SPI, portMAX_DELAY);
  SPI_MCP.beginTransaction(spiSettingsMAX6675);
  digitalWrite(PIN_SPI_CS_MAX6675, LOW);
  raw = SPI_MCP.transfer16(0x0000);
  digitalWrite(PIN_SPI_CS_MAX6675, HIGH);
  SPI_MCP.endTransaction();
  xSemaphoreGive(xMutex_SPI);

  if (raw & 0x0004) return false;

  uint16_t t = (raw >> 3) & 0x0FFF;
  tempC = (float)t * 0.25f;
  return true;
}
```

Figure 51 - Low-level MAX6675 temperature reading function

3.4.4.4 Temperature acquisition task.

The task vTask_MAX6675_Read periodically performs temperature acquisition with a fixed period of 250 ms. At each activation:

- it calls the MAX6675 reading function;
- updates the temperature value in the global structure;
- records whether the reading was valid;
- updates the timestamp of the last valid measurement;
- increments the fault counter when applicable.

This task is exclusively dedicated to the thermal variable, which enhances modularity and simplifies the experimental validation of the temperature measurement chain. As shown in Figure 52.

```
// ================== TASK: MAX6675 ==================
static void vTask_MAX6675_Read(void *pvParameters) {
  (void)pvParameters;
  TickType_t tLast = xTaskGetTickCount();

  for (;;) {
    float tempC = 0.0f;
    bool ok = max6675_read_celsius(tempC);

    xSemaphoreTake(xMutex_Status, portMAX_DELAY);
    if (ok) {
      g_status.tempC = tempC;
      g_status.temp_ok = true;
      g_status.last_temp_ms = millis();
    } else {
      g_status.temp_ok = false;
      g_status.temp_fault_count++;
    }
    xSemaphoreGive(xMutex_Status);

    vTaskDelayUntil(&tLast, pdMS_TO_TICKS(TASK_MAX6675_PERIOD_MS));
  }
}
```

Figure 52 - Periodic MAX6675 temperature acquisition task

3.4.4.5 Differential pressure acquisition.

The task vTask_DP_Read is responsible for the acquisition and initial processing of the differential pressure sensor signal. The execution cycle runs at 10 Hz.

The reading is performed using an average of n ADC samples, where n is adjustable via the dp_filtro variable. This mechanism reduces the influence of noise on the measurement. After digital averaging:

- the ADC value is converted into voltage;
- the voltage is converted into differential pressure through a calibrated linear relationship;
- the results are stored in the global structure.

This block represents the acquisition chain of the pressure variable, from the raw digital domain to the physical value in Pascal. As shown in Figure 53.

```
// ================== TASK: DP ==================
static void vTask_DP_Read(void *pvParameters) {
  (void)pvParameters;

  const TickType_t period = pdMS_TO_TICKS(1000 / DP_TASK_HZ);
  TickType_t tLast = xTaskGetTickCount();

  for (;;) {
    vTaskDelayUntil(&tLast, period);

    int n = dp_filtro;
    if (n < 1) n = 1;
    if (n > 5000) n = 5000;

    uint64_t sum = 0;
    for (int i = 0; i < n; i++) {
      sum += (uint32_t)analogRead(PIN_DP_ADC);
    }

    const uint32_t adc_avg = (uint32_t)(sum / (uint64_t)n);

    // calibração ADC -> V
    const float v_avg = ((float)adc_avg * 0.00077206f) + 0.1f;

    // calibração V -> Pa
    const int32_t dp_pa = (int32_t)lroundf(1757.8475336f * v_avg - 1353.5426009f);

    xSemaphoreTake(xMutex_Status, portMAX_DELAY);
    g_status.adc_avg = adc_avg;
    g_status.v_avg   = v_avg;
    g_status.dp_pa   = dp_pa;
    g_status.dp_n    = (uint16_t)n;
    g_status.last_dp_ms = millis();
    xSemaphoreGive(xMutex_Status);
  }
}
```

Figure 53 - DP read task

3.4.4.6 math functions of Venturi.

These functions implement the mathematical core of the flow rate calculation using the Venturi. The model considers:

- the Venturi geometry, through the β ratio;
- the throat area;
- gas expansibility;
- density obtained from the ideal gas equation.

The flow rate is calculated in SI units and includes numerical robustness checks, such as rejection of invalid inputs and the application of a deadband for very small differential pressures.

This set of functions constitutes the central physical-mathematical block of the firmware, being responsible for transforming primary measurements into the experimental variable of interest. As shown in Figure 54.

```c
// ================== Venturi math (SI) ==================
static inline float venturi_beta() {
  const float D = VENTURI_D_IN_M;
  const float d = VENTURI_D_THROAT_M;
  if (D <= 0.0f) return 0.0f;
  return d / D;
}

static inline float venturi_area_throat() {
  const float d = VENTURI_D_THROAT_M;
  const float r = 0.5f * d;
  return (float)M_PI * r * r;
}

static inline float venturi_eps(float dp_abs_pa, float p1_pa, float gamma, float beta) {
  if (p1_pa <= 0.0f || gamma <= 0.0f) return 1.0f;
  const float beta2 = beta * beta;
  const float beta4 = beta2 * beta2;
  const float beta8 = beta4 * beta4;
  const float k = (0.351f + 0.256f * beta4 + 0.93f * beta8);
  const float x = dp_abs_pa / (gamma * p1_pa);
  float eps = 1.0f - k * x;
  if (eps > 1.0f) eps = 1.0f;
  if (eps < 0.0f) eps = 0.0f;
  return eps;
}
```

```c
static inline float venturi_qv_from_dp_T_p1(int32_t dp_pa, float T_k, float p1_pa) {
  if (T_k <= 0.0f || p1_pa <= 1000.0f) return 0.0f;

  const float rho = p1_pa / (GAS_R_SPEC * T_k);
  if (rho <= 0.0f) return 0.0f;

  const float beta = venturi_beta();
  const float At = venturi_area_throat();
  if (beta <= 0.0f || beta >= 1.0f || At <= 0.0f) return 0.0f;

  const float dp = (float)dp_pa;
  const float dp_abs = fabsf(dp);
  if (dp_abs < DP_DEADBAND_PA) return 0.0f;

  const float eps = venturi_eps(dp_abs, p1_pa, GAS_GAMMA, beta);

  const float beta2 = beta * beta;
  const float beta4 = beta2 * beta2;
  const float denom = sqrtf(fmaxf(1e-12f, (1.0f - beta4)));

  const float K = (VENTURI_C / denom) * At * eps * sqrtf(2.0f * rho);
  const float qm = copysignf(K * sqrtf(dp_abs), dp);
  return qm / rho;
}
```

Figure 54 - Flow math

3.4.4.7 Volumetric flow

The task vTask_FlowCalc periodically computes the volumetric flow rate of the exhaust gases. The calculation cycle runs at 10 Hz.

- At each iteration, the task:
- reads the differential pressure;
- reads the temperature;
- considers the upstream absolute pressure;
- converts the temperature to Kelvin;
- calculates the gas density;
- computes the flow rate using the Venturi model;
- stores the results in the global state.

This separation between acquisition and calculation is appropriate from a design perspective, as it allows the physical algorithm to be isolated from the sensor reading implementation details. As shown in Figure 55.

```
// ================= TASK: FLOW =================
static void vTask_FlowCalc(void *pvParameters) {
  (void)pvParameters;

  const TickType_t period = pdMS_TO_TICKS(1000 / FLOW_TASK_HZ);
  TickType_t tLast = xTaskGetTickCount();

  for (;;) {
    vTaskDelayUntil(&tLast, period);

    int32_t dp_pa;
    float tempC;
    float p1_pa;

    xSemaphoreTake(xMutex_Status, portMAX_DELAY);
    dp_pa  = g_status.dp_pa;
    tempC  = g_status.tempC;
    p1_pa  = (float)g_p1_pa;
    xSemaphoreGive(xMutex_Status);

    const float T_k = tempC + 273.15f;
    const float qv  = venturi_qv_from_dp_T_p1(dp_pa, T_k, p1_pa);
    const float rho = (T_k > 0.0f) ? (p1_pa / (GAS_R_SPEC * T_k)) : 0.0f;

    xSemaphoreTake(xMutex_Status, portMAX_DELAY);
    g_status.qv_m3s = qv;
    g_status.T_k    = T_k;
    g_status.rho    = rho;
    g_status.p1_kpa = p1_pa / 1000.0f;
    xSemaphoreGive(xMutex_Status);
  }
}
```

Figure 55 - Flow calculation

3.4.4.8 Sensors CAN Communication

The task vTask_CAN1_RX is responsible for receiving messages from the first CAN network. Its short period of 2 ms was chosen to ensure fast reading of messages available in the MCP2515.

When a message with the expected identifier is detected: As shown in Figure 56.

- two values in float format, corresponding to NOx and O_2, are extracted;
- the λ value is calculated based on the O_2 concentration;
- all three values are stored in g_status.

```
// ================= TASK: CAN1 RX =================
static void vTask_CAN1_RX(void *pvParameters) {
  (void)pvParameters;
  TickType_t tLast = xTaskGetTickCount();
  struct can_frame rx{};

  for (;;) {
    xSemaphoreTake(xMutex_SPI, portMAX_DELAY);
    MCP2515::ERROR err = mcp2515_rx.readMessage(&rx);
    xSemaphoreGive(xMutex_SPI);

    if (err == MCP2515::ERROR_OK) {
      if (rx.can_id == CAN_ID_SENSOR && rx.can_dlc >= 8) {
        float NOx = 0.0f;
        float O2  = 0.0f;

        memcpy(&NOx, &rx.data[0], sizeof(float));
        memcpy(&O2,  &rx.data[4], sizeof(float));

        const float denom  = (20.9f - O2);
        const float lambda = (fabsf(denom) > 0.001f) ? (20.9f / denom) : 0.0f;

        xSemaphoreTake(xMutex_Status, portMAX_DELAY);
        g_status.nox_ppm     = NOx;
        g_status.o2_pct      = O2;
        g_status.lambda      = lambda;
        g_status.can_ok      = true;
        g_status.last_can_ms = millis();
        xSemaphoreGive(xMutex_Status);
      }
    }

    vTaskDelayUntil(&tLast, pdMS_TO_TICKS(TASK_CAN1_RX_PERIOD_MS));
  }
}
```

Figure 56 - Nox read task

3.4.4.9 Communication with the datalogger

The task vTask_CAN2_TX implements periodic transmission on the second CAN network. This task:

- runs at a fixed frequency defined by CAN2_TX_HZ;
- reads the latest available values from the global state;
- prepares two CAN messages;
- transmits these messages on the CAN2 bus

The first message contains NOx and O_2 values, while the second contains the λ value.

The CAN2 network maintains a constant update rate, regardless of the arrival rate of external data. This can be useful when the receiving system expects regular updates or when deterministic timing behaviour is required at the output.

There is also an important technical consequence: if new data stops arriving via CAN1, the task will continue transmitting the last valid stored values. As shown in Figure 57.

```
// ================= TASK: CAN2 TX PERIÓDICO =================
static void vTask_CAN2_TX(void *pvParameters) {
  (void)pvParameters;

  const TickType_t period = pdMS_TO_TICKS(1000 / CAN2_TX_HZ);
  TickType_t tLast = xTaskGetTickCount();

  for (;;) {
    vTaskDelayUntil(&tLast, period);

    float nox, o2, lambda;

    xSemaphoreTake(xMutex_Status, portMAX_DELAY);
    nox    = g_status.nox_ppm;
    o2     = g_status.o2_pct;
    lambda = g_status.lambda;
    xSemaphoreGive(xMutex_Status);

    // Mensagem 1: ID 100 -> NOx + O2
    uint8_t pA[8] = {0};
    memcpy(&pA[0], &nox, sizeof(float));
    memcpy(&pA[4], &o2,  sizeof(float));
    (void)can2_send_direct(CAN2_ID_NOX_O2, pA, 8, false, false);

    // Mensagem 2: ID 101 -> lambda
    uint8_t pB[8] = {0};
    memcpy(&pB[0], &lambda, sizeof(float));
    (void)can2_send_direct(CAN2_ID_LAMBDA, pB, 8, false, false);
  }
}
```

Figure 57 - Can to datalogger task

3.4.4.10 Serial Print to Diagnostic Task

This task generates the diagnostic textual output via the serial port. Every 100 ms, the contents of the global structure are copied into a local variable and formatted into a single line containing the main system operating parameters.

The information provided includes:

- temperature and its validity status;

- differential pressure, equivalent voltage, and number of averaged samples;
- volumetric flow rate, absolute temperature, density, and pressure;
- received CAN values.

This block does not directly participate in measurement or control, but it is important for experimental validation, bench testing, and fault detection during development. As shown in Figure 58.

```
// ================== TASK: UART ==================
static void vTask_UART_Pretty(void *pvParameters) {
  (void)pvParameters;

  TickType_t tLast = xTaskGetTickCount();
  char line[260];

  for (;;) {
    vTaskDelayUntil(&tLast, pdMS_TO_TICKS(TASK_UART_PERIOD_MS));

    status_t s;
    xSemaphoreTake(xMutex_Status, portMAX_DELAY);
    g_status.now_ms = millis();
    s = g_status;
    xSemaphoreGive(xMutex_Status);

    const bool have_can = s.can_ok;

    snprintf(…
    );

    if (have_can) {…
    }

    Serial.println(line);
  }
}
```

Figure 58 - Uart task

This page was intentionally left blank

4 System Validation

The validation stage was carried out to assess the functionality and performance of the main subsystems developed in this work. Since the proposed system integrates measurement, signal processing, communication, and mechanical components, validation was performed at both component level and system level.

The experimental work focused on three main aspects: verification of the NOx measurement module and its communication capability, validation of the electronic hardware through PCB testing, and validation of the Venturi-based flow measurement approach. These tests were intended to confirm that the developed system operates correctly under the expected conditions and that the selected components are suitable for the intended application.

The validation methodology combined functional verification, experimental measurements, and comparative analysis between measured and expected values. This approach made it possible to identify the operating limits of the system and to assess the reliability of the implemented solution.

4.1 Nitrogen Oxides Module Validation

For the verification and validation of the NOx module operation, an experimental test was carried out consisting of the controlled variation of the lambda value by adjusting the amount of injected fuel, while keeping the engine at idle. This procedure made it possible to analyse the response of the NOx module and assess the consistency of NOx and lambda measurements under different air–fuel mixture conditions.

The test was conducted using a Ford Sierra equipped with a 4-cylinder, 2000 cc engine, with injection controlled by a reprogrammable engine control unit. This unit allowed real-time adjustment of the lambda value by modifying the injected fuel quantity. By maintaining a constant engine speed, these changes directly influenced the lambda value, enabling the definition of different controlled engine operating points.

The comparison of NOx values was performed using an emissions analyser from Testo XL350, allowing the values measured by the NOx module to be compared with those obtained from a certified instrument. Additionally, the lambda value was compared using three distinct sources: a lambda measurement module from AEM, the vehicle's original lambda sensor, and the NOx module itself. This approach enabled validation of the consistency and reliability of lambda measurements provided by the module through comparison with reference equipment and the vehicle's original system.

For the test setup, the vehicle's original exhaust system was used up to the end of the primary pipes, where the original lambda sensor was installed. Downstream of this point, a modified exhaust section was used, in which two threaded bungs were welded to accommodate the sensors from the ECM modules and the AEM system. Additionally, the emissions analyser probe from the Testo system was installed in the same area, as illustrated in Figure 59.

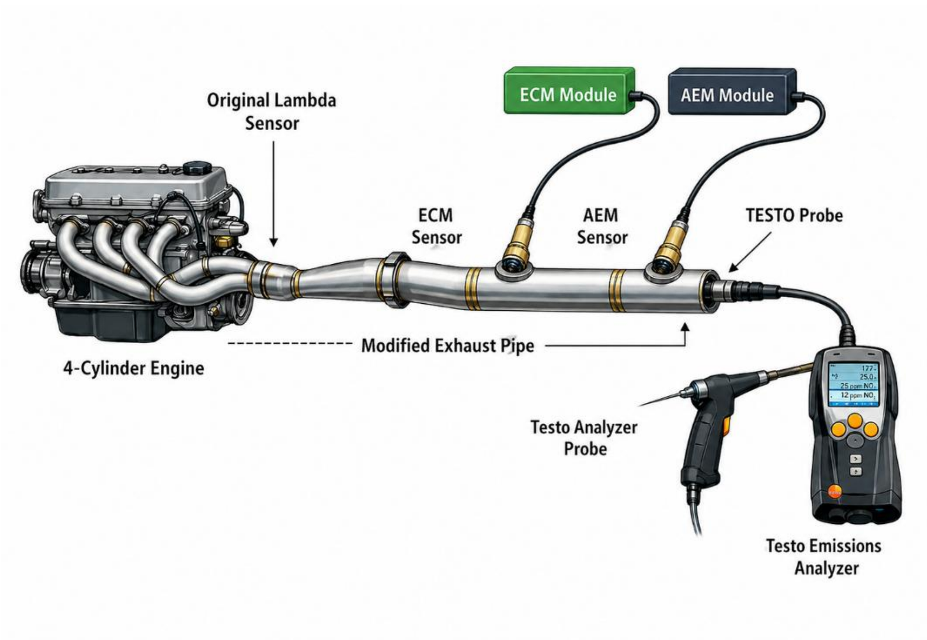

Figure 59 - Schematic of the experimental test of the NOx sensor (Image generated by AI)

The experimental procedure consisted of defining different lambda values by adjusting the amount of fuel injected by the Motec unit. These values, presented in Table 6, were selected to allow the engine to operate across a range of air–fuel mixture conditions, including both rich and lean regimes, while ensuring proper engine operation and including a transition through $\lambda = 1.05$, which theoretically corresponds to the point of maximum NOx formation, as shown in Figure 1.

After each change in lambda value, a stabilisation period of approximately 30 seconds was allowed to ensure steady engine operation and stable sensor readings. Following this stabilisation period, data were acquired over a 20-second interval.

The values presented for each test point correspond to the average of the measurements taken during this 20-second interval for all studied variables, namely NOx and lambda. This procedure reduced the influence of short-term fluctuations and ensured greater reliability and repeatability of the results.

For data acquisition, the software provided by the respective equipment manufacturers was used, except for the lambda measurement module from AEM, whose values were recorded manually in a spreadsheet using Microsoft Excel.

Five distinct operating points were defined and measured, corresponding to five lambda values obtained from the vehicle's original lambda sensor. These values were considered as reference values for the comparative analysis of the remaining measurement systems.

Table 6 - Lambda tests point

Test Conditions- operating points	Lambda probe value [-]
1	0.9
2	0.96
3	1.04
4	1.16
5	1.3

The atmospheric conditions provided by the laboratorial installation are specified in the following table. As presented in Table 7.

Table 7 - Atmospheric Conditions

%O2	Temperature [ºc]	% Humidity R	Press [kPa]
20.58	26.1	51.9	101.64

The first comparison parameter between the modules was the O_2 concentration (%) in the air, as both modules compute it, yielding the following results:

Testo	20.95%
ECM	20.40%

Compared to the ECM module, regarding the O_2 concentration in the air, a difference of 2% was observed relative to the values measured by the Testo analyser, and a difference of 0.9% when compared to the values obtained from the dynamometer test bench.

The second comparison parameter was the lambda value, for which the following results were obtained: As presented in Table 8.

Table 8 - Lambda results

PONTO	LAMBDA PROBE	AEM	ECM	DIF% SL/ECM	DIF% AEM/ECM
1	0.9	0.9	0.87	2.5	2.5
2	0.96	0.97	0.95	0.4	1.5
3	1.04	1.07	1.05	0.9	1.8
4	1.16	1.17	1.15	0.3	1.2
5	1.3	1.31	1.28	1.3	2.1

Regarding the comparison between the original vehicle lambda sensor and the ECM module, a percentage difference of 2.59% was obtained at point 1, 0.49% at point 2, 0.97% at point 3, 0.35% at point 4, and 1.38% at point 5.

With respect to the comparison between the AEM lambda measurement module and the ECM module, a percentage difference of 2.59% was observed at point 1, 1.52% at point 2, 1.86% at point 3, 1.20% at point 4, and 2.14% at point 5. As shown in Figure 60.

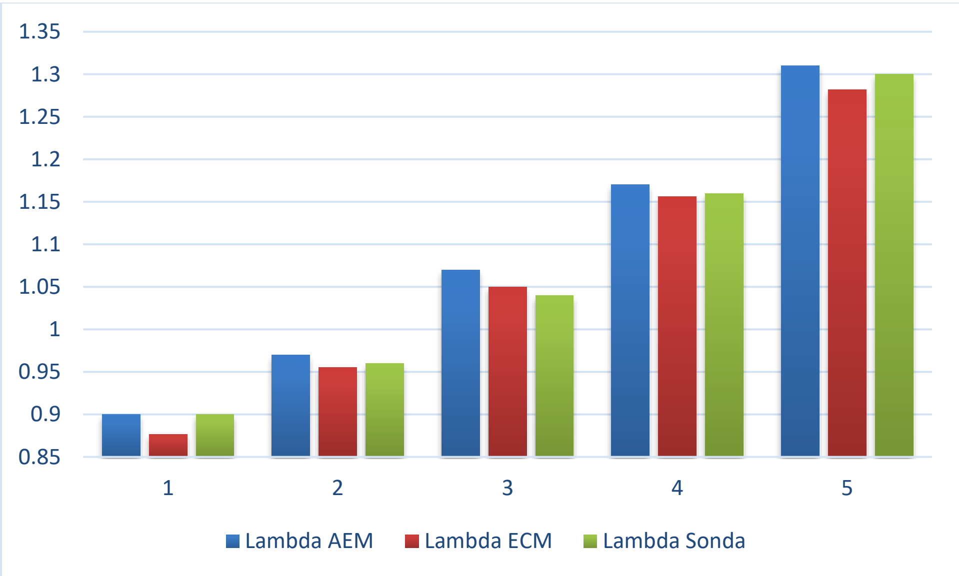

Figure 60 - Lamda values of experimental test

The final parameter analysed was the NOx value, and the results are presented in the following table. As presented in Table 9.

Table 9 - NOx Results

Test Points	Testo, NOx [ppm]	ECM ,NOx [ppm]	dif% Testo/ECM
1	874.3	815.0	7.2
2	1629.7	1636.8	0.4
3	2089.8	1882.6	11.0
4	940.3	817.2	15.0
5	150.4	123.9	21.3

Regarding the comparison of the average NOx values between the Testo analyser and the ECM module, a percentage difference of 7.27% was obtained at point 1, 0.44% at point 2, 11.00% at point 3, 15.06% at point 4, and 21.34% at point 5.

Although the NOx measurements obtained from the ECM module showed minor deviations when compared with the Testo analyser, the overall behaviour of the sensor can be considered consistent and reliable. The results clearly demonstrate that the sensor is capable of accurately capturing the expected trends and dynamic variations of NOx emissions across the tested operating points.

It is important to note that NOx measurements are inherently sensitive to calibration procedures and operating conditions. Therefore, the observed discrepancies cannot be attributed exclusively to the ECM sensor, as they may also arise from uncertainties associated with the reference instrument. Since only a single reference analyser (Testo) was used, a comprehensive assessment of measurement accuracy remains limited.

For this reason, further validation using an independent NOx measurement system is recommended. This would enable cross-verification of the results and support a more rigorous calibration process, ensuring increased confidence in the absolute accuracy of both measurement systems. As shown in Figures 61 and 62.

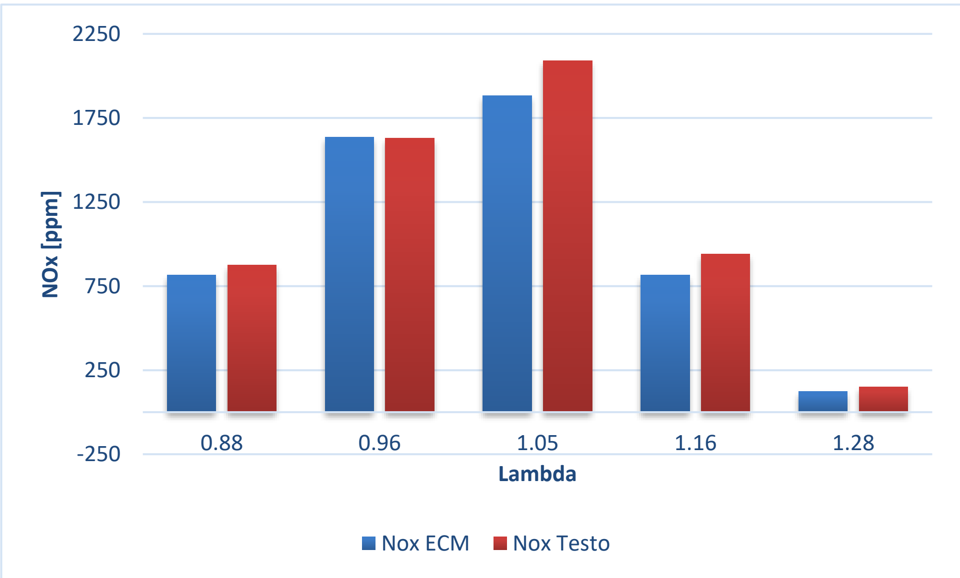

Figure 61 - NOx values as a function of lambda values for the 5 experimental test conditions.

Figure 62 - Exhaust test photo

4.2 Printed Circuit Board Validation.

After soldering the PCB, a validation procedure was carried out in order to verify whether all modules communicated correctly and whether the system met the intended functionality.

In an initial stage, a visual inspection of the solder joints was performed using a microscope to identify possible short circuits between component pins and to confirm the quality of the soldering process. This procedure proved essential, as illustrated in Figure 63, where a short circuit between two pins was detected. This issue was corrected by reworking the soldering, thereby preventing potential damage to the board during power-up.

Figure 63 - microscope PCB validation

After completing this procedure, the board was initially powered through the 12 V supply line. The power LED turned on, and the current drawn from the power supply was 0.044 A, a value consistent with the expected operation in the absence of short circuits. As shown in Figure 64.

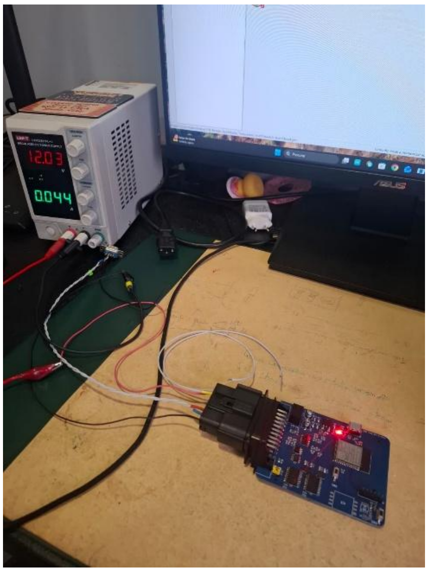

Figure 64 - Power supply test

The correct operation of the DC-DC converters was then verified. For this purpose, the voltage reduction from 12 V to 11.3 V, due to the voltage drop across the protection diode, was confirmed, as well as the subsequent conversion from 11.3 V to 5 V and from 5 V to 3.3 V. As shown in Figures 65, the entire power supply system operated as expected.

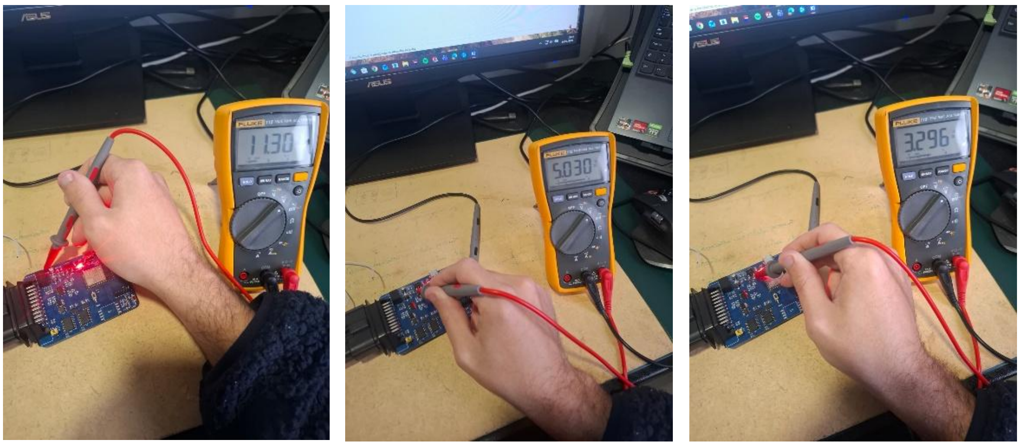

Figure 65 - DcDc conversion test

Subsequently, the code uploading system for the PCB and the possibility of powering it up to 5 V via the USB Type-C port were tested. After connecting the PCB to the computer, the power LED turned on and the computer immediately detected the connected device, indicating correct system operation. As shown in Figure 66.

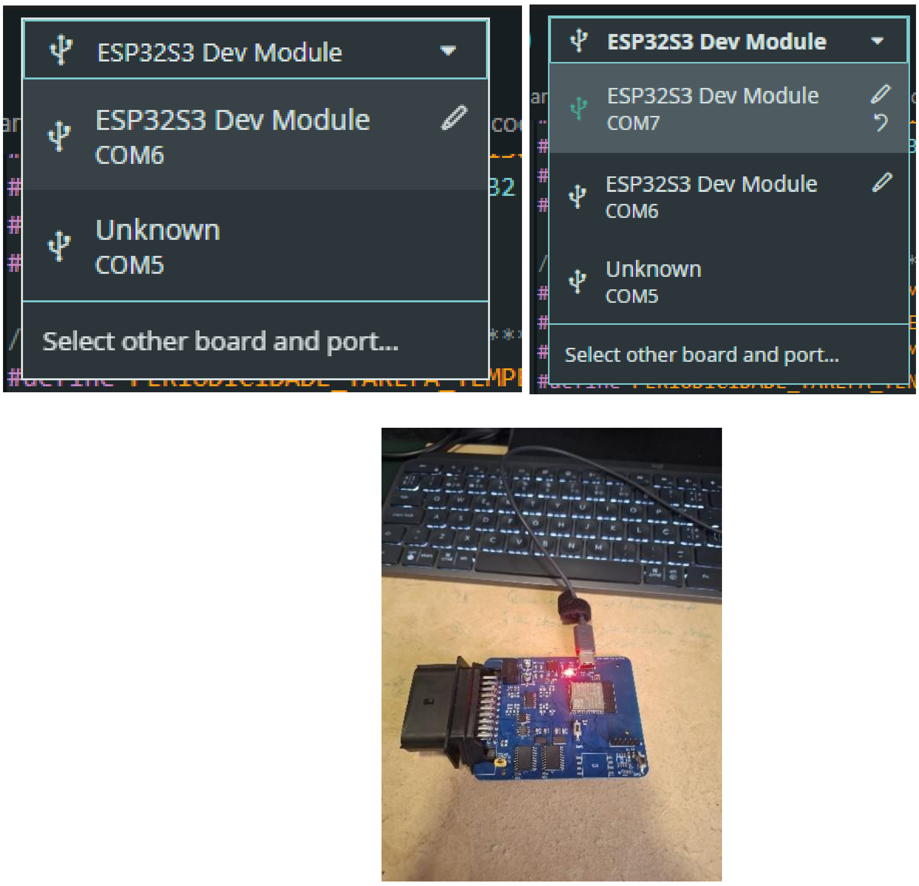

Figure 66 - Code upload Test

Subsequently, a base code was uploaded in order to verify the programmability of the microcontroller. For testing the PCB CAN communication system, this base code was used to generate and transmit CAN messages with known identifiers and data contents. This code was not developed as part of this work and was used exclusively as a tool for hardware and CAN communication validation. As shown in Figure 67.

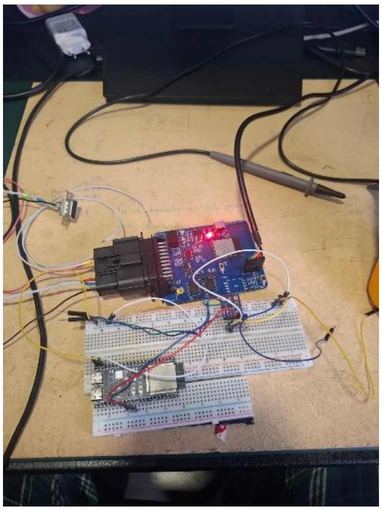

Figure 67 - Can Test

The test system consisted of the cyclic transmission of three distinct CAN messages, each with a specific identifier (ID) and associated with a set of simulated variables. The messages were sent by an ESP32-S3 equipped with a CAN transceiver, configured to operate at a speed of 500 kbps.

Three different CAN messages were transmitted, corresponding to different system parameters: oil pressure and temperature (ID 0x100), H_20 pressure and temperature (ID 0x105), and engine speed together with battery voltage (ID 0x110).

Each message was structured with three data bytes. The first byte corresponds to the pressure or voltage value, while the following two bytes represent the main variable encoded in two bytes (MSB and LSB), allowing higher resolution values to be transmitted.

The messages were transmitted sequentially and cyclically, with a fixed period between transmissions, enabling verification of the correct transmission and reception of the different CAN identifiers by the developed PCB.

The byte organization of each message is presented in the following table. As presented in Table 10.

Table 10 - CAN Message Structure and Byte Allocation for Test Signals

CAN ID HEX	BYTE 0	BYTE 1	BYTE 2
0X100	Oil pressure	Oil Temperature (MSB)	Oil Temperature (LSB)
0X105	H_2O pressure	H_2O Temperature (MSB)	H_2O Temperature (LSB)
0X110	Battery Voltage	RPM (MSB)	RPM (LSB)

On the receiver side, corresponding to the developed PCB under validation in this work, the CAN messages were received in hexadecimal format. Based on the predefined constant values used in the test, the expected contents were as follows: for ID 0x100, the value 0x2B in the byte corresponding to oil pressure and 0x0032 in the bytes corresponding to oil temperature; for ID 0x105, the value 0x34 for H_2O pressure and 0x005A for H_2O temperature; and for ID 0x110, the value 0x0D for battery voltage and 0x1D4C for engine speed. The correct reception of these values confirmed the proper operation of the PCB CAN receiver.

The transmitted message is presented in the following table. As presented in Table 11.

Table 11 - Decoded CAN Messages and Signal Values

ID CAN	BYTE 0	BYTE 1	BYTE 2	DESCRIÇÃO
64	0x2B	0x00	0x32	Oil Pressure = 43 ; Oil Temperature= 50
69	0x34	0x00	0x5A	H_2O pressure = 52 ; H_2O temperature = 90
6E	0x0D	0x1D	0x4C	Battery Voltage = 13.5 V ; RPM = 7500

As shown in Figure 68, through the microcontroller's serial interface, the received messages matched the transmitted messages, confirming the correct reception of the data.

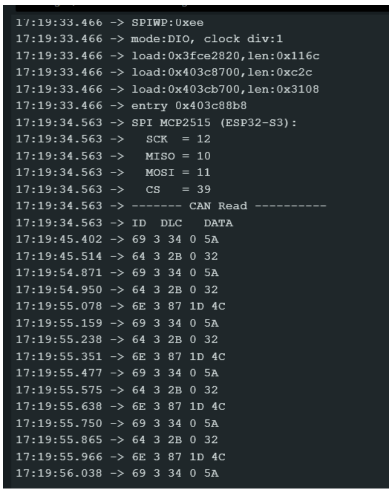

Figure 68 - Can test serial print

Subsequently, the differential pressure and temperature sensors were validated. Both sensors were evaluated in the experimental test described in Section 4.3, where their validation and calibration were performed.

Regarding the NOx sensor, it was confirmed that it is communicating correctly, and the required data could be successfully acquired. As shown in Figure 69.

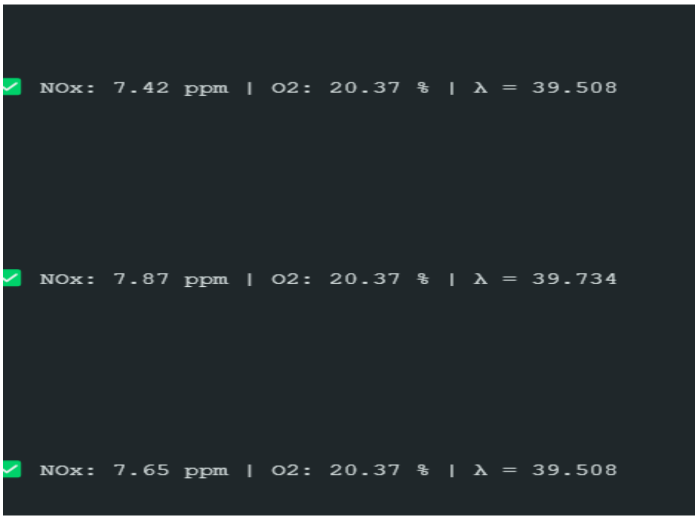

Figure 69 - Nox Validation via uart

After some tests the issue observed in the differential pressure measurement system was related to the instability of the zero-pressure (0 Pa) reference at startup. In practice, when no real pressure difference existed between the two measurement points, the analog output signal of the sensor did not consistently initialize at the same value. In some cases, the baseline voltage was approximately 0.8 V, while in others it was closer to 0.9 V. This variation introduced an immediate offset in the calculated pressure. Since the original implementation relied on a fixed calibration curve, any shift in this baseline was incorrectly interpreted as a real pressure differential, even when the actual differential pressure was zero.

This behavior was consistent with known characteristics of analog sensing systems and was likely caused by a combination of factors. The most relevant contributors included sensor offset drift, thermal stabilization effects during the first seconds after power-up, ADC reference variability, supply fluctuations, and minor pneumatic effects from the installation. In essence, the slope of the calibration remained valid, but the origin shifted between power cycles. In the original implementation, the pressure was calculated using a fixed linear relationship: As shown in Figure 70.

```
const float v_avg = ((float)adc_avg * 0.000804884f)+ 0.060f;
const int32_t dp_pa = 1833.18056829 * v_avg -1499.54170486;
```

Figure 70 - standard sensor equation

This formulation assumed a constant zero reference. As a result, any deviation in the actual sensor offset at startup directly propagated into the computed pressure value. Therefore, the primary limitation was not the gain accuracy, but the assumption of a fixed offset in a system where the offset was inherently variable.

To address this limitation, an automatic zero calibration procedure was implemented during the first 10 seconds after startup. During this interval, the system assumed that the real differential pressure was zero and collected a large number of ADC samples. The average of these samples was converted into a voltage value and stored as the new reference corresponding to zero differential pressure. After this calibration phase, the system no longer used a fixed offset in the calibration equation. Instead, it subtracted the measured startup offset before applying the calibrated gain. This approach preserved the original slope while compensating for the actual offset present at each startup.

To support this solution, new configuration parameters and global variables were introduced to define the calibration duration, ADC-to-voltage conversion, and storage of the calibrated zero: As shown in Figure 71.

```
// Auto-zero no arranque
#define DP_CAL_TIME_MS            60000UL
#define DP_CAL_PRINT_MS           500UL
#define DP_CAL_SAMPLE_DELAY_MS    2UL

// Calibração ADC -> V
#define DP_ADC_TO_V_GAIN          0.000804884f
#define DP_ADC_TO_V_OFFSET        0.060f

// Calibração V -> Pa
// Mantém-se o ganho da tua reta original
#define DP_SLOPE_PA_PER_V         1833.18056829f

// Limites físicos do sensor
#define DP_SENSOR_MAX_V           3.0f
#define DP_SENSOR_MAX_PA          3920.0f

static volatile float g_dp_zero_v = 0.818f;   // valor default até calibrar
static volatile bool  g_dp_cal_ok = false;

// ================== FLOW CONFIG ==================
#define FLOW_TASK_HZ              10
#define DP_DEADBAND_PA            1.0f
```

Figure 71 - Configuration parameters for differential pressure measurement, including calibration constants, sensor limits, and auto-zero settings.

The automatic zero calibration routine was implemented as a dedicated function executed during the setup() phase, prior to the initialization of the FreeRTOS tasks. This ensured that no measurement processing occurred before the zero reference had stabilized: As shown in Figures 72 and 73.

```
// ================= AUTO-ZERO DP =================
static void calibrate_dp_zero_startup(void) {
  const uint32_t t_start = millis();
  uint64_t sum_adc = 0;
  uint32_t samples = 0;
  uint32_t adc_min = 4095;
  uint32_t adc_max = 0;
  uint32_t last_print = 0;

  Serial.println();
  Serial.println("============================================");
  Serial.println("CALIBRACAO DP: auto-zero durante 60 segundos");
  Serial.println("Garantir 0 Pa diferencial durante a calibracao");
  Serial.println("============================================");

  while ((millis() - t_start) < DP_CAL_TIME_MS) {
    const uint32_t adc = (uint32_t)analogRead(PIN_DP_ADC);

    sum_adc += adc;
    samples++;

    if (adc < adc_min) adc_min = adc;
    if (adc > adc_max) adc_max = adc;

    const uint32_t now = millis();
    if ((now - last_print) >= DP_CAL_PRINT_MS) {
      const float progress = 100.0f * (float)(now - t_start) / (float)DP_CAL_TIME_MS;
      const float adc_avg_now = (samples > 0) ? ((float)sum_adc / (float)samples) : 0.0f;
      const float v_avg_now = adc_to_volts((uint32_t)lroundf(adc_avg_now));
```

Figure 72 - Auto-zero calibration routine for the differential pressure sensor at system startup

```
      const float v_avg_now = adc_to_volts((uint32_t)lroundf(adc_avg_now));

      Serial.print("Calibracao DP: ");
      Serial.print(progress, 1);
      Serial.print("% | ADCmedio=");
      Serial.print(adc_avg_now, 1);
      Serial.print(" | Vmedio=");
      Serial.println(v_avg_now, 3);

      last_print = now;
    }

    delay(DP_CAL_SAMPLE_DELAY_MS);
  }

  if (samples == 0) {
    Serial.println("ERRO: sem amostras na calibracao DP");
    g_dp_zero_v = 0.818f;
    g_dp_cal_ok = false;
    return;
  }

  const float adc_avg = (float)sum_adc / (float)samples;
  const float v_zero_raw = adc_to_volts((uint32_t)lroundf(adc_avg));
  const float v_zero = roundf(v_zero_raw * 1000.0f) / 1000.0f;

  g_dp_zero_v = v_zero;
  g_dp_cal_ok = true;

  Serial.println();
  Serial.println("=== RESULTADO CALIBRACAO DP ===");
  Serial.print("Amostras       : ");
  Serial.println(samples);
```

Figure 73 - Final stage of the differential pressure sensor auto-zero calibration, including offset computation and validation.

This function effectively replaced the assumption of a fixed zero by measuring the actual system offset at startup. It was then invoked in the setup() function before any tasks were created: As shown in Figure 74.

```
// Calibracao de zero do DP antes das tasks arrancarem
calibrate_dp_zero_startup();
```

Figure 74 - Invocation of the differential pressure sensor auto-zero calibration routine during system startup.

The key modification in the pressure computation was applied in the vTask_DP_Read task. Previously, the system directly applied a full linear calibration including a fixed offset. This was replaced by a two-step process: first correcting the measured voltage by subtracting the calibrated zero, and then applying the gain: As shown in Figure 75.

```
// ADC -> V
const float v_avg = adc_to_volts(adc_avg);

// correcao de offset medido no arranque
const float v_corr = roundf((v_avg - g_dp_zero_v) * 100.0f) / 100.0f;

// conversao para Pa mantendo o ganho
int32_t dp_pa = (int32_t)lroundf(DP_SLOPE_PA_PER_V * v_corr);
```

Figure 75 - Differential pressure computation from ADC signal, including offset correction and conversion to physical units (Pa)

This reformulation is mathematically equivalent to a linear calibration but with a dynamically adjusted offset. The original expression:

dp_pa = 1833.18056829 * v_avg -1499.54170486;

was effectively replaced by:

dp_pa = gain * (measured_voltage - calibrated_zero_voltage)

From a physical perspective, this approach is more appropriate because it isolates the offset error without altering the sensitivity of the sensor.

Additionally, a saturation mechanism was introduced to ensure that the computed pressure remained within the physical limits of the sensor, defined as ±3920 Pa for a 0–3 V range: As shown in Figure 76.

```
// saturacao fisica opcional
if (dp_pa > (int32_t)DP_SENSOR_MAX_PA)  dp_pa = (int32_t)DP_SENSOR_MAX_PA;
if (dp_pa < -(int32_t)DP_SENSOR_MAX_PA) dp_pa = -(int32_t)DP_SENSOR_MAX_PA;
```

Figure 76 - Saturation of the computed differential pressure to the physical limits of the sensor.

To improve observability and validation, the calibrated zero value and calibration status were also integrated into the system state and displayed via the serial interface. This allowed direct verification of the calibration result after each startup.

In summary, the issue stemmed from the use of a fixed zero reference in a system where the sensor offset varied between power cycles. The most probable causes were sensor offset drift and transient thermal effects. The implemented solution introduced a startup auto-zero calibration phase, which measured and stored the actual zero reference under no-flow conditions. This eliminated the observed offset error while preserving the original calibration gain.

It should be noted, however, that this approach remained valid only if the differential pressure was truly zero during the calibration period. If any real pressure differential existed during those 60 seconds, the system would calibrate an incorrect zero, resulting in a systematic measurement error. This limitation represented the next critical aspect to address in order to further improve system robustness. As shown in Figure 77.

```
Calibracao DP: 33.2% | ADCmedio=973.2 | Vmedio=0.843
Calibracao DP: 34.0% | ADCmedio=973.1 | Vmedio=0.843
Calibracao DP: 34.9% | ADCmedio=973.1 | Vmedio=0.843
Calibracao DP: 35.7% | ADCmedio=973.0 | Vmedio=0.843
Calibracao DP: 36.5% | ADCmedio=973.0 | Vmedio=0.843
Calibracao DP: 37.4% | ADCmedio=972.9 | Vmedio=0.843
Calibracao DP: 38.2% | ADCmedio=972.9 | Vmedio=0.843
Calibracao DP: 39.0% | ADCmedio=972.8 | Vmedio=0.843
Calibracao DP: 39.9% | ADCmedio=972.8 | Vmedio=0.843
Calibracao DP: 40.7% | ADCmedio=972.8 | Vmedio=0.843
Calibracao DP: 41.5% | ADCmedio=972.7 | Vmedio=0.843
Calibracao DP: 42.4% | ADCmedio=972.7 | Vmedio=0.843
Calibracao DP: 43.2% | ADCmedio=972.6 | Vmedio=0.843
Calibracao DP: 44.0% | ADCmedio=972.6 | Vmedio=0.843
Calibracao DP: 44.9% | ADCmedio=972.6 | Vmedio=0.843
Calibracao DP: 45.7% | ADCmedio=972.5 | Vmedio=0.843
Calibracao DP: 46.5% | ADCmedio=972.5 | Vmedio=0.842
Calibracao DP: 47.4% | ADCmedio=972.4 | Vmedio=0.842
Calibracao DP: 48.2% | ADCmedio=972.4 | Vmedio=0.842
Calibracao DP: 49.0% | ADCmedio=972.4 | Vmedio=0.842
Calibracao DP: 49.9% | ADCmedio=972.3 | Vmedio=0.842
Calibracao DP: 50.7% | ADCmedio=972.3 | Vmedio=0.842
Calibracao DP: 51.5% | ADCmedio=972.2 | Vmedio=0.842
Calibracao DP: 52.4% | ADCmedio=972.2 | Vmedio=0.842
Calibracao DP: 53.2% | ADCmedio=972.2 | Vmedio=0.842
Calibracao DP: 54.0% | ADCmedio=972.1 | Vmedio=0.842
Calibracao DP: 54.9% | ADCmedio=972.1 | Vmedio=0.842
Calibracao DP: 55.7% | ADCmedio=972.0 | Vmedio=0.842
Calibracao DP: 56.5% | ADCmedio=972.0 | Vmedio=0.842
Calibracao DP: 57.4% | ADCmedio=971.9 | Vmedio=0.842
Calibracao DP: 58.2% | ADCmedio=971.9 | Vmedio=0.842
```

Figure 77 - Sensor zero-offset calibration

4.3 venturi validation

The validation of the Venturi aimed to assess the accuracy of the proposed flow measurement method under controlled experimental conditions. For this purpose, a test bench was assembled in which predefined airflow rates were imposed and the values calculated by the developed system were compared with the corresponding reference values measured experimentally.

The airflow was generated using a dedicated air supply system, consisting of a fan capable of both adjusting and measuring the airflow rate. The flow direction was established from the inlet section, where the Venturi was installed, towards the outlet. The fan was positioned in an intermediate section of the setup, while a regulating valve located at the outlet allowed manual adjustment of the flow rate. In addition, a potentiometer was used to vary the fan speed and, consequently, the airflow. As shown in Figure 78.

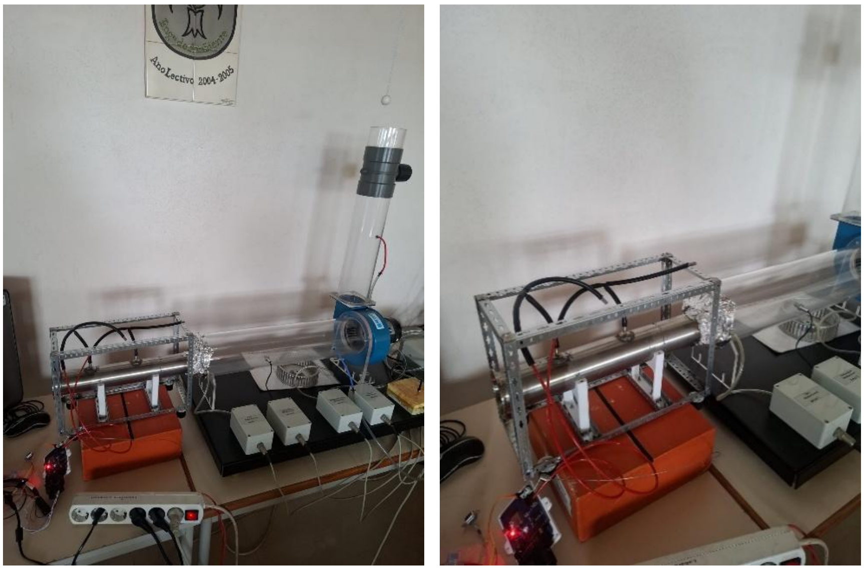

Figure 78 - flow test and calibration

During the experimental procedure, the operating points were not imposed a priori. Instead, the airflow was gradually varied by adjusting the fan speed and the outlet valve, and the corresponding flow values were read directly from the reference system software. At each stabilized condition, the flow value indicated by the software was recorded and defined as a measurement point. These points were subsequently organized and presented in Table 12.

Table 12 Flow Rate Points

CBM/H [m^3/h]
TEST FLOW RATE
384
343
295
260
210
173
119
96
60

For each operating point, data acquisition was performed simultaneously from multiple sources. The differential pressure was measured both by the reference instrument (PVW100) and by the differential pressure sensor integrated in the developed PCB. The mass flow rate calculated by the microcontroller-based system was also recorded. In addition, temperature measurements were collected from three independent sources: the temperature sensor integrated in the PCB, a digital thermometer, and the temperature reading provided by the fan system. As shown in Figure 81.

Figure 81 - Flow Test

The results obtained for each measurement point were then compared with the corresponding reference values, and the comparative analysis is presented in Tables 13 14 e 15.

In the temperature validation, a high level of agreement was observed among the three measurement systems used, with no significant deviations identified between the recorded values. The average temperature during the tests was approximately 20.5 ºC, which is consistent with the ambient temperature at the time of the experiments. As shown in Figure 79.

Table 13 - Temperature Results

PCB Temperature [ºC]	DIGITAL THERMOMETER TEMPERATURE [ºC]	VENTILATOR TEMPERATURE [ºC]
21	20.3	21
20.7	20.3	21
20.8	20.3	21
20.8	20.3	21
20.3	20.3	21
20.1	20.3	21
20.2	20.4	21
20.2	20.4	21
20.2	20.4	21

Figure 7979 - temperature measurement

It was observed that the flow rate values present significant deviations between the values calculated by the PCB and those indicated by the fan. However, according to the fan datasheet, at maximum rotation speed the device delivers a maximum flow rate of approximately 0.055 m³/s. This value is inconsistent with the flow rates indicated by the simulator measurement system, suggesting that the latter does not provide reliable measurements.

Therefore, it was not possible to properly validate the flow rate based on the values provided by the fan. Consequently, external validation using appropriate reference equipment is required in order to accurately calibrate and validate the flow rate calculation equation.

Furthermore, additional experimental testing is mandatory to improve the calibration of the flow rate estimation method. This includes controlled laboratory tests using reliable reference instruments, followed by validation under real engine operating conditions. Considering the law of mass conservation, the exhaust gas mass flow rate can be determined as the sum of the intake air mass flow rate and the injected fuel mass flow rate, thus enabling an indirect validation of the obtained values. As shown in Figure 80 and presented in Table 14.

Table 13 - Flow Results

FLOW PCB [m^3/s]	TEST FLOW RATE [m^3/s]	ERROR FLOW PCB/TEST
0.00000	0.0167	-100%
0.00286	0.0267	-89%
0.00408	0.0331	-88%
0.00637	0.0481	-87%
0.00816	0.0583	-86%
0.01061	0.0722	-85%
0.01282	0.0819	-84%
0.01404	0.0953	-82%
0.01624	0.1067	-81%

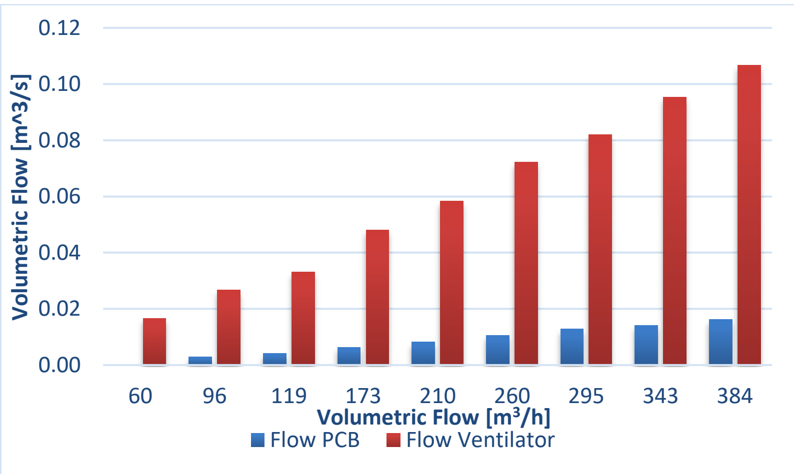

Figure 80 - Comparison between calculated flow rate and simulator flow rate

It was observed that, up to approximately 160 Pa of differential pressure, the system error is negligible. However, for values below this threshold, it was necessary to recalibrate the sensor by adjusting its transfer curve. As a result, the initial equation was replaced by a new calibrated equation for this operating range.

For differential pressure values above 160 Pa, the original sensor equation was maintained, as it exhibited appropriate behaviour and good agreement with the reference measurements.

Due to the limitations of the test setup, specifically the fan used, which only allows differential pressures up to approximately 560 Pa, it was possible to test only about one-seventh of the sensor's full measurement range. Therefore, the validity of the calibration equation is limited to the experimentally tested range.

Consequently, it is concluded that further validation by a specialized entity is required in order to perform a complete calibration of the sensor over its entire operating range, as well as to ensure a more accurate validation of the flow measurement. As shown in Figure 82 and presented in Table 15.

Table 15 - Differential pressure results

[Pa]	[Pa]	Error
DP PCB	DP PVW100	%
560	555	1%
458	445	3%
348	347	0%
275	286	-4%
165	180	-8%
92	110	-16%
37	52	-29%
18	36	-50%
0	17	-100%

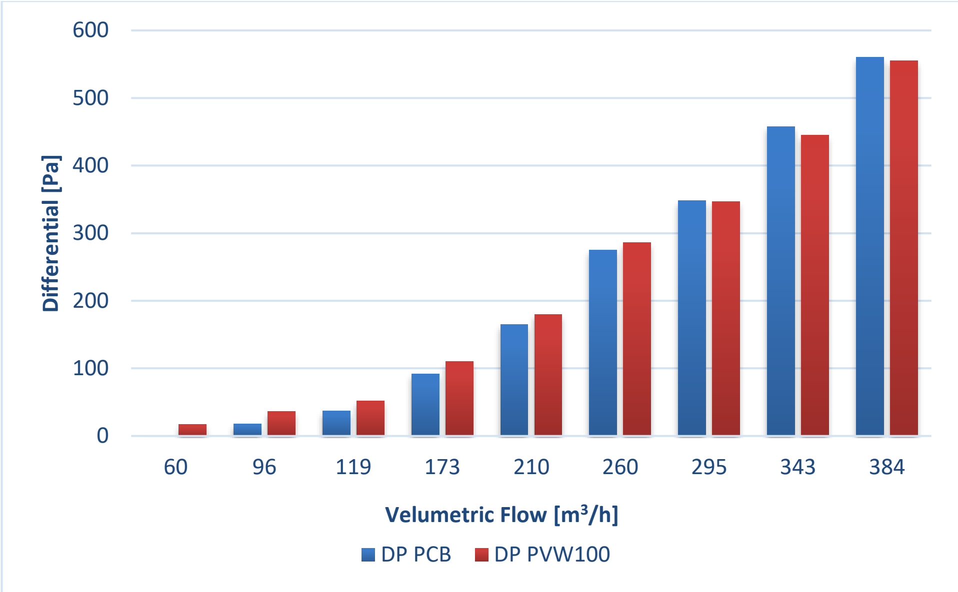

Figure 82 - Differential pressure comparison between PVW100 and PCB measurements as a function of volumetric flow rate

Despite the limitations identified in the experimental validation process, namely the absence of a reliable reference system for flow rate measurement, the obtained results allow for drawing positive conclusions regarding the performance of the developed Venturi. In particular, the consistency between theoretical results, CFD analysis, and the measured differential pressure values indicates that the operating principle has been correctly implemented. The discrepancies observed in the flow rate do not compromise the validity of the concept but highlight the need for proper calibration supported by certified reference equipment. Therefore, the developed Venturi can be considered a technically viable solution for exhaust gas flow measurement, showing strong potential for application after a more rigorous calibration and validation process.

4.4 Total Price

This subsection presents the cost analysis associated with the development of the proposed system. The total budget for the main components is summarized in Table X, including the cost of the PCB (€70,34), the Venturi tube (€675,85), and the NOx measurement module (€3550), resulting in an overall cost of approximately €4296,2. All values include Portuguese Value Added Tax (VAT); however, additional expenses such as shipping, customs duties, and development costs were not considered.

It should be noted that the reported cost corresponds primarily to hardware components and does not include engineering effort, calibration procedures, or system certification.

When compared to existing commercial solutions, namely Portable Emissions Measurement Systems (PEMS) from manufacturers such as AVL and HORIBA, a significant cost difference can be observed. These systems typically operate in the range of tens of thousands of euros, often exceeding €150,000 and reaching values above €200,000 depending on the configuration, measured pollutants, and certification level.

In this context, the developed system represents a low-cost alternative, enabling the measurement of relevant exhaust gas parameters with a substantially lower investment. However, it must be emphasized that this cost reduction comes with limitations in terms of accuracy, robustness, and certification, meaning that the system is not directly comparable to fully homologated commercial solutions. Nevertheless, it is suitable for applications such as research, development, and preliminary emissions monitoring. As presented in Table 16.

Table 16 - Price Tabel

		Unit Price (Euro)	*Quantities*	*final Price (Euro)*
PCB	PCB	1,5	1	1,5
	USB-C	1,49	1	1,49
	DCDC 3v3	2,04	1	2,04
	DCDC 5v	3,48	1	3,48
	Main PCB Connector	7,44	1	7,44
	Micro controller	6,04	1	6,04
	Thermocouple chip	14,04	1	14,04
	DP Sensor	16,94	1	16,94
	Transceiver CAN	1,1	2	2,2
	Ampop	1,75	1	1,75
	CAN Crystal	0,594	2	1,188
	MCP2515	2,67	2	5,34
	Male Connector	4,27	1	4,27
	Protection Diode	0,257	1	0,257
	Connector pins	0,118	20	2,36
			Total	70,34
Venturi	Venturi	574,59	1	574,59
	Air pressure taps	3,73	2	7,46
	Structure	40	1	40
	Inox Connectors	26,9	2	53,8
			Total	675,85
ECM Model	Model	3550	1	3550
			Total	**4296,2**

4.5 System Validation Subchapter conclusion

The validation results demonstrate that the developed system operates correctly at both component and system levels, with consistent performance across the evaluated subsystems.

The NOx module exhibited good agreement with the reference instrument, particularly in lambda measurement, where deviations remained low across all operating points. The NOx measurements showed acceptable trends, although larger deviations were observed under certain conditions, indicating sensitivity to operating parameters. Given these observations, additional validation using an independent NOx measurement system is recommended in order to confirm the obtained results and ensure measurement accuracy.

The PCB validation confirmed the correct operation of all hardware components, including power supply, communication interfaces, and sensor integration. The implementation of an automatic zero calibration for the differential pressure sensor effectively addressed offset variability at startup, improving measurement stability.

In the Venturi validation, the differential pressure measurements showed good agreement with the reference instrument for values above approximately 160 Pa. For lower pressure differentials, recalibration of the sensor transfer function was required. However, due to limitations of the test setup, only a fraction of the sensor's operating range was experimentally validated.

The flow rate results presented significant discrepancies when compared with the values provided by the fan system, which were found to be inconsistent with the manufacturer's specifications. As a result, it was not possible to validate the flow measurement under the current conditions, Additional testing is required.

Temperature measurements showed strong agreement across all measurement systems, confirming the reliability of the temperature acquisition.

Overall, the system demonstrated reliable operation, although further external validation is required to fully characterize and calibrate the flow measurement and extend the validation across the complete operating range.

This page was intentionally left blank

5 Conclusion

5.1 Work Conclusions and Achievement of Objectives

The work developed allowed the defined objectives to be achieved, making it possible to design and implement a portable system for measuring relevant exhaust gas parameters, namely temperature, NOx concentration, and flow rate estimation.

The system architecture proved to be suitable for the intended application, with particular emphasis on the use of CAN communication and the modular organization of both hardware and software. The developed PCB operated correctly, including power supply, signal acquisition, and communication between modules.

The NOx measurement system showed consistent results when compared with reference equipment: the average NOx values differed from the Testo analyser by 7.27%, 0.44%, 11.00%, 15.06% and 21.34% across the five operating points, and the O_2 concentration differed by only 2% from the Testo and 0.9% from the dynamometer bench. The lambda values agreed with the vehicle and AEM sensors within 0.35% to 2.59%. Temperature measurements showed strong agreement across all sensors.

Regarding flow measurement, the Venturi-based method proved valid from theoretical and numerical perspectives, with the CFD analysis predicting a measurable pressure differential of approximately 0.28 bar under high flow conditions (116 m/s inlet velocity). However, at low flow rates (1.46 m/s) the generated pressure differential dropped to about 6 Pa (0.00006 bar), which is insufficient to ensure reliable measurement with conventional sensors.

Furthermore, the experimental validation of the flow rate was not conclusive: the differential-pressure error remained negligible only above approximately 160 Pa, and below this threshold the sensor required recalibration, while the flow values calculated by the PCB showed large deviations relative to the reference fan (whose maximum output is about 0.055 m^3/s). This prevents confirmation of the accuracy of the implemented model and constitutes one of the main constraints of this work.

From an architectural perspective, the system demonstrates a high level of flexibility, allowing the integration of multiple ECM measurement modules in parallel via the CAN bus. Although the current system is configured only for NOx measurement, this approach enables future expansion to measure other relevant gases and Particulates without requiring significant structural modifications.

Overall, the developed system represents a functional, low-cost solution aligned with the PEMS concept, with a total component cost of approximately €4296 (PCB €70.34, Venturi €675.85 and NOx module €3550) compared with commercial PEMS that often exceed €150,000. It is suitable for research applications, although it is not yet comparable to commercial systems in terms of accuracy and validation, particularly for flow-rate measurement.

5.2 Future Work

The development carried out highlighted several limitations that should be addressed in future work, with the aim of improving the robustness, accuracy, and applicability of the system.

The main limitation identified is related to the measurement of exhaust gas flow rate. The experimental validation was not conclusive due to the use of a reference system with inconsistent performance. Therefore, it is essential to perform new tests using certified reference equipment, such as calibrated flow benches or commercial PEMS systems, in order to validate and refine the implemented calculation model.

Additionally, indirect validation of the flow rate based on the law of mass conservation should be explored, considering that the exhaust gas mass flow corresponds to the sum of the intake air mass and the injected fuel mass. This approach will allow an independent verification of the obtained results.

Another relevant limitation concerns the performance of the Venturi under low flow conditions. To overcome this issue, different approaches may be considered, including the use of multiple Venturi geometries adapted to different operating ranges, the use of higher-sensitivity differential pressure sensors, or the adoption of alternative flow measurement methods.

In the field of emissions measurement, expanding the system to include additional ECM modules represents a natural evolution. The integration of additional sensors will enable a more comprehensive characterization of exhaust gases, including the measurement of species such as NH_3, CO_2, O_2, or PM, allowing more advanced analysis of aftertreatment system performance.

From a firmware perspective, improvements can be implemented at the signal processing level, including more advanced filtering techniques and data validation mechanisms, in order to reduce noise impact and increase measurement reliability. Temporal synchronization between variables should also be improved to enable more accurate analysis under transient conditions.

Finally, a relevant evolution of the system involves the direct determination of emissions in mass terms (e.g., g/s of NOx), by combining pollutant concentration with exhaust gas flow rate. This approach will bring the developed system closer to solutions used in regulatory contexts, significantly increasing its technical value and practical applicability.

After full validation of the system, a set of experimental tests should be carried out with the objective of characterizing NOx emissions across different vehicles, enabling the definition of maximum reference values per Euro standard and the development of a suitable testing procedure for application in periodic technical inspections, in order to address the current lack of standardized methodologies for NOx evaluation in this context.

6 Bibliografia

[1] A. Melas, T. Selleri, R. Suarez-Bertoa, and B. Giechaskiel, “Evaluation of Solid Particle Number Sensors for Periodic Technical Inspection of Passenger Cars,” *Sensors 2021, Vol. 21, Page 8325*, vol. 21, no. 24, p. 8325, Dec. 2021, doi: 10.3390/s21248325.

[2] J. Martins, *Motores de Combustão Interna*. Porto - Portugal, 2020.

[3] J. B. Heywood, *Internal Combustion Engine Fundamentals*. Singapore: McGraw-Hill, 2018.

[4] P. & C. M. Coelho, *Combustão*. Amadora - Portugal: Edições Orion, 2012.

[5] R. D. Atkins, *An introdution to engine testing and development*. Warrendale - USA, 2009.

[6] H. I. Abdel-Shafy and M. S. M. Mansour, “A review on polycyclic aromatic hydrocarbons: Source, environmental impact, effect on human health and remediation,” *Egyptian Journal of Petroleum*, vol. 25, no. 1, pp. 107–123, Mar. 2016, doi: 10.1016/J.EJPE.2015.03.011.

[7] Z. D. Ristovski *et al.*, “Respiratory health effects of diesel particulate matter,” *Respirology*, vol. 17, no. 2, pp. 201–212, May 2012, doi: 10.1111/j.1440-1843.2011.02109.x.

[8] M. Pietikäinen *et al.*, “Particle and NOx emissions of a non-road diesel engine with an SCR unit: The effect of fuel,” *Renew. Energy*, vol. 77, pp. 377–385, May 2015, doi: 10.1016/j.renene.2014.12.031.

[9] Isabella Nova, *Urea-SCR Technology for deNOx After Treatment of Diesel Exhausts*. 2014.

[10] Y. Wen, S. Zhang, Y. Wu, and J. Hao, “Vehicular ammonia emissions: an underappreciated emission source in densely populated areas,” *Atmos. Chem. Phys*, vol. 23, pp. 3819–3828, 2023, doi: 10.5194/acp-23-3819-2023.

[11] P. Nevalainen *et al.*, “Formation of NH3 and N2O in a modern natural gas three-way catalyst designed for heavy-duty vehicles: the effects of simulated exhaust gas composition and ageing,” *Appl. Catal. A Gen.*, vol. 552, pp. 30–37, Feb. 2018, doi: 10.1016/j.apcata.2017.12.017.

[12] M. Börnhorst and O. Deutschmann, “Advances and challenges of ammonia delivery by urea-water sprays in SCR systems,” *Prog. Energy Combust. Sci.*, vol. 87, Nov. 2021, doi: 10.1016/j.pecs.2021.100949.

[13] D. L. Baulch *et al.*, “Evaluated Kinetic Data for Combustion Modeling: Supplement II,” *J. Phys. Chem. Ref. Data*, vol. 34, no. 3, 2005, doi: 10.1063/1.1748524.

[14] V. Valverde *et al.*, “Measurement of Gaseous Exhaust Emissions of Light-Duty Vehicles in Preparation for Euro 7: A Comparison of Portable and Laboratory Instrumentation,” *Energies 2023, Vol. 16, Page 2561*, vol. 16, no. 6, p. 2561, Mar. 2023, doi: 10.3390/en16062561.

[15] A. A. Konnov, “On the role of C2O radicals in the prompt-NO mechanism,” *Combustion, Explosion, and Shock Waves 2008 44:5*, vol. 44, no. 5, pp. 497–501, Oct. 2008, doi: 10.1007/s10573-008-0077-y.

[16] Robert. Huzij, Angelo. Spano, and Sean. Bennett, “Modern diesel technology heavy equipment systems,” 2024.

[17] "Diesel Engine System Design | ScienceDirect." Accessed: Apr. 14, 2026. [Online]. Available: https://www.sciencedirect.com/book/monograph/9781845697150/diesel-engine-system-design

[18] *Directive 2014/45/EU of the European Parliament and of the Council of the European Communities*. Official Journal of the European Union, 2014, pp. 51–128.

[19] G. Kadijk, M. Elstgeest, N. E. Ligterink, and P. J. Van Der Mark, "Investigation into a Periodic Technical Inspection (PTI) test method to check for presence and proper functioning of Diesel Particulate Filters in light-duty diesel vehicles-part 2," 2017, Accessed: Mar. 19, 2026. [Online]. Available: www.tno.nl

[20] W. Jarosiński and P. Wiśniowski, "Verifying the Efficiency of a Diesel Particulate Filter Using Particle Counters with Two Different Measurements in Periodic Technical Inspection of Vehicles," *Energies 2021, Vol. 14, Page 5128*, vol. 14, no. 16, p. 5128, Aug. 2021, doi: 10.3390/en14165128.

[21] "PTI by Particle Count PN at Low Idle VERT recommended procedures and instruments 1. Why Periodic Technical Inspection (PTI) for On-road and Non-road Fleets Represents the Fastest Route to Clean Urban Air at Low Cost".

[22] B. GIECHASKIEL *et al.*, "Particle number measurements in the European legislation and future JRC activities," *Combustion Engines*, vol. 174, no. 3, pp. 3–16, Jul. 2018, doi: 10.19206/ce-2018-301.

[23] A. Melas, T. Selleri, R. Suarez-Bertoa, and B. Giechaskiel, "Evaluation of Measurement Procedures for Solid Particle Number (SPN) Measurements during the Periodic Technical Inspection (PTI) of Vehicles," *International Journal of Environmental Research and Public Health 2022, Vol. 19, Page 7602*, vol. 19, no. 13, p. 7602, Jun. 2022, doi: 10.3390/ijerph19137602.

[24] J. Franzetti *et al.*, "Assessment of a NOx Measurement Procedure for Periodic Technical Inspection (PTI) of Light-Duty Diesel Vehicles," *Energies (Basel).*, vol. 16, no. 14, p. 5520, Jul. 2023, doi: 10.3390/en16145520.

[25] "Vehicle safety – revising the EU's roadworthiness package." Accessed: Mar. 19, 2026. [Online]. Available: https://ec.europa.eu/info/law/better-

regulation/have-your-say/initiatives/13132-Vehicle-safety-revising-the-EUs-roadworthiness-package/feedback_en?p_id=19720

[26] B. Giechaskiel, P. Dilara, and J. Andersson, “Particle Measurement Programme (PMP) Light-Duty Inter-Laboratory Exercise: Repeatability and Reproducibility of the Particle Number Method,” *Aerosol Science and Technology*, vol. 42, no. 7, pp. 528–543, Jul. 2008, doi: 10.1080/02786820802220241.

[27] “on particle number measurement for the periodic technical inspection of vehicles equipped with compression ignition engines”, doi: 10.3390/s20205790.

[28] S. Zhang *et al.*, “On-board monitoring (OBM) for heavy-duty vehicle emissions in China: Regulations, early-stage evaluation and policy recommendations,” *Science of the Total Environment*, vol. 731, Aug. 2020, doi: 10.1016/j.scitotenv.2020.139045.

[29] P. Tapak, M. Kocur, M. Rabek, and J. Matej, “Periodical Vehicle Inspections with Smart Technology,” *Applied Sciences 2023, Vol. 13, Page 7241*, vol. 13, no. 12, p. 7241, Jun. 2023, doi: 10.3390/APP13127241.

[30] “Sources and emissions of air pollutants in Europe | Air quality in Europe 2022 | European Environment Agency (EEA).” Accessed: Mar. 20, 2026. [Online]. Available: https://www.eea.europa.eu/en/analysis/publications/air-quality-in-europe-2022/sources-and-emissions-of-air-pollutants-in-europe

[31] T. Selleri, A. D. Melas, A. Joshi, D. Manara, A. Perujo, and R. Suarez-Bertoa, “An Overview of Lean Exhaust deNOx Aftertreatment Technologies and NOx Emission Regulations in the European Union,” *Catalysts 2021, Vol. 11, Page 404*, vol. 11, no. 3, p. 404, Mar. 2021, doi: 10.3390/catal11030404.

[32] “Revision of the Directives of the Roadworthiness Package | EESC.” Accessed: Mar. 20, 2026. [Online]. Available: https://www.eesc.europa.eu/en/news-media/press-summaries/revision-directives-roadworthiness-package

[33] F. Boveroux *et al.*, “Feasibility study of a new test procedure to identify high emitters of particulate matter during periodic technical inspection,” *SAE*

Technical Papers, vol. 2019-April, no. April, Apr. 2019, doi: 10.4271/2019-01-1190.

[34] H. Burtscher, T. Lutz, and A. Mayer, "A New Periodic Technical Inspection for Particle Emissions of Vehicles," *Emission Control Science and Technology 2019 5:3*, vol. 5, no. 3, pp. 279–287, Jul. 2019, doi: 10.1007/s40825-019-00128-z.

[35] S. Lipp, "New procedure of NOx emission test (AU) in a future Periodic Technical Inspection (PTI)," 2021. Accessed: Mar. 20, 2026. [Online]. Available: https://tugraz.elsevierpure.com/en/publications/new-procedure-of-nox-emission-test-au-in-a-future-periodic-techni/

[36] J. Czerwinski, P. Comte, D. Engelmann, A. Mayer, T. Lutz, and V. Hensel, "Considerations of periodical technical inspection of vehicles with deNOx systems," *SAE Technical Papers*, vol. 2019-April, no. April, Apr. 2019, doi: 10.4271/2019-01-0744.

[37] "SEMS equipment in connection with periodic technical inspections (PTI) of lorries." Accessed: Mar. 20, 2026. [Online]. Available: https://www.danishroadtrafficauthority.dk/publications/sems-equipment-in-connection-with-periodic-technical-inspections-pti-of-lorries

[38] "Mobility and Transport 2023 - European Commission." Accessed: Mar. 20, 2026. [Online]. Available: https://commission.europa.eu/law/application-eu-law/implementing-eu-law/infringement-procedure/2023-annual-report-monitoring-application-eu-law/mobility-and-transport-2023_en

[39] E. V.D. Eijnden, R. Cloudt, F. Willems, and P. V.D. Heijden, "Automated model fit tool for SCR control and OBD development," *SAE Technical Papers*, 2009, doi: 10.4271/2009-01-1285.

[40] R. Vermeulen, R. Van Gijlswijk, P. Paschinger, and J. De Ruiter, "Dutch In-service Emissions Measurement and Monitoring Programme for Heavy-Duty Vehicles 2021," 2022, Accessed: Apr. 04, 2026. [Online]. Available: https://www.nsl-monitoring.nl/

[41] N. Fonseca González, J. Casanova Kindelán, and J. M. López Martínez, "Methodology for instantaneous average exhaust gas mass flow rate

measurement," *Flow Measurement and Instrumentation*, vol. 49, pp. 52–62, Jun. 2016, doi: 10.1016/J.FLOWMEASINST.2016.04.007.

[42] "Measurement of fluid flow by means of pressure differential devices inserted in circular cross-section conduits running full-Part 1: General principles and requirements," 2022.

[43] "Measurement of fluid flow by means of pressure differential devices inserted in circular cross-section conduits running full-Part 4: Venturi tubes," 2022.

[44] P. Pajdowski and B. Puchałka, "The Process of Diesel Particulate Filter Regeneration under Real Driving Conditions," *IOP Conf. Ser. Earth Environ. Sci.*, vol. 214, no. 1, Jan. 2019, doi: 10.1088/1755-1315/214/1/012114.

Attachment

Attachment A.

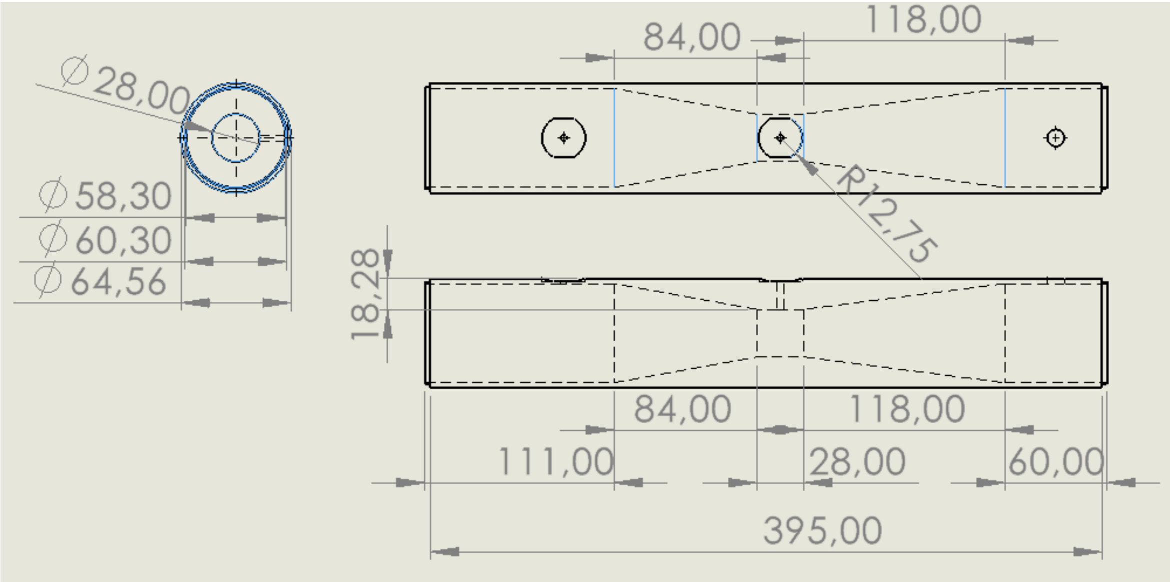

This page was intentionally left blank